Overview of the MOSAiC Expedition – Atmosphere

Matthew D. Shupe[*,1,2], Markus Rex[3], Byron Blomquist[1,2], P. Ola G. Persson[1,2], Julia Schmale[4], Taneil Uttal[2], Dietrich Althausen[5], Hélène Angot[6,4], Stephen Archer[7], Ludovic Bariteau[1,2], Ivo Beck[4], John Bilberry[8], Silvia Bucci[9], Clifton Buck[10], Matt Boyer[11], Zoé Brasseur[11], Ian M. Brooks[12], Radiance Calmer[1,13], John Cassano[1,13,14], Vagner Castro[15], David Chu[8], David Costa[1,2], Christopher J. Cox[2], Jessie Creamean[16], Susanne Crewell[17], Sandro Dahlke[3], Ellen Damm[18], Gijs de Boer[1,2,19], Holger Deckelmann[3], Klaus Dethloff[3], Marina Dütsch[9], Kerstin Ebell[17], André Ehrlich[20], Jody Ellis[21], Ronny Engelmann[5], Allison A. Fong[18], Markus M. Frey[22], Michael R. Gallagher[1,2], Laurens Ganzeveld[23], Rolf Gradinger[24], Jürgen Graeser[3], Vernon Greenamyer[21], Hannes Griesche[5], Steele Griffiths[25], Jonathan Hamilton[1,2], Günther Heinemann[26], Detlev Helmig[27], Andreas Herber[18], Céline Heuzé[28], Julian Hofer[5], Todd Houchens[29], Dean Howard[1,2,6], Jun Inoue[30, 31], Hans-Werner Jacobi[32], Ralf Jaiser[3], Tuija Jokinen[11], Olivier Jourdan[33], Gina Jozef[1,14,13], Wessley King[21], Amelie Kirchgaessner[22], Marcus Klingebiel[20], Misha Krassovski[34], Thomas Krumpen[18], Astrid Lampert[35], William Landing[36], Tiia Laurila[11], Dale Lawrence[37, 38], Michael Lonardi[20], Brice Loose[39], Christof Lüpkes[18], Maximilian Maahn[20], Andreas Macke[5], Wieslaw Maslowski[40], Christopher Marsay[10], Marion Maturilli[3], Mario Mech[17], Sara Morris[2], Manuel Moser[41,42], Marcel Nicolaus[18], Paul Ortega[8], Jackson Osborn[2], Falk Pätzold[35], Donald K. Perovich[43], Tuukka Petäjä[11], Christian Pilz[5], Roberta Pirazzini[44], Kevin Posman[7], Heath Powers[8], Kerri A. Pratt[45], Andreas Preußer[26], Lauriane Quéléver[11], Martin Radenz[5], Benjamin Rabe[18], Annette Rinke[3], Torsten Sachs[46,35], Alexander Schulz[3], Holger Siebert[5], Tercio Silva[47], Amy Solomon[1,2], Anja Sommerfeld[3], Gunnar Spreen[48], Mark Stephens[49], Andreas Stohl[9], Gunilla Svensson[50], Janek Uin[51], Juarez Viegas[8], Christiane Voigt[41,42], Peter von der Gathen[3], Birgit Wehner[5], Jeffrey M. Welker[52,53], Manfred Wendisch[20], Martin Werner[18], ZhouQing Xie[54], Fange Yue[54]

*Corresponding Author: matthew.shupe@noaa.gov
[1]Cooperative Institute for Research in Environmental Sciences, University of Colorado, Boulder, Colorado, United States
[2]National Oceanic and Atmospheric Administration, Physical Sciences Laboratory, Boulder, Colorado, United States
[3]Alfred-Wegener-Institut Helmholtz-Zentrum für Polar- und Meeresforschung, Potsdam, Germany
[4]École Polytechnique Fédérale de Lausanne, Lausanne, Switzerland
[5]Leibniz Institute for Tropospheric Research, Leipzig, Germany
[6]Institute for Arctic and Alpine Research, University of Colorado, Boulder, Colorado, United States
[7]Bigelow Laboratory for Ocean Sciences, East Boothbay, Maine, United States
[8]Los Alamos National Laboratory, Los Alamos, New Mexico, United States
[9]Department of Meteorology and Geophysics, University of Vienna, Vienna, Austria
[10]Skidaway Institute of Oceanography, University of Georgia, Savannah, Georgia, United States
[11]Institute for Atmospheric and Earth System Research, Faculty of Science, University of Helsinki, Helsinki, Finland
[12]University of Leeds, Leeds, United Kingdom
[13]National Snow and Ice Data Center, University of Colorado, Boulder, Colorado, United States
[14]Department of Atmospheric and Oceanic Sciences, University of Colorado, Boulder, Colorado, United States
[15]Pacific Northwest National Laboratory, Richland, Washington, United States
[16]Colorado State University, Ft. Collins, Colorado, United States

[17]University of Cologne, Institute for Geophysics and Meteorology, Cologne, Germany
[18]Alfred-Wegener-Institut Helmholtz-Zentrum für Polar- und Meeresforschung, Bremerhaven, Germany
[19]Integrated Remote and In Situ Sensing, University of Colorado, Boulder, Colorado, United States
[20]University of Leipzig, Leipzig Institute for Meteorology, Leipzig, Germany
[21]Hamelmann Communications, Pagosa Springs, Colorado, United States
[22]British Antarctic Survey, Natural Environment Research Council, Cambridge, United Kingdom
[23]Wageningen University, Wageningen, Netherlands
[24]UiT, The Arctic University of Norway, Langnes, Norway
[25]Australian Bureau of Meteorology, Melbourne, Australia
[26]University of Trier, Department of Environmental Meteorology, Trier, Germany
[27]Boulder A.I.R, LLC, Boulder, Colorado, United States
[28]Departement of Earth Sciences, University of Gothenburg, Gothenburg, Sweden
[29]Sandia National Laboratories, Albuquerque, New Mexico, United States
[30]National Institute of Polar Research, Tachikawa, Japan
[31]Japan Agency for Marine-Earth Science and Technology, Yokohama, Japan
[32]Institute for Geosciences and Environmental Research, CNRS/Université Grenoble Alpes/IRD/G-INP, Grenoble, France
[33]Université Clermont Auvergne, Laboratoire de Météorologie Physique, LaMP/CNRS/UCA, Clermont-Ferrand, France
[34]Oak Ridge National Laboratory, Oak Ridge, Tennessee, United States
[35]Institute of Flight Guidance, TU Braunschweig, Braunschweig, Germany
[36]Florida State University, Tallahassee, Florida, United States
[37]Research and Engineering Center for Unmanned Vehicles, University of Colorado, Boulder, Colorado, United States
[38]Aerospace Engineering Sciences, University of Colorado, Boulder, Colorado, United States
[39]University of Rhode Island, Kingston, Rhode Island, United States
[40]Naval Postgraduate School, Monterey, California, United States
[41]Institute for Physics of the Atmosphere, Deutsches Zentrum für Luft- und Raumfahrt (DLR), Oberpfaffenhofen, Germany
[42]Institute for Physics of the Atmosphere, University of Mainz, Mainz, Germany
[43]Thayer School of Engineering, Dartmouth College, Hanover, New Hampshire, United States
[44]Finnish Meteorological Institute, Helsinki, Finland
[45]University of Michigan, Ann Arbor, Michigan, United States
[46]GFZ German Research Centre for Geosciences, Potsdam, Germany
[47]Universidade dos Açores, Ponta Delgado, Portugal
[48]University of Bremen, Institute of Environmental Physics, Bremen, Germany
[49]Florida International University, Miami, Florida, United States
[50]Stockholm University, Stockholm, Sweden
[51]Brookhaven National Laboratory, Upton, New York, United States
[52]University of Alaska - Anchorage, Anchorage, Alaska, United States
[53]University of Oulu, Oulu, Finland
[54]University of Science and Technology of China, Department of Environmental Science and Engineering, Hefei, China

Journal: Elementa – MOSAiC Special Feature

ABSTRACT

As the Arctic rapidly changes it is essential to observe, understand, and model these changes. To support these needs, an annual cycle of observations of atmospheric properties, processes, and interactions was made while drifting with the sea ice across the central Arctic during the Multidisciplinary drifting Observatory for the Study of Arctic Climate (MOSAiC) expedition from October 2019 to September 2020. An international team designed and implemented the comprehensive program to document and characterize all aspects of the Arctic atmospheric system in unprecedented detail, using a variety of approaches, and across multiple scales. These measurements were coordinated with other observational teams to explore cross-cutting and coupled interactions with the Arctic ocean, sea ice, and ecosystem through a variety of physical and biogeochemical processes. This overview outlines the breadth and complexity of the atmospheric research program, which was organized into four sub-groups: atmospheric state, clouds and precipitation, gases and aerosols, and energy budgets. Atmospheric variability over the annual cycle revealed important influences from a persistent large-scale winter circulation pattern, leading to some storms with pressure and winds that were outside the interquartile range of past conditions suggested by long-term reanalysis. Similarly, the MOSAiC location was warmer and wetter in summer than the reanalysis climatology, in part due to its close proximity to the sea ice edge. The comprehensiveness of the observational program for characterizing and analyzing atmospheric phenomena is demonstrated via a winter case study examining air mass transitions and a summer case study examining vertical atmospheric evolution. Overall, the MOSAiC atmospheric program successfully met its objectives and was the most comprehensive atmospheric measurement program to date conducted over the Arctic sea ice. The obtained data will support a broad range of coupled-system scientific research and provide an important foundation for advancing multi-scale modeling capabilities in the Arctic.

1. Introduction and background

The Arctic climate system is changing rapidly as a result of rising global greenhouse gas concentrations. Arctic air temperature is increasing at a rate that is twice as fast as the global average (Overland et al., 2019), and this Arctic Amplification is caused in large part by numerous feedbacks related to the declining sea ice and other phenomena (Serreze and Barry, 2011). The loss of Arctic sea ice over the past two decades is one of the clearest manifestations of Arctic and global change. While declines in the spatial extent and thickness of sea ice are readily identified via observations (e.g., Kwok, 2018), the processes that both drive and respond to these sea ice changes are less obvious, and many are associated with the atmosphere. As temperatures rise, the atmosphere-surface energy balance shifts, but significant uncertainties remain about how, for example, increasing atmospheric moisture content will affect seasonal cloud properties and feedback on the surface (Middlemas et al., 2020) and the transport of moisture within, into, and out of the Arctic (Mellet Ardakani et al., 2021). Similarly, projected increases in evaporation and precipitation could play amplifying or buffering roles, depending on when and where they occur (Bintanja et al., 2020). Increased areas of open ocean, changes in terrestrial land surfaces, and modified air mass transport pathways are also affecting Arctic atmospheric composition and aerosol populations, which themselves can modulate cloud, precipitation, and radiation processes (Schmale et al., 2021). Moreover, all of these regional processes are subject to, and possibly play a role in, potential shifts in large-scale atmospheric circulation (Jaiser et al., 2013; Screen et al., 2018). Such shifts will affect meridional heat

transport, leading to increasing occurrence of warm air intrusions into the Arctic (Woods and Caballero, 2016), and likely supporting an intensification of cyclone impacts on the Arctic (Akperov et al., 2015) that further exacerbate Arctic change. These shifts might also affect the Arctic ozone layer (Romanowsky et al., 2019) and influence lower-latitude climate variability (Coumou et al., 2018; Cohen et al., 2020). To address these important, emergent issues in the Arctic and global climate systems, and particularly the role the atmosphere plays, requires a detailed understanding of the processes that underpin these changes, which will expedite development of improved models that can represent these processes robustly within the context of the coupled Arctic-global system.

Our understanding of Arctic atmospheric processes is based on spatially and temporally sparse observations over the last decades using a variety of approaches. These approaches started with the rudimentary meteorological measurements of early Arctic explorers (e.g., Nansen, 1897), who laid the foundation upon which change can be quantified. Atmospheric observations over the sea ice benefited greatly from the Russian drifting station program (Frolov et al., 2005), which periodically over the course of many decades (1937–2015) provided for extensive study of the lower-atmospheric structure, exchanges with the surface, and impacts on sea ice. Building on several prior activities, the year-long Surface Heat Budget of the Arctic Ocean (SHEBA, Perovich et al. 1999) project in the late 1990s focused on feedbacks that impact the Arctic energy budget and observed the first detailed annual cycle of cloud properties over the Arctic ice. In the years since, a number of other extended and seasonal campaigns probed the Arctic atmosphere over the sea ice (Gascard et al., 2008; Tjernström et al., 2014; Cohen et al., 2017; Wendisch et al., 2019; Vüllers et al., 2020; and others), bringing new sophisticated sensors and approaches to further characterize atmosphere-ice-ocean coupling, seasonal aerosol processes, vertical atmospheric stratification, atmospheric composition, cloud characteristics, and related topics. Only the most recent of these projects have started to incorporate the cross-disciplinary coupling of atmospheric physics to chemical and biological processes.

Land-based stations surrounding the Arctic Basin have also brought long-term perspectives with comprehensive instrument suites (Uttal et al., 2016). The international stations at Ny-Ålesund, Svalbard (e.g., Maturilli and Kayser, 2017) have been observing the Arctic atmosphere for decades, with more recent, intensified observations offering key insight into the North Atlantic storm track region, including long-term measurements of Arctic aerosols and clouds. The Department of Energy (DOE) Atmospheric Radiation Measurement (ARM) facility in northern Alaska (Verlinde et al., 2016) has been in operation since 1998, accumulating the longest continuous observational record of Arctic clouds, among other parameters. Nearby, the National Oceanic and Atmospheric Administration (NOAA) has been monitoring greenhouse gas concentrations since the 1970s (Dlugokencky et al., 1995). Together these stations, and others in northern Canada, Greenland, Scandinavia, and Russia provide a long-term, continuous perspective that is not available over the Arctic sea ice.

Finally, periodic aircraft campaigns have probed the Arctic atmosphere, often linking the land and ocean environments, seeking to better understand cloud structure (e.g., Herman and Curry, 1984; Curry et al., 2000; Verlinde et al., 2007; Wendisch et al., 2019), aerosol distributions (e.g., Brock et al., 2011; Herber et al., 2012; Ancellet et al., 2014), atmosphere-surface interactions (Walter and Overland, 1991; Drüe and Heinemann, 2001; Tetzlaff et al., 2015), atmospheric

composition and chemistry (e.g., Jacob et al., 2010; Roiger et al., 2015), storm structure (Brümmer et al., 2006) and many other processes. From space, polar-orbiting satellites also offer a unique spatial view of the Arctic atmosphere that has been used, among others, to constrain atmospheric moisture content (Groves and Francis, 2002; Boisvert et al., 2013), explore cloud feedbacks (Philipp et al., 2020) and changes (Morrison et al., 2018), and characterize precipitation (e.g., Edel et al., 2020).

Despite the vast knowledge gained from past Arctic observations, numerous uncertainties remain in modeling the Arctic atmosphere and its interactions within the coupled climate system. Uncertainties in large-scale circulation are often driven by a lack of Arctic observational data for assimilation into forecast systems (e.g., Jung et al., 2016). However, climate models also struggle to represent large-scale features like moisture fluxes into the Arctic (Woods et al., 2017) with certain consequences. Small-scale physical atmospheric processes are often poorly represented in models at all spatial and temporal scales. For example, warm biases in models at low levels have been associated with errors in Arctic surface sensible heat fluxes (Tjernström et al., 2021). Additionally, the long-standing model challenge of representing Arctic clouds can lead to biases in modeled radiative balance and feedbacks (Karlsson and Svensson 2013; Urrego-Blanco et al., 2019; Kretzschmar et al., 2020). More specifically, difficulties in representing cloud liquid water were shown to cause errors in the balance between surface radiative and turbulent heat fluxes in regional climate model simulations (Sedlar et al., 2020). Aerosol-cloud interactions are another common challenge for even high-resolution models (Stevens et al., 2018), due, in large part, to poor understanding of basic aerosol processes (Schmale et al., 2021). For a variety of reasons, including that many of the relevant processes operate at sub-grid scales, weather forecast and climate models also frequently struggle to represent common stable Arctic atmospheric boundary layers (Sandu et al., 2013) as well as the interactions between sea ice leads and the boundary layer structure (Heinemann et al. 2021). Lastly, the interactions of solar radiation with the sea ice surface and clouds are likely oversimplified, leading to major issues in simulating this key surface coupling process with stark implications for sea ice properties (Stapf et al., 2020; Keen et al., 2021).

The Multidisciplinary drifting Observatory for the Study of Arctic Climate (MOSAiC) expedition was designed to address many gaps in our knowledge and to collect a wealth of data to study the changing Arctic climate system and improve model representations of this system. MOSAiC was a year-long expedition in the central Arctic starting in September 2019, wherein the German research icebreaker *Polarstern* (Polarstern, 2017) was frozen into the sea ice north of the Laptev Sea, and drifted with that ice across the Transpolar Drift for most of the following twelve months. Observational assets were onboard *Polarstern*, surrounding *Polarstern* in a Central Observatory (CO) ice camp, and across a Distributed Network (DN) of mostly autonomous observing systems, in addition to coordinated satellite and aircraft observations. A general overview of the expedition, including scientific design and logistical implementation, is forthcoming. In addition to that overview, more detailed overview papers aim to document the scientific drivers and field details for each of the primary MOSAiC science teams, including providing initial views into the data and preliminary results. These include the atmosphere (ATMOS, this paper), sea ice and snow (ICE; Nicolaus et al., 2022), ocean (OCEAN; Rabe et al., 2022), ecosystem (ECO; forthcoming), and biogeochemistry (BGC; forthcoming) teams.

The Science Plan for MOSAiC (MOSAiC, 2016) was developed over many years through cross-cutting engagement of the Arctic research community, including representatives of many disciplines, participants in past Arctic field expeditions, modeling groups focused at multiple scales, international scientific committees, and other stakeholders. As developed for that plan, the guiding science question for MOSAiC is: *What are the causes and consequences of an evolving and diminished Arctic sea ice cover?* This question places sea ice change as a clear nexus of MOSAiC research, and presents the need to address the numerous processes that are driving and responding to this change. Many of these processes intimately involve the atmosphere. To further guide and organize MOSAiC, a set of six more detailed science questions were identified, and of these five directly pertain to atmospheric processes:

1. What are the seasonally varying energy sources, mixing processes, and interfacial fluxes that affect the heat budgets of the Arctic atmosphere, ocean, and sea ice?
2. How are sea ice formation, drift, deformation, and melting coupled to atmospheric, oceanic, and ecosystem processes?
3. What are the processes that regulate the formation, properties, precipitation, and lifetime of Arctic clouds and their interactions with aerosols, boundary layer structure, and atmospheric fluxes?
4. How do interfacial exchange rates of biogeochemical process-related trace gases trigger the Arctic climate system?
5. How do ongoing changes in the Arctic climate system impact large-scale heat, momentum, and mass fluxes, and how do these changes feed back into the Arctic climate and ecosystem?

This set of questions draws upon all aspects of the Arctic atmosphere and provides strong guidance for the types of observations and activities that comprised the atmospheric program for MOSAiC. Many key processes that were studied are portrayed schematically in Figure 1. These can be separated into the four broad categories of atmospheric physical and dynamical structure, clouds and precipitation, gases and aerosols, and energy transfer. Many of these processes represent direct linkages to other components of the highly coupled Arctic system. For example, transfer of atmospheric momentum to the surface impacts sea ice movement and deformation as well as upper ocean circulation, while gas fluxes represent a biogeochemical linkage from the ocean and ice to the atmosphere. Interactions like these between the atmosphere and the rest of the coupled system are plentiful, represent some of the largest uncertainties in our understanding of the Arctic as a whole, and must be clarified to understand the future trajectory of the Arctic system.

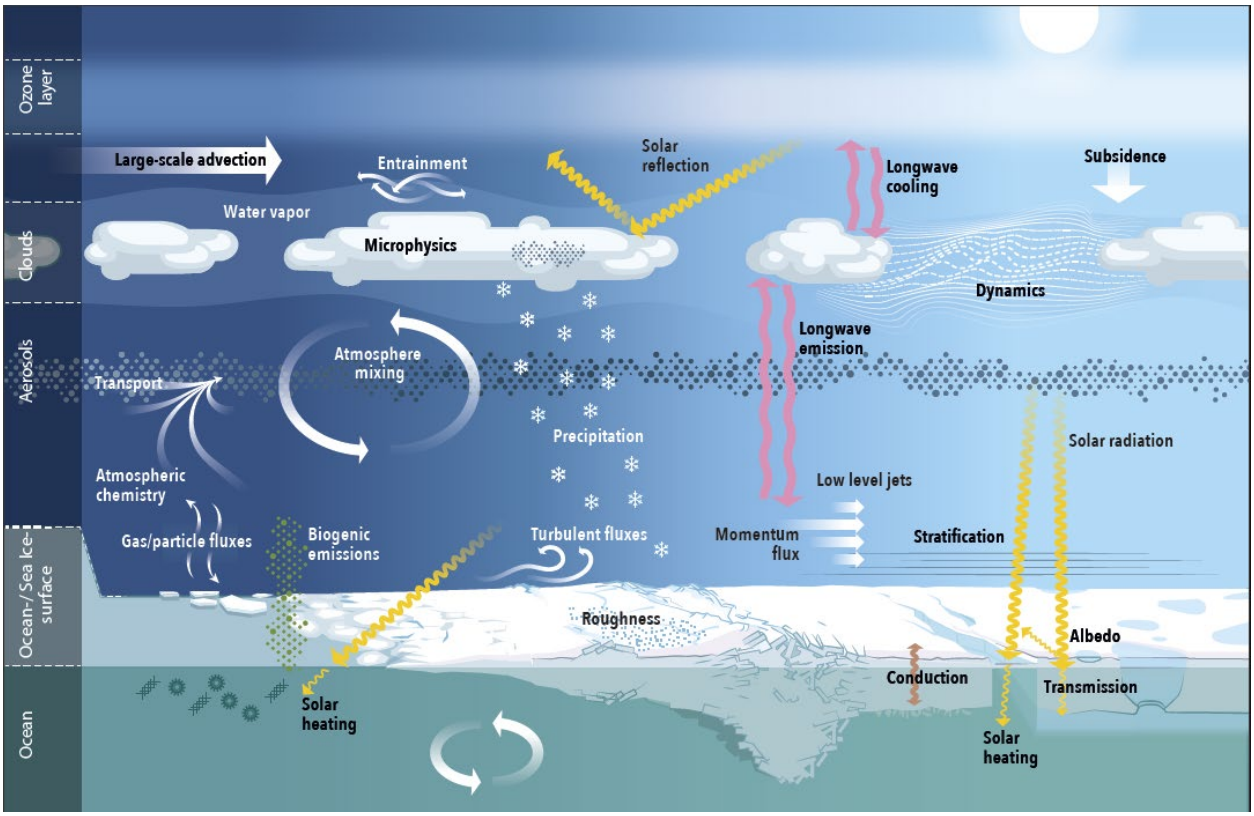

Figure 1. Atmospheric processes over the Central Arctic.
Depicted are the primary zones and processes examined by the atmosphere team during the year-long MOSAiC expedition that began in September 2019.

2. Methods and observational program

Two words appropriately describe the atmospheric observational program during MOSAiC: comprehensive and complementary. The observational suite and sampling activities were intentionally designed to provide the most comprehensive view of atmospheric processes in the central Arctic to date. Redundancy was employed in targeted ways to ensure continuity and consistency for many critical measurements, and to enable assessment and intercomparison of techniques. Most of the atmospheric team activities were also organized in a way to facilitate cross-disciplinary research with the other MOSAiC teams. The ATMOS team itself was organized around a collection of participating projects. Typically, each of these projects provided field personnel to support their individual projects, leading to strong continuity, while some cross-project support and collaboration was essential to implement the full atmospheric program and to ensure strong linkages with other MOSAiC teams. In this section the atmospheric observational program, including the contributing projects, is described in detail. A list of participating institutions is provided in Appendix A.

2.1 ATMOS observations at multiple scales

The MOSAiC expedition drifted across the central Arctic for approximately a full year, and was organized around five “Legs” with distinct groups of participants (Figure 2). Observational

activities and installations from the ATMOS team took place in numerous locations across the MOSAiC observational domain, including onboard *Polarstern*, in a Central Observatory within about 2 km of *Polarstern*, and in a Distributed Network at larger distances. Additionally, atmospheric measurements were made from aircraft flying at large distances from the other observational locations, and across the Arctic Basin in an Arctic Water Isotope Network (AWIN). The initial installations occurred in early October 2019 in the northern Laptev Sea on unusually thin sea ice compared to prior years (Krumpen et al., 2020), yet remained largely intact while drifting across the central Arctic through mid-May 2020, with minor spatial changes due to local ice dynamics. This period included Legs 1 through 3. *Polarstern* then left the MOSAiC floe from mid-May to mid-June 2020; during this period a subset of equipment was left behind to maintain some basic observations at the MOSAiC ice floe, while most equipment onboard *Polarstern* continued making measurements as the ship transited to Svalbard and back. From the middle of June through the end of July (much of Leg 4), the vessel was again attached to the original MOSAiC floe, albeit at a different location on the floe and with a newly established CO. Then, after the disintegration of the floe close to the ice edge in Fram Strait, scientific equipment was again removed from the ice and *Polarstern* transited to an entirely new ice floe near the North Pole and established a new CO for late August through late September (Leg 5).

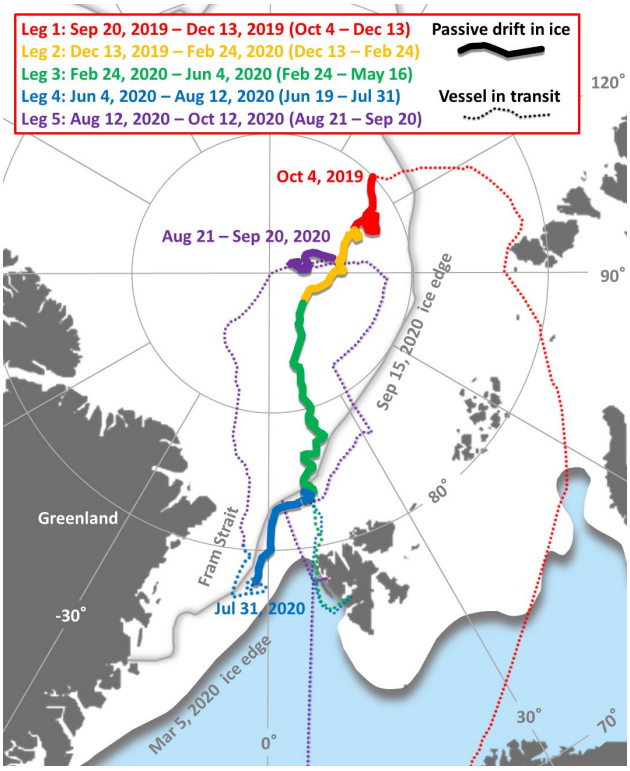

Figure 2. Expedition track distinguished by leg.
Periods of passive drift by *Polarstern* (solid) and periods of transit when the vessel was underway (dotted) are distinguished. The inclusive dates for each of the five, color-coded expedition legs are given in the legend, with the second set of dates in parentheses being the dates spent in passive drift with an ice floe. The approximate sea ice edge at the annual maximum (Mar 5, 2020) and minimum (Sep 15, 2020) is also provided.

During the full year in the Arctic, *Polarstern* served as a platform to support many atmospheric observational and sampling systems. Atmosphere-observing instruments are often large and sophisticated, or operated as observational suites from within sea-container-based laboratories. They often protrude up into the atmosphere, or must have an unobstructed view of the sky from various angles. Thus, the vessel itself served as a stable platform for these intensive operations (Figure 3). The helicopter deck towards the aft of the vessel was the platform for launching routine radiosondes and other research balloons, with a dedicated balloon-filling station directly adjacent to this deck. The *Polarstern* P-deck, above and directly aft of the bridge, offered a suitable location for a large collection of sky-observing systems, some of which viewed vertically, while others viewed the sky over a range of angles. On the foredeck, numerous stacked sea-containers housed a major collection of atmospheric instrumentation, including those for observing the sky and those for sampling air. Additionally, a tower mounted from the *Polarstern* bow crane allowed for measurements to be made forward of the vessel. Some of these measurements were linked with cabling and tubing to an additional sea-container laboratory installed below deck in the forward cargo hold.

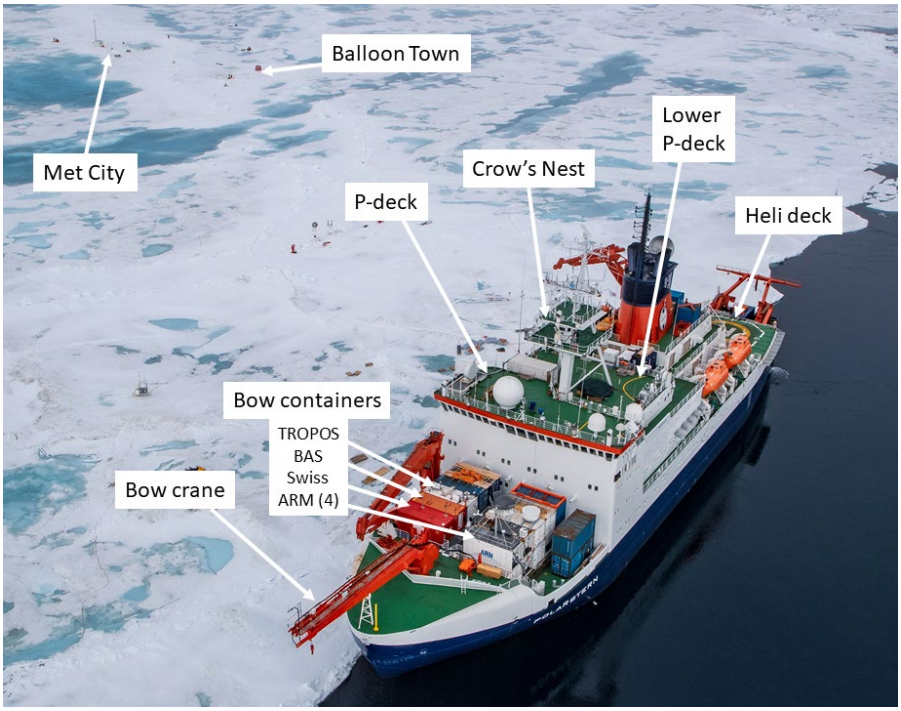

Figure 3. *Polarstern* during July 2020, with key observing locations for the ATMOS team highlighted.
Bow containers included instruments provided by institutions TROPOS, BAS, Swiss and ARM (abbreviations defined in Appendix A). Photo credit: Lianna Nixon.

The vessel itself can adversely influence the measurement of some atmospheric processes, such as turbulence, and does not allow for access to undisturbed sea ice surfaces. To support coupled system research, atmospheric measurements made nearby those being made of other components of the system was advantageous. For these reasons, a collection of atmospheric observational activities also took place on the sea ice itself within about 2 km of *Polarstern* in the MOSAiC CO (Figure 4); three different COs were established over the course of the year. A centerpiece of

the CO was Met City, which housed numerous atmospheric measurements as well as some targeting the sea ice, snow, ocean, and ecosystem. This key observation site was far enough from *Polarstern* to limit adverse impacts on the measurements, while still allowing a physical powerline connection most of the time and typically visual observation of the site from the *Polarstern* bridge (Figure 4).

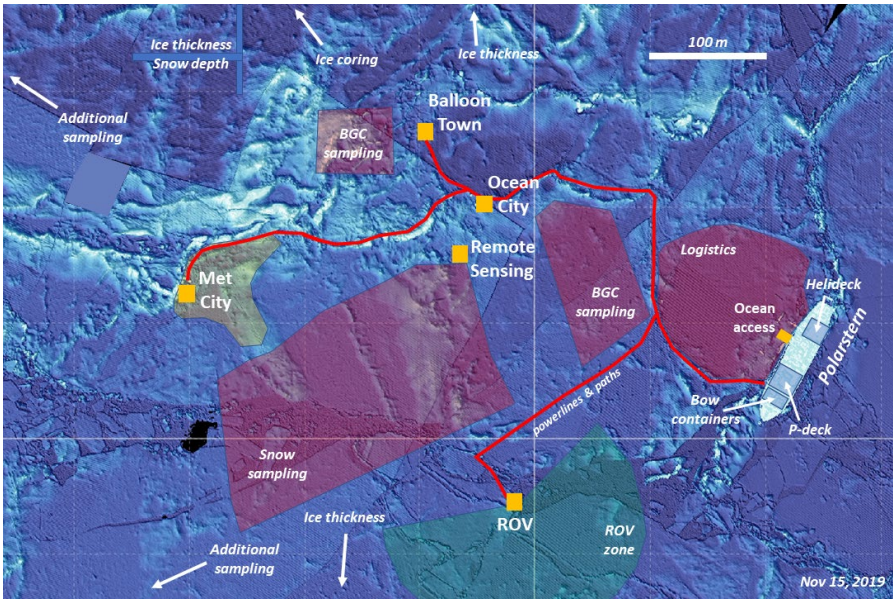

Figure 4. Main installations in the MOSAiC Central Observatory on November 15, 2019. This configuration of the Central Observatory is provided as a conceptual example; while it accurately represents the initial installation during Leg 1, ice dynamics and logistics dictated many changes over the course of the expedition. BGC refers to Biogeochemistry; ROV, to remotely operated vehicle.

Other key locations in the CO included Balloon Town and the numerous Drone airports, which supported observing platforms offering insight into the lower atmospheric profile structure. Balloon Town served as the hub for flying tethered balloons at a safe distance from *Polarstern*. During all expedition legs, the 9-m^3 tethered balloon named Miss Piggy was operated, with a maximum payload of 4 kg. For Leg 4, the BELUGA balloon (Balloon-bornE modular Utility for profilinG the Atmosphere; Egerer et al., 2019) was also operated, with its 90-m^3 size supporting an instrument payload of up to 15 kg. Operation of these tethered balloons was restricted to suitable flight conditions, which included the absence of significant icing and near surface winds below approximately 7 m s^{-1}. Multiple airports for uncrewed aircraft systems (UAS) were established across the CO starting in March 2020 to enable observations of different surface types and coordination with other surface-based measurements. Three UAS were deployed episodically from these locations: the DataHawk2 fixed-wing aircraft, HELiX multi-rotor system, and Spectra quadcopter. Additional atmospheric sampling and measurement activities occurred at many locations across the CO for targeted sampling of gases, aerosols, energy fluxes, temperature profiles, and more.

Collectively, the CO and associated installations were established on three distinct occasions due to required movements of *Polarstern*. The positions of CO installations relative to *Polarstern* for each of these installations are summarized in Table 1. At times installations moved relative to each other due to ice dynamics, which also led to periodic power interruptions and thus discontinuities in the data. Observations onboard *Polarstern* were continuous and without power interruptions. Collectively, the *Polarstern* and CO served as an intensive, process-based observatory. The resultant observations provide a detailed and comprehensive characterization of the atmospheric system and its interactions that is specifically appropriate for direct linkage to high-resolution model studies and to individual columns in large-scale models.

Table 1. Primary ATMOS team observing locations, with approximate locations and headings relative to *Polarstern*

Site	Leg	Distance (m)	Heading (deg)
Met City	1–3	300–600	0–60
Met City	4	400	130
Met City	5	375	130
Balloon Town	1–3	380	90
Balloon Town	4	250–300	135
Balloon Town	5	370	115
Drone #1	3	200	30
Drone #2	3	600	90
Drone #1	4	600	40
Drone #2	4	135	140

Reaching beyond the local domain of the CO, the ATMOS team had limited installations across the MOSAiC Distributed Network. The primary installations were at the three most comprehensive sites, called L sites, which were initially located 13–23 km from *Polarstern* at nominally 120˚ intervals around the vessel. Additionally, some atmospheric measurements were made onboard the helicopter-borne meteorological sensor system called HELiPOD, which was flown on 25–60 km transects across the MOSAiC domain on five flights during May through July. Lastly, a variety of atmospheric measurements were made during a coordinated aircraft campaign based in Svalbard during the final weeks of MOSAiC.

Observations at these wider spatial scales were implemented to provide key information on variability of the atmospheric system at spatial scales comparable to the typical size of a model grid cell, as well as to capture spatial gradients and transitions, to understand the spatial evolution of the atmosphere, and to distinguish between advective and locally evolving processes. The aircraft campaign targeted air masses and their transformation in space and time, sometimes using modeled back- or forward-trajectories to relate aircraft measurement to those made at *Polarstern*. Finally, the MOSAiC atmospheric observations were in many cases designed to link directly with other key observatories across the Arctic to better characterize pan-Arctic patterns and variability. Of particular note here are the fixed atmospheric observatories at Ny-Ålesund, Svalbard; Utqiagvik, Alaska; Eureka, Canada; Summit Station, Greenland; and others (e.g., Uttal et al., 2016), which served as a model for many MOSAiC observations. Importantly, many observing activities at these stations and elsewhere across the Arctic ramped up during MOSAiC and in prior years as part of the coordinated Year of Polar Prediction

(YOPP) initiative organized by the Polar Prediction Project of the World Meteorological Organization.

2.2 Atmospheric physical structure measurements

Measurements of the physical structure of the atmosphere – temperature, humidity, wind speed and direction, and turbulence – provide an essential context for interpreting many of the other measurements, far beyond their primary application to atmospheric dynamics. They span an hierarchy of temporal and spatial scales, and include continuous measurements, discrete but regularly scheduled, and sporadic sampling (see Figure 5 and Table B1 in Appendix B).

The backbone of the atmospheric structure measurements is provided by the radiosounding program. Radiosondes were launched at least every 6 hours throughout the entire duration of MOSAiC, including periods when *Polarstern* was in transit. Conforming to the requirements of Global Climate Observing System Reference Upper-Air Network (GRUAN) post-processing, additional pre-launch ground checks of the radiosondes were conducted, and data were transmitted to the Global Telecommunications System (GTS) for assimilation by operational weather forecast models. The radiosoundings provide vertical profiles of temperature, relative humidity (RH), pressure, and winds from 12 m (the altitude of the helideck from which they were launched) up to an altitude of about 30 km, thus covering both troposphere and lower stratosphere. The sounding frequency was increased to 3-hourly during periods that were of particular interest dynamically, such as storm systems, or during intensive measurement periods coordinated with YOPP. On a roughly monthly basis, a cryogenic frost-point hygrometer sonde for measurements of stratospheric water vapor was added to the radiosonde package.

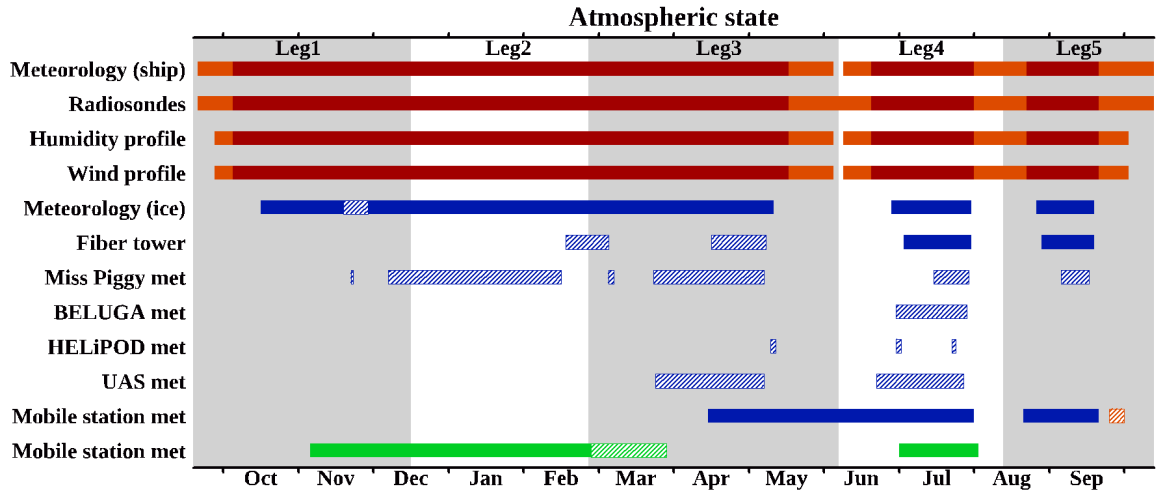

Figure 5. Temporal coverage of atmospheric state measurements in different categories. The different colors represent the following: red, onboard *Polarstern* while at MOSAiC ice floe; orange, onboard *Polarstern* while underway; blue, on sea ice in the Central Observatory; green, on sea ice in the Distributed Network. Solid bars are continuous measurements with minimal gaps. Hatched bars are intermittent or periodic measurements. The time spans from late September 2019 through early October 2020.

Atmospheric water vapor was also measured using ground-based remote sensors operated from the *Polarstern* bow and P-deck. Four microwave radiometers (MWR) measured microwave brightness temperatures at a variety of narrow microwave frequency bands that contain information on the vertically integrated water vapor. These include a two-channel system with measurements at approximately 23 and 31 GHz and a three-channel system that also includes measurements near 90 GHz. The Humidity and Temperature Profiler (HATPRO) has seven channels each between 22–31 GHz and 51–58 GHz, which adds the ability to derive coarsely resolved humidity and temperature profiles through the lower troposphere. Extending to much higher frequencies, the Microwave Radiometer for Arctic Clouds observes multiple channels near 183, 243, and 340 GHz that are better suited to observe low water vapor amounts in Arctic winter. Additionally, when combined with radiosonde temperature information, the multi-wavelength lidar (PollyXT) uses the Raman technique to derive continuous profiles, up to approximately 6 km, of water vapor mixing ratio during polar night. Lastly, direct measurements of water vapor isotopes were made from air sampled on the *Polarstern* P-deck as well as across the Arctic Basin at 20 or more sites in northern Alaska, Greenland, Finland, Svalbard and elsewhere as part of the AWIN. These isotopic measurements provide geochemical fingerprints of moisture transported into, within, and out of the Arctic as well as providing insight into surface moisture exchange processes (e.g., Galewsky et al., 2016; Bailey et al., 2019).

For studies of atmospheric boundary layer (ABL) processes, in particular those related to turbulent dynamics, a high temporal resolution is required. To address this particular aspect, a suite of remote sensing instruments was deployed, both on *Polarstern* and on the ice, to provide continuous sampling of lower atmosphere winds. Multiple Doppler lidars operated in different modes to provide information on both mean and turbulent winds. One Doppler lidar observed continuous wind profiles using the velocity-azimuth display (VAD) technique over the full year from the P-deck, while a second operated on the *Polarstern* bow mainly in vertical stare mode, measuring vertical velocity on a continuous basis to retrieve the turbulent dissipation rate (O'Connor et al., 2010), with only periodic horizontal wind profiles. Two additional Doppler lidars made range-height indicator scans at multiple azimuth angles, ensuring frequent scans oriented close to the mean wind direction. These enable the retrieval of profiles of turbulent kinetic energy (Banta et al., 2006). Periodic, short VAD scans by these systems added additional spatial perspectives on the wind profile and allowed for cross-comparisons among instruments. One system operated continuously from P-deck, overlooking the CO, while the other system was deployed on the ice until May 2020, then moved to the P-deck for May onwards. These two scanning lidars were also intermittently operated in a virtual tower mode (Calhoun et al., 2006).

Further wind information came from a 1290-MHz Beam-Steerable Radar Wind Profiler that was operated continuously from the *Polarstern* bow. This system provides Doppler spectra and moments along multiple beams, from which hourly vertical profiles of wind speed and direction are derived. The beam-steerable nature of the system made it robust to shifts in the level of *Polarstern*. Additional horizontal wind information, and atmospheric divergence, can be derived from hydrometeor movements observed by the Ka-band Scanning ARM Cloud Radar located on the *Polarstern* P-deck at distances out to 20 km. Finally, a phased-array Doppler sodar was installed at Met City. In addition to profiling low-level winds on the ice, the sodar backscatter, when calibrated with a direct measure of the surface heat flux under well-mixed conditions, can provide retrievals of temperature structure-function profiles. These profiles offer a good measure

of the surface mixed layer depth and low-level temperature inversions. Turbulent quantities, such as velocity variances, can also be retrieved.

While the radiosondes provide valuable information about thermodynamics, kinematics, and the synoptic background state of the atmospheric column above the floe, they do not cover the near-surface layer. This gap is filled with measurements made in the ice camp. Temperature, relative humidity, and wind measurements were made at Met City at nominal heights of 2, 6, and 10 m on a 10-m tower and at 30 (before mid-November) or 23 m (after mid-November) on a separate mast that was operated during Legs 1–3. A similar meteorological measurement suite was operated at about 29 m onboard *Polarstern*, and was possibly influenced by the ship itself. Additionally, during Legs 2–5, temperature measurements at 60-cm vertical resolution were made using a fiberoptic-based Distributed Temperature Sensing system (Thomas et al., 2012) installed vertically along a 10-m telescoping "Fiber" tower.

High resolution, in-situ boundary layer observations up to about 1.5 km were periodically performed at Balloon Town with instruments installed on tethered balloons. Throughout the entire expedition, Miss Piggy was operated using a tethersonde system to obtain standard flight-level measurements of temperature, humidity, wind, and height. Operated either in "profiling" or "stationary at height" mode, numerous additional instruments were periodically attached to the balloon. Among those was a Distributed Temperature Sensing system like that operated near the surface, offering high-resolution temperature profiles to characterize turbulent boundary layer processes. Turbulence was also measured episodically during Legs 1–3 using a one-component hot-wire anemometer probe. During Leg 4, BELUGA operated in "profiling mode" making 1-m vertical resolution measurements of temperature, humidity, and winds both inside and outside of clouds up to 1.5 km. This balloon also flew an ultrasonic anemometer to examine cloud-induced mixing processes.

During Legs 3 and 4, UAS were operated from the sea ice over the CO. To document the thermodynamic structure of the atmosphere, these systems measured pressure, temperature and humidity with similar sensors to those employed on the radiosondes. Additionally, the DataHawk2 carried a finewire array to collect very high-resolution observations of temperature and air velocity, from which to derive turbulence parameters. A pair of IR temperature sensors provided information on surface features, such as leads, that the aircraft flew over, as well as cloud cover, as the aircraft sampled the atmosphere beneath the clouds. Profiling through a variety of stability regimes, the DataHawk2 collected information on strong inversions, low-level jets, warm air intrusions and other features. Some flights also sampled the influence of small leads on the atmosphere structure.

2.3 Cloud and precipitation measurements

The characterization and quantification of different cloud and precipitation parameters was a high priority during MOSAiC because these parameters play substantial roles in the Arctic system. They impact the radiative balance and temperature throughout the troposphere and at the surface, help to shape the atmospheric turbulent structure, and are strongly linked to aerosol populations. Precipitation is the primary sink of atmospheric moisture and snowfall represents an important link to the surface via accumulation and wet deposition.

The MOSAiC cloud observing suite (see Figure 6 and Table B2 in Appendix B) was designed to characterize the macro- and microphysical properties of clouds and precipitation from the lower stratosphere down to the surface. Most cloud-sensing instruments are large and sophisticated, and thus were typically installed onboard *Polarstern* with a clear view of the sky, either pointing vertically or at various scanning angles. Some measurements, specifically for precipitation, were also made from the sea ice. The overall suite of cloud and precipitation measurements benefitted from two significant facilities onboard: the ARM Mobile Facility and the OCEANET-Atmosphere facility.

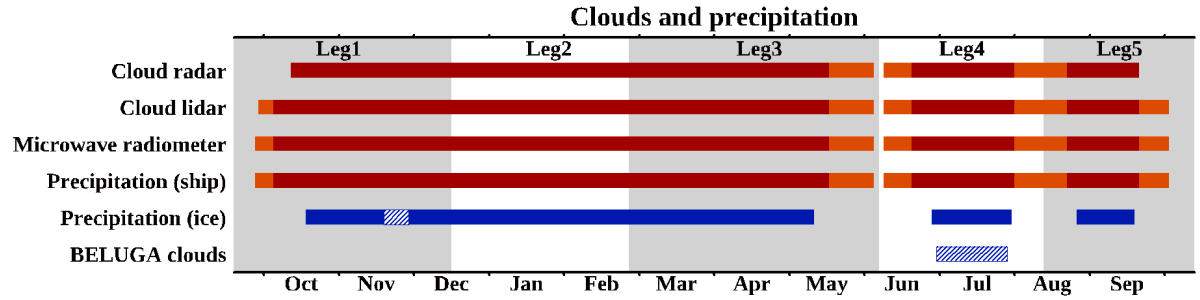

Figure 6. Temporal coverage of cloud and precipitation measurements in different categories.
The different colors represent the following: red, onboard *Polarstern* while at MOSAiC ice floe; orange, onboard *Polarstern* while underway; blue, on sea ice in the Central Observatory. Solid bars are continuous measurements with minimal gaps. Hatched bars are intermittent or periodic measurements. The time spans from late September 2019 through early October 2020.

Surface-based, active remote sensors were an important backbone of the cloud-observing program. Cloud Doppler radar measurements at two wavelengths were made using the Ka-band ARM Zenith Radar (KAZR), Marine W-band ARM Cloud Radar, and Ka-band Scanning ARM Cloud Radar. The first two of these viewed vertically from the bow, while the third was installed on the P-deck and performed a dedicated scanning strategy that included a series of plan position indicator scans at multiple elevation angles and range-height indicator scans at multiple azimuth angles to characterize the spatial distribution of cloud properties. All of these radars measure the radar moments, including reflectivity, mean Doppler velocity, and spectrum width, which provide insight into the mass, size, and fall speed of cloud and precipitation particles. Additionally, the vertically pointing radars record the full Doppler spectrum, which offers further insight into hydrometeor populations and processes. Lidar measurements were made using the multiwavelength Raman lidar PollyXT, the High Spectral Resolution Lidar, and the Micropulse Lidar, all operated from the *Polarstern* bow. These lidars measure backscatter cross-section, which provides information about the size of atmospheric particles, and depolarization ratio, which allows discrimination of particle shape and thus phase. In addition, the PollyXT and High Spectral Resolution Lidar measure extinction independently from backscatter and can thus be used for aerosol typing. PollyXT also measures depolarization by multiple scattering from liquid clouds at two different fields-of-view (i.e., viewing-angle geometries) to derive cloud-droplet number concentration, effective radius, and liquid water content near the cloud base. In addition to these more sophisticated lidar systems, multiple ceilometers were operated on the *Polarstern* P-deck to provide relative backscatter and cloud base height.

These active sensors were complemented by a collection of passive sensors operated in close proximity. The four MWRs collectively provide many measurements to derive the vertically integrated cloud liquid water path (LWP), including a number of higher frequencies that are well suited to derive small LWPs as well as providing information on the cloud ice-water content. At infrared frequencies, the Marine Atmospheric Emitted Radiance Interferometer installed on the P-deck measures the spectrum from 520 to 3300 cm^{-1}, providing information suitable for deriving cloud radiative and microphysical properties, as well as atmospheric thermodynamic structure and trace gas concentrations. In addition, two Total Sky Imagers obtained hemispheric visible sky images from the P-deck and the bow to document the cloud spatial distribution and sky coverage.

Measuring snowfall is notoriously difficult, particularly in windy, blowing snow environments. To address this challenge numerous measurements of precipitation occurrence and intensity were made both from the *Polarstern* and at Met City. The on-ice suite consisted of a Present Weather Detector, laser disdrometer, and a weighing bucket, with the latter two installed within double Alter shields. Measurements made onboard *Polarstern* included a Present Weather Detector, laser disdrometer, and a Siphon rain gauge on the P-deck, complemented by 1- and 2-dimensional laser disdrometers on the bow. While possibly suffering other challenges due to the ship infrastructure, these onboard measurements were likely less affected by blowing snow than the measurements made at Met City (Wagner et al. 2021).

In-situ measurements of precipitation particles were made by a Video In-Situ Snowfall Sensor, which was initially installed at Met City but then moved to the *Polarstern* P-deck at the end of April for the rest of the expedition. Similar measurements were made from the BELUGA tethered balloon during Leg 4 using a Video Ice Particle Sampler, which is also sensitive to cloud particles. Images from both of these systems provide information on particle shape and size. Lastly, snow particle concentrations in multiple size bins were measured near the surface and at 10 m from the Met City tower; these measurements were specifically designed to help distinguish falling from blowing snow.

The direct measurements from this collection of cloud and precipitation-sensing instruments can be used to derive many higher-order products to characterize important geophysical parameters. Radar, lidar, ceilometer, microwave radiometer, and radiosonde measurements all contribute to unified cloud property retrieval packages (Illingworth et al., 2007; Shupe et al., 2015), which provide a continuous time-height characterization of cloud phase and microphysical properties. Furthermore, lidar estimates of aerosol properties near clouds can be linked to cloud-droplet size and number and to ice crystal number concentrations within the clouds. From the thermodynamic state measured by radiosondes and from observations of ice clouds, relevant freezing processes (homogenic and heterogenic) can be revealed. Cloud radar radial velocities and Doppler spectra offer information on vertical wind motions within clouds (Shupe et al., 2008), dynamic forcing of clouds and precipitation (Matejka and Srivastiva, 1991), and ice water content and flux (Bühl et al., 2016). Temporal variability in radar velocity measurements are the basis to derive turbulent dissipation rate associated with clouds (O'Connor et al., 2005). Similarly, cloud radar measurements are used to derive continuous estimates of snowfall rate (e.g., Matrosov, 2007), which can be compared and constrained using the various surface precipitation sensors.

2.4 Gas and aerosol measurements

Atmospheric concentrations and exchange fluxes of aerosol and trace gases are coupled to chemical and biological processes in snow, sea ice, and the ocean, and are strongly dependent on regional and long-range transport, air mass evolution, and atmospheric mixing. Aerosols and their precursors emitted above sea ice regions may impact climate by direct and indirect radiative effects through interaction with clouds. Photochemical release of reactive chemical species such as halogens from snow, ice and aerosol influences atmospheric composition and oxidizing capacity. Finally, the sign and magnitude of exchange fluxes of greenhouse gases (such as carbon dioxide, methane, nitrous oxide) determine the role of sea ice covered regions as a respective source or sink. In general, air-sea and air-ice interactions, the role of sea ice and snow as a chemical reservoir or aerosol source, and the influence of air-sea exchange on regional atmospheric composition and cloud properties are all poorly understood.

A complementary suite of in-situ gas and aerosol measurements and sampling was implemented at various locations on the ship and ice floe. Together, these give a comprehensive picture of near-surface concentrations of greenhouse gases and reactive trace gases, aerosol precursors, aerosol size distribution and number concentration, aerosol chemical composition and morphology, aerosol optical and hygroscopic properties, and aerosol-cloud interactions. Additionally, a subset of gas and aerosol properties were measured intermittently above the surface using multiple airborne platforms. Finally, physical samples of precipitation, surface snow, sea ice, and upper ocean water were obtained in coordination with other MOSAiC teams to characterize potential sources and sinks of climate-active trace gases, aerosol precursors, and aerosols. A more detailed overview of the gas and aerosol measurements conducted during MOSAiC is given in Figure 7 and Tables B3, B4, and B5 in Appendix B.

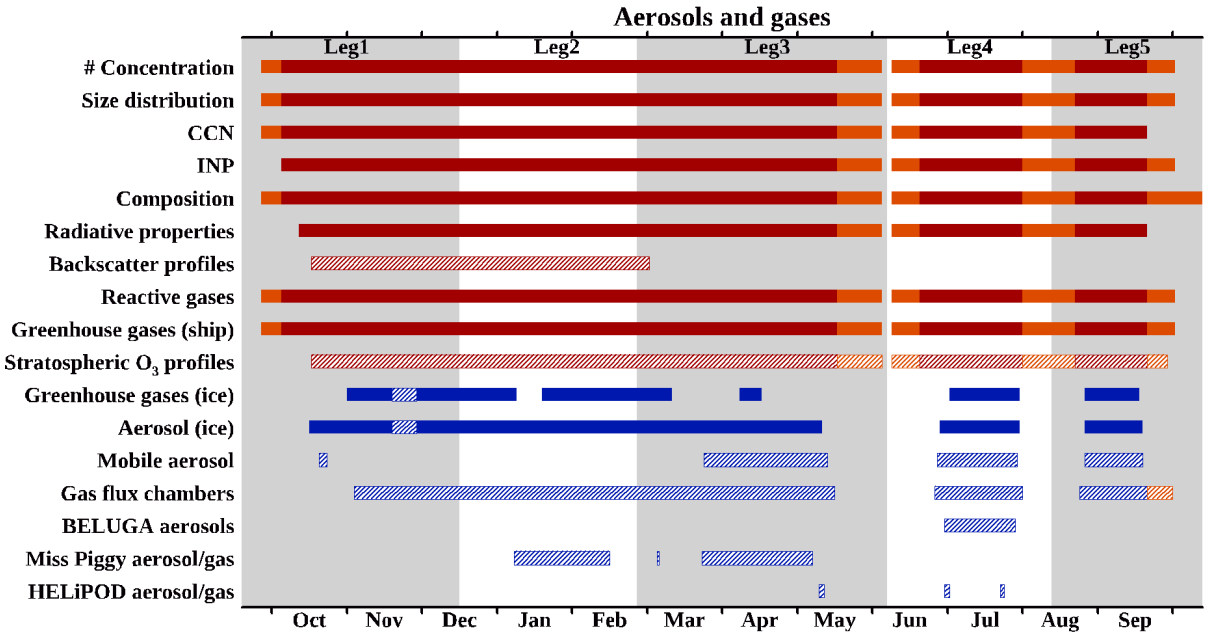

Figure 7. Temporal coverage of gas and aerosol measurements in different categories. The different colors represent the following: red, onboard *Polarstern* while at MOSAiC ice floe; orange, onboard *Polarstern* while underway; blue, on sea ice in the Central Observatory. Solid bars are continuous measurements with minimal gaps. Hatched bars are intermittent or periodic measurements. The time spans from late September 2019 through early October 2020.

Trace gas measurements included the primary greenhouse gases: carbon dioxide (CO_2), methane (CH_4), nitrous oxide (N_2O), and sulfur hexafluoride (SF_6); selected reactive gases: ozone (O_3), dimethyl sulfide (DMS), volatile organic compounds (VOCs), carbon monoxide, sulfur dioxide (SO_2), halogenated VOCs (h-VOCs), nitrogen oxides ($NO/NO_2/NO_y$), and gaseous elemental mercury (Hg^0); and anthropogenic chlorofluorocarbon tracers (CFCs). Continuous gas analyzers on the ship drew sample air from inlets on the *Polarstern* bow. These measurements span a range of time scales from 10 Hz to 3-hourly. In addition, weekly flask samples were collected on site for post-cruise greenhouse gas and hydrocarbon analysis by the NOAA Global Monitoring Laboratory (GML) and the University of East Anglia. For CO_2, CH_4, Hg^0, O_3 and carbon monoxide, there were continuous analyzers operating at several locations on the ship. Cross-calibration of greenhouse gas measurements was done with reference to flask samples analyzed by the NOAA GML reference lab. CO_2, CH_4, and carbon monoxide were calibrated regularly on board with reference gas cylinders. Atmospheric O_3 profiles from the surface to the middle stratosphere were also obtained from weekly balloon-borne ozonesondes, with increased frequency during the spring ozone loss season, while lower-troposphere ozone profiles were obtained periodically from Miss Piggy tethered balloon profiles made from January to May.

To assess air-sea trace gas exchanges, eddy covariance (EC) turbulent flux systems for CO_2, CH_4, DMS, and O_3 were deployed on the *Polarstern* bow tower. An additional CO_2-CH_4 EC system was operated from the Met City tower. Continuous EC fluxes were computed over hourly timescales with a footprint extending hundreds of meters upwind from the measurement location. Fluxes of CO_2, CH_4, and DMS were also obtained at shorter temporal and spatial scales and higher sensitivity with flux chamber systems (dynamic and static) deployed several times per week on both ice and water surfaces.

The composition of gas phase precursors for aerosol formation, e.g., sulfuric acid, methanesulfonic acid, and iodic acid, was monitored using a nitrate-based Chemical Ionization Atmospheric Pressure interface Time-Of-Flight mass spectrometer (Jokinen et al., 2012), sampling from a specifically designed new particle formation inlet (Baccarini et al., 2020) on the *Polarstern* bow. A second similar mass spectrometer, but without a chemical ionization unit, was operated to monitor the composition of atmospheric ions from a second specific inlet.

Aerosol measurements spanned a wide array of physical, chemical, optical, and microphysical properties using both online and offline techniques. Aerosol size distributions and number concentrations were measured at various locations during the campaign. Continuous aerosol size distribution measurements were performed on the *Polarstern* bow collectively covering the full range from 0.8 nm to 50 μm in diameter using a particle size magnifier, Neutral Cluster and Air Ion Spectrometer, two Scanning Mobility Particle Sizer (SMPS) systems, an Ultra High Sensitivity Aerosol Spectrometer, an Aerodynamic Particle Sizer (APS), a Wideband Integrated Bioaerosol Sensor, and a portable optical particle counter, along with a Cloud and Aerosol

Spectrometer deployed on the *Polarstern* crow's nest. A Compact Lightweight Aerosol Spectrometer Probe was also integrated with a sonic anemometer on the Met City tower to provide continuous in-situ measurements on the sea ice and estimates of aerosol flux and dry deposition rates. The continuous size distribution measurements were collocated with aerosol number concentration measurements of particles with diameters larger than 1 nm using particle size magnifiers and Condensation Particle Counters (CPCs) with different lower diameter detection limits. A subset of the continuous aerosol size distribution and number concentration measurements was made via a specialized inlet capable of routinely switching between modes of sampling total and interstitial aerosols, where interstitial particles are defined as those that did not activate as cloud droplets (< 1 μm) when *Polarstern* was in fog or low clouds.

Detailed aerosol chemical composition was measured throughout the campaign by several methods. Continuous online measurements of aerosol chemistry were performed using a high-resolution aerosol mass spectrometer and an Aerosol Chemical Speciation Monitor. Other aspects of aerosol chemical composition were also assessed using specialized instrumentation, including a Wideband Integrated Bioaerosol Sensor for measuring fluorescent particles, and an aethalometer and Single Particle Soot Photometer for characterizing properties of equivalent and refractory black carbon.

Various optical properties associated with aerosols were characterized during the campaign. Light scattering and absorption measurements were continuously monitored at three wavelengths for dry aerosol particles using a nephelometer and a Particle Soot Absorption Photometer, respectively.

Aerosol hygroscopic properties were monitored on the *Polarstern* bow using a Humidified Tandem Differential Mobility Analyzer for measurements below water saturation (RH < 100%). Two continuous flow chamber cloud condensation nuclei (CCN) counters for measurements above water saturation (RH > 100%) provided information on aerosol hygroscopicity, microphysical properties, and potential cloud activity at both fixed and variable supersaturations. Furthermore, a Spectrometer for Ice Nuclei was episodically operated in April–May to characterize deposition and immersion mode ice-nucleating particle (INP) concentrations at variable supersaturation and temperature with high temporal resolution.

In addition to the online measurements, routine collection of aerosol loadings on filters and impactor substrates, as well as in physical ice, snow, and water samples, was designed to support various offline chemical and microphysical analyses. Air samplers included several total suspended particulate and $PM_{2.5}$ filters that operated from daily to weekly integrations under high and low volume conditions, and Davis Rotating-drum Universal-size-cut Monitoring samplers that collected daily integrated and size-segregated aerosol loadings from 100 nm to approximately 12 μm in size. Subsequent offline analyses of these samples are used to examine major ions, trace elements, organic and stable sulfur isotope chemistry in the aerosol phase, single-particle morphology and elemental composition, DNA sequencing of biological aerosol, and immersion-freezing INP concentrations as a function of size and temperature. Dissolved and particulate matter found in ice, snow, ocean, and melt pond physical samples (see Table B5 in Appendix B) support similar offline analysis techniques to characterize chemical, biological, and ice nucleation properties (e.g., Creamean et al., 2019).

While most aerosol measurements were made onboard, opportunistic measurements were also made at a variety of locations away from *Polarstern*, offering a view into spatial and vertical variability. Short-term deployments of a CPC occurred at the ROV hut (Figure 4) in the CO, while a portable aerosol sampler with a time-resolved PM_{10} filter sampler and optical particle counter was deployed at many locations to examine surface sources of aerosols from melt ponds and leads. Measurements above the surface are extremely important to understand aerosol origins and cloud interactions in the highly stratified Arctic atmosphere. An aerosol filter sampler and optical particle counter were also periodically deployed on the Miss Piggy tethered balloon from January to May to investigate surface aerosol sources possibly associated with storms or leads. Further aerosol measurements, including number concentration, size distribution of accumulation and coarse-mode particles, and black carbon mass concentrations, were obtained from the BELUGA balloon during Leg 4. Providing both spatial and vertical information, the periodic HELiPOD missions also included optical particle counter and CPC measurements, along with absorption measurements from a Single Channel Tricolor Absorption Photometer. Lastly, during the dark season, a Compact Optical Backscatter Aerosol Detector was also included in monthly soundings to measure aerosol backscatter through the troposphere into the mid-stratosphere.

Note that nearly all gas and aerosol measurements were influenced episodically by emissions from the ship engines, snowmobiles, helicopters, and other vents on the ship. Such pollution is readily identified by various measures, including the total number concentration of small particles as well as rapid fluctuations in particle and gas (e.g., NO_x) concentrations. Wind-sector analyses also offer important context for the air samples. Intensive efforts to detect sampling periods influenced by pollution are in progress and pollution masks will be available alongside the data.

2.5 Energy budget measurements

Energy transfer at the surface is one of the fundamental ways in which the atmosphere, sea ice, and ocean are coupled, and this transfer of energy strongly influences the sea ice and upper ocean energy budgets, vertical temperature structure, growth or melt of sea ice, and photosynthetically active radiation. Key factors that influence surface energy transfer include the ABL structure, near-surface stratification, radiative impacts of moisture and clouds, atmospheric turbulent mixing, the material properties of the surface like albedo and thermal conductivity, surface temperature and emission, and the amount of available sunlight (e.g., Figure 1).

The surface energy budget, or net energy flux density at the air-ice interface, is given as:

$$F_{net} = Q_{net} - H_s - H_l + C + P \qquad \text{(Equation 1)}$$

where H_s and H_l are the upward turbulent sensible and latent heat fluxes; C is the upward conductive heat flux to the surface from below; P represents the latent heat of melting or freezing of the sea ice at the interface; and Q_{net} is the net (downward minus upward) irradiance, which expands as follows:

$$Q_{net} = \mathrm{SWD} - \mathrm{SWU} + \mathrm{LWD} - \mathrm{LWU} - \mathrm{SWT} \qquad \text{(Equation 2)}$$

where SW and LW are broadband shortwave (solar) and longwave (terrestrial) irradiance and U or D designate upward or downward, respectively. SWT is the transmitted shortwave irradiance through the surface interface. Each term in Equations 1 and 2 was measured, or can be estimated in a variety of ways, during MOSAiC. For an interface budget, $F_{net} = 0$, indicating a balance. However, for a thin but finite surface layer, as considered here, F_{net} represents a storage term and is related to changes in temperature. A full account of the heat budgets of the sea ice or upper ocean requires additional details such as the extinction profile of transmitted solar radiation and the equivalent energy balance at the ocean-ice interface, which are addressed by the ICE (Nicolaus et al., 2022) and OCEAN (Rabe et al., 2022) teams. The ATMOS team was largely responsible for radiative and turbulent heat fluxes, while also providing some perspectives on the conductive heat flux. In addition, energy fluxes above the surface, including radiative flux divergences across the ABL, influence the ABL structure, temporal changes, and the transfer of atmospheric energy to the surface. To characterize all of these processes, fluxes were observed continuously near the surface from installations on the ice and on *Polarstern*, and episodically within the lower troposphere using several airborne sensor platforms (summarized in Figure 8 and Table B6 in Appendix B).

To derive radiative fluxes (Q_{net}), multiple measurements of LWD and SWD were made within the CO, providing important redundancy and ensuring a well-constrained, robust, and continuous record of these important inputs to the system. Multiple measurements of LWU and SWU are necessary to observe variability due to spatial heterogeneity in surface characteristics. Broadband pyranometers (SW) and pyrgeometers (LW) were deployed facing the sky in triplicate on the *Polarstern* P-deck and bow. On the ice, these same measurements along with their surface-facing complements were made continuously at Met City, including redundant measurements at other locations in the CO. These on-ice measurements also allowed for continuous observations of surface albedo and surface (radiometric) skin temperature that link with similar observations made by the ICE team. Stations on the ice were moved only when necessary due to ice dynamics, ridging, or camp re-locations.

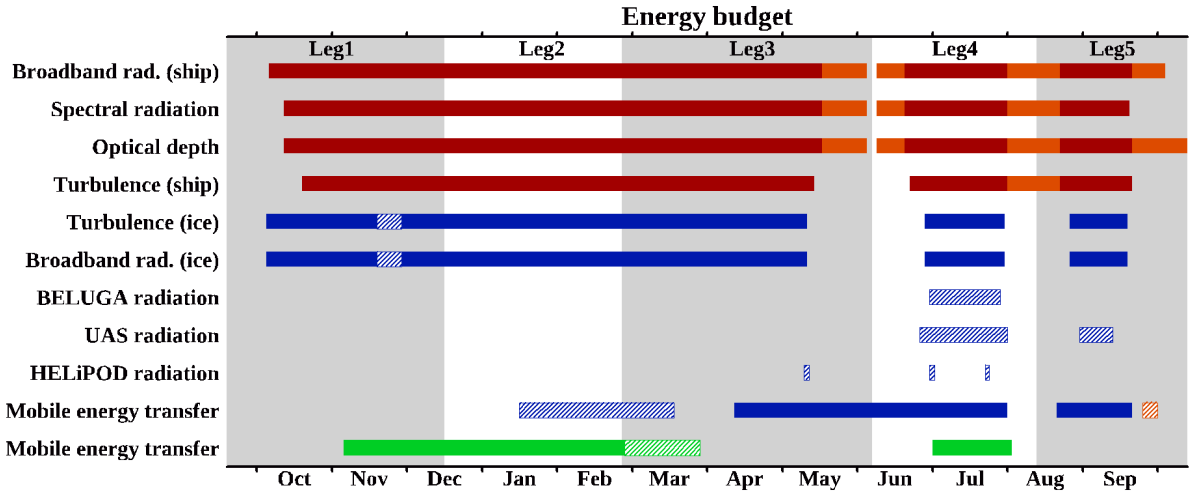

Figure 8. Temporal coverage of energy budget measurements in different categories.

The different colors represent the following: red, onboard *Polarstern* while at MOSAiC ice floe; orange, onboard *Polarstern* while underway; blue, on sea ice in the Central Observatory; green, on sea ice in the Distributed Network. Solid bars are continuous measurements with minimal gaps. Hatched bars are intermittent or periodic measurements. The time spans from late September 2019 through early October 2020.

In addition to the fixed stations, several mobile stations were used to measure time series of surface albedo, surface skin temperature, and all components of Q_{net}. Three Atmospheric Surface Flux Stations (ASFS) were deployed on a semi-continuous basis to characterize the spatial variability at local scales (within the CO) and mesoscales (as far as the L-sites in the DN). Opportunistic measurements were also made for targeted experiments using the ASFS and similar mobile radiation measurement suites. The targeted studies were often in coordination with the ICE team (Nicolaus et al., 2022), which also made radiometric measurements above, within, and below the ice. For example, helicopter infrared surface temperature mapping was done in the CO during Legs 1–3, radiative fluxes over refreezing melt ponds were observed during Leg 5, melt pond albedo measurements were made regularly during Legs 4 and 5, and observations along short transects over variable ice surfaces were made during Leg 5.

To complement the broadband radiation measurements, several narrow-band, spectral, and partitioned observations were made that provide more detailed information about emitted and scattered radiation. For example, principles like surface albedo and atmospheric emission can be highly spectrally dependent, with important implications for atmospheric composition, energy balance, photochemistry, and biological processes. Narrow-band measurements of the sky and surface infrared brightness temperature were made continuously using 8–14 μm infrared thermometers stationed at Met City and the ASFS, from which the thermodynamic temperature of the surface is derived. Similar observations were made episodically from DataHawk2 and HELiX UAS, as well as HELiPOD. From *Polarstern*, high spectral resolution infrared (450–3000 cm^{-1}), narrow field-of-view observations were made continuously using the Atmospheric Emitted Radiance Interferometer, including two sky and two surface views. These measurements provide information on surface and sky (brightness) temperature that can be used to derive emissivity, cloud, and trace gas properties. The COmpact RAdiation measurement System (CORAS) provided a similar spectral view in the near-infrared and visible (300–2200 nm) from March 2020 through the end of the expedition, giving insight into the radiative effects and properties of clouds, aerosols, and water vapor. Multifilter radiometers were mounted facing the surface at Met City and, with a shadowband, facing the sky on *Polarstern*. These measurements made at discrete spectral bands in the SW are suitable for deriving information on the spectral surface albedo. The Multifilter Rotating Shadowband Radiometer further distinguishes the diffuse scattered and direct beam SWD components, as do broadband SPN1 pyranometers deployed at Met City and on the *Polarstern* P-deck.

To characterize spatial heterogeneity more comprehensively, airborne observations were made using the HELiX multi-copter, Spectra quadcopter, and helicopter-borne HELiPOD. HELiX was operated within the CO, focusing on albedo measurements using pyranometers and a multispectral camera during Leg 4. Spectra was operated in the CO during Leg 5, equipped with pyranometers and spectro-radiometers to measure broadband and spectral albedo. HELiPOD was used to conduct radiation surveys extending well beyond the CO during Legs 3 and 4. At

Balloon Town during Leg 4, vertical profiles of radiative fluxes (all components) were sampled episodically using the BELUGA tethered balloon, providing information on the radiative flux divergence and derived atmospheric heating rates up to 1.5 km.

Turbulent sensible and latent heat fluxes (H_s, H_l) were calculated on a variety of platforms at multiple heights using the EC methodology. Each installation included an ultrasonic anemometer measuring three-dimensional winds and acoustic temperature (for H_s), usually paired with a co-located fast-response gas-analyzer to measure water vapor concentration (for H_l). In addition to the heat fluxes, observations were made of the momentum flux and its dependent stress variables (e.g., friction velocity, surface roughness length), which quantify the stress imparted upon the ice and ocean by the wind. All EC sensors were operated with sampling rates of 10–20 Hz, but the precise sampling frequencies, integration periods, and processing methodologies differed slightly between individual observing systems. These EC data provide direct measurements of turbulent momentum and heat fluxes, but are sensitive to assumptions about the stationarity of input data, reducing the number of valid samples. Therefore, the EC data are complemented by independent flux estimates using a bulk aerodynamic method based on standard meteorological measurements (wind speed, humidity, air and surface skin temperatures), which is sensitive to a different set of assumptions, principally the surface roughness (Andreas et al., 2010).

H_s was derived continuously at Met City from EC measurements at (nominal) heights of 2, 6, and 10 m, and for Legs 1–3 also at 23 or 30 m. H_l was derived at 2- or 6-m height depending on time of year. The multiple heights facilitate observing the turbulent flux and its divergence within and above the surface layer. The three ASFS systems, deployed at multiple locations across the CO and DN, were outfitted with EC capabilities at 3.8-m height. Two additional mobile eddy covariance systems made EC measurements at 3-m height and were designed to observe targeted areas for shorter periods of time (e.g., open leads, ridges, and specific footprint areas). All on-ice EC measurements were generally made at least 200 m from *Polarstern* to reduce the effects of the vessel on turbulence. EC measurements were also made while *Polarstern* was stationary from the bow tower (approximately 18 m), where corrections for flow distortion are more easily tractable. Airborne EC observations were carried out by HELiPOD on Legs 3 and 4. Measurements suitable for deriving parameters related to momentum fluxes (e.g., roughness length) were also made periodically from BELUGA on Leg 4.

Conductive heat flux (C) at the sea ice surface was measured using two flux plates paired with each ASFS and at the Met City tower. They are advantageous because they measure C directly such that assumptions about the transfer coefficients are not necessary, but are disadvantaged by the fact that they are localized within the profile and their depth varies with snow accumulation and ablation of snow and ice. The flux plate measurements are complementary to thermistor strings deployed throughout the CO and DN by the ICE team from which conductive heat flux can also be derived. Together these data form an important interfacial link for characterizing both sides of the atmosphere-ice interface.

2.6 Aircraft observations

The airborne campaign Atmospheric airborne observations in the Central Arctic (ACA) and the IceBird campaign using the research aircraft *Polar 5* and *Polar 6* (Wesche et al., 2016)

complemented the other measurements obtained during MOSAiC. These airborne activities contributed in-situ and remote sensing surveys covering a wide geographic area with different surface conditions. The primary objectives were to examine the spatial variability of the atmospheric boundary layer and surface, the influence of clouds on precipitation and radiation, and air mass transformation along trajectories, all ideally linked with the surface-based measurements during MOSAiC. Originally, four airborne campaigns were planned – two in spring and two in summer. However, due to the COVID-19 pandemic, the spring campaigns were cancelled. The summer campaigns took place from August 30 to September 17, 2020, based in Longyearbyen, Svalbard. Both aircraft are of the type Basler BT-67, with an operational range greater than 2500 km, which was sufficient to reach the sea ice during the summer campaigns, but not *Polarstern* at the time. Here the atmospheric component of the measurements made during the summer is outlined.

Polar 5, as the primary aircraft for ACA, was equipped with in-situ, remote sensing, and basis instrumentation (Table B7 in Appendix B). The observations focused on characterizing the Arctic ABL in conjunction with ocean-atmosphere interactions, clouds, solar and terrestrial radiation, and aerosol radiative properties. The mean three-dimensional wind vector and turbulent fluxes of momentum were derived from high frequency measurements of a five-hole probe mounted at the nose boom of *Polar 5*. A fast temperature sensor was installed to obtain fluxes of sensible heat. Sixty dropsondes were released during the flights to study the vertical profile of the atmospheric state. In-situ measurements of microphysical cloud properties were obtained by the Two-Dimensional Stereo cloud probe, the Cloud Combination Probe, the polar nephelometer, and the Precipitation Imaging Probe. This combination of cloud probes covered the size range of Arctic cloud hydrometeors from 2 μm to 6.2 mm and measured the particle shape, number concentration, and size distribution. The phase function of hydrometeors was detected with the polar nephelometer. In addition to the wing-mounted instruments, a Nevzorov bulk probe installed at the front part of the fuselage measured liquid and total water content of clouds. The cloud and surface remote sensing instrumentation of *Polar 5* combined the active, cloud radar, part of the Microwave Radar/radiometer for Arctic Clouds, a Humidity And Temperature PROfiler, the Airborne Mobile Aerosol Lidar system, the Spectral Modular Airborne Radiation measurement sysTem, the Airborne Imaging Spectrometer for Applications Eagle/Hawk, and a digital 180° fish-eye camera. A nadir-looking thermal infrared radiation thermometer and two pairs of upward and downward facing broadband radiometers were installed, including a pair of pyranometers for measuring solar irradiance (0.3–3.6 μm) and a pair of pyrgeometers for measuring terrestrial irradiance (4.5–42 μm). In addition to sea ice focused measurements, *Polar 6* was also equipped with the same suite of broadband radiometers. Details of the *Polar 5* instrumentation are summarized in Ehrlich et al. (2019). A total of 8 flights (43 flight hours) was conducted with *Polar 5* (see Figure 9 and Table 2) while *Polar 6* performed seven flights (Nicolaus et al., 2022).

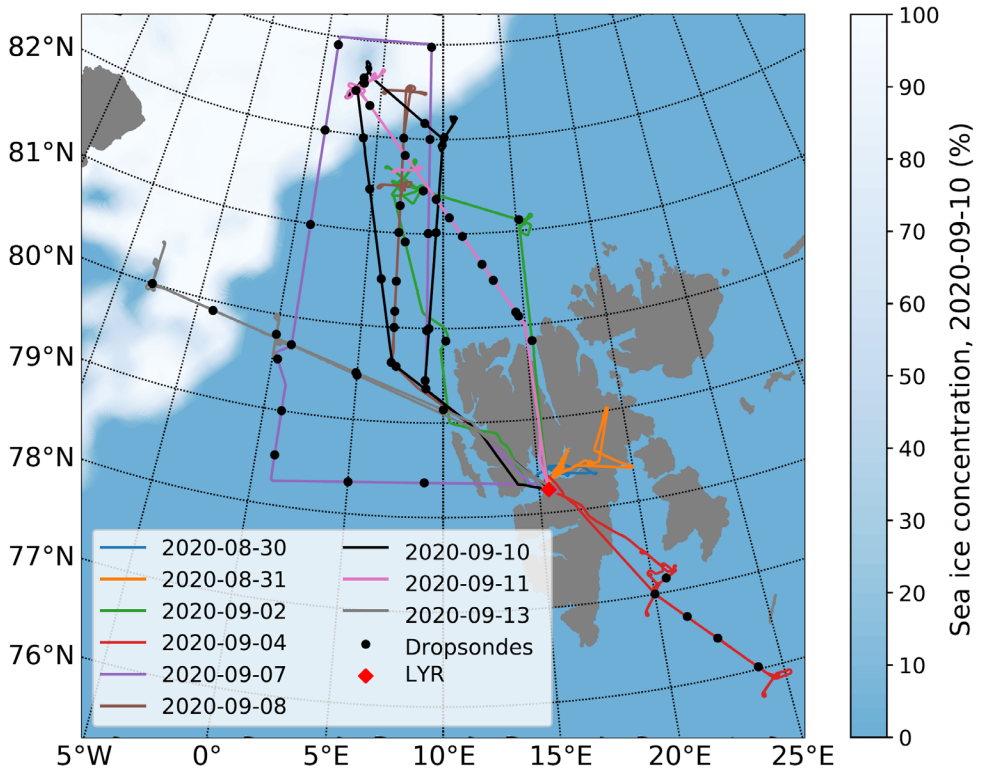

Figure 9. *Polar 5* flight paths for flights conducted during the ACA program out of Longyearbyen (LYR).
Flight dates are given as year-month-day. The sea ice concentration is shaded according to the colorbar.

Table 2. Flight activities wherein *Polar 5* was equipped for the ACA program

Date in 2020	Objective	Air time (hours)
Aug 31	Wing-by-wing flight with *Polar 6*	2.3
Sep 2	CALIPSO satellite underflight	5.5
Sep 4	ABL structure and fluxes	5.5
Sep 7	Remote sensing measurements of clouds	5.7
Sep 8	ABL structure and fluxes	6.1
Sep 10	Cloud properties over sea ice and open water	6.2
Sep 11	Cloud properties over sea ice and open water	5.7
Sep 13	ABL structure and fluxes	5.8
All dates	Inclusive	42.8

2.7 Field operations and support

Field operations for the ATMOS team focused on two modes of operation. Most observations were designed to be as continuous as possible for the full year. Day-to-day field support for these observations followed a routine schedule of checks and maintenance. The second mode of operation was for targeted observations with specialized, non-continuous instrumentation,

including the tethered balloons, HELiPOD, UAS, crewed aircraft, and various direct sampling activities. While only implemented periodically, these activities often required intensive support. Standard operations faced a few key challenges over the course of the year. For on-ice activities, frequent events of ice dynamics sometimes limited access to measurement or sampling sites, forced instrument re-installations, and interrupted the line power provided from the ship to on-ice installations. Continuity was also affected when *Polarstern* had to transit to the ice edge for resupply and crew rotation or to move the ice camp. Fortunately, most of the onboard instrumentation remained operational during these transit periods, offering a unique spatial perspective of many key parameters. Additionally, during the month-long absence of *Polarstern* from the MOSAiC ice floe from mid-May to mid-June, an ASFS was left behind to monitor the near surface meteorology and surface energy budget continuously.

During the course of the year additional targeted experiments and/or special operations were implemented, sometimes in coordination with other teams. These included increased radiosonde profiling frequency to capture key events like a mid-April warm air intrusion. Enhanced observations were also made during a continuous 36-hour period as well as a specialized "flight day" in mid-summer, both of which included intensive observations from tethered balloons and UAS to examine diurnal variability. Additionally, specialized surface flux experiments were performed with multiple measurement systems to examine, for example, the impact of surface roughness features on turbulent exchange. Lastly, the ATMOS team participated in a coordinated, cross-team sampling of upper ocean freshwater layers, with a specific focus on gas transfer processes.

Complementing these field observation activities, modeling also played an important role in support of both field operations and data interpretation. First, operational forecasts from the Deutscher Wetterdienst, delivered each day, provided essential support for day-to-day operations and enabled the ATMOS team to prepare for key events, such as storms, that were of great interest. After the field operations, re-analysis data have offered an important context for the observations relative to the last decades (e.g., Rinke et al., 2021), while coupled models have provided experimental forecasts to serve as a basis for coupled-system analyses. Additionally, trajectory modeling using tools such as the Lagrangian particle dispersion model FLEXPART (Pisso et al., 2019) have given significant insight into the source regions for sampled air masses and interpretation of gas and aerosol measurements.

3. Results

3.1 Annual cycle perspective

The comprehensive suite of atmospheric measurements made during MOSAiC was designed to operate over the full annual cycle, and to specifically observe many key processes in action throughout that annual cycle. As context for more detailed studies, an understanding of the basic atmospheric variability over the MOSAiC year is therefore essential. We explore this variability by examining continuous, daily-average time series of a set of core meteorological measurements during the entire MOSAiC drift.

The annual cycles of near-surface meteorology for the MOSAiC ice floes, including atmospheric pressure, temperature, and relative humidity at a nominal 2-m height as well as 10-m wind speed, are shown in Figure 10. All of these parameters were measured nearly continuously from the meteorological tower installed at Met City. For periods without continuous measurements at Met City, such as from mid-May to mid-June when *Polarstern* left the ice floe, equivalent measurements from an ASFS were included to complete the time series. The spatial location of these measurements over time is given in Figure 2.

Annual variability is most apparent in near-surface temperature, which also provides insight into seasonal transitions. As the drift started, air temperature around –10˚C indicated that the autumn freeze up was already underway. As autumn transitioned to winter, the temperature continued to drop until a minimum near –40˚C during the first four days of March 2020. The temperature remained generally colder than –20˚C, broadly defining the winter season, from the end of November 2019 through mid-April 2020. In mid-April, a transition to air temperature warmer than –20˚C occurred abruptly, coincident with a southerly advection event, signifying the spring transition season and the progression towards melt. In late May, as the sea ice reached consistent surface melt, the near-surface temperature was constrained by the melting ice to a narrow range within a couple degrees of 0˚C, where it remained until early September. In the first days of September, near-surface temperature dropped significantly and consistently below 0˚C, pushing the system back towards the autumn freeze up, with similar conditions to when the expedition began a year prior. The annual cycle of near-surface relative humidity (with respect to liquid water) largely followed that of temperature, ranging from a winter minimum near 70% to summer maxima greater than 95%. When the relative humidity is considered with respect to ice, the near-surface layer was very close to ice saturation for the full year, except for the spring into early summer when values dropped consistently below 100%.

Surface pressure and wind speed tell a story of periodic storms that impacted many atmospheric processes, contributed to sea ice dynamics, and affected other components of the coupled system. Many of these events will be the focus of intensive future research. Over the year, 21 distinct cyclones (black squares in Figure 10a) were identified as having impacted the MOSAiC drift location, these being simply defined as periods when the surface pressure dropped below 1000 hPa locally associated with a distinct nearby low-pressure center. More detailed analysis of these cyclones is available in Rinke et al. (2021). Typically, these cyclones were linked with the advection of warm, moist air masses from lower latitudes towards the MOSAiC location, in addition to increased wind speed. Cyclones were markedly more frequent in winter, when large swings in pressure were observed, and infrequent in summer, with little pressure variation and consistently weak wind. Maximum observed daily-averaged near-surface wind speed reached 10–14 m s^{-1}, typically, but not always, coincident with passing cyclones.

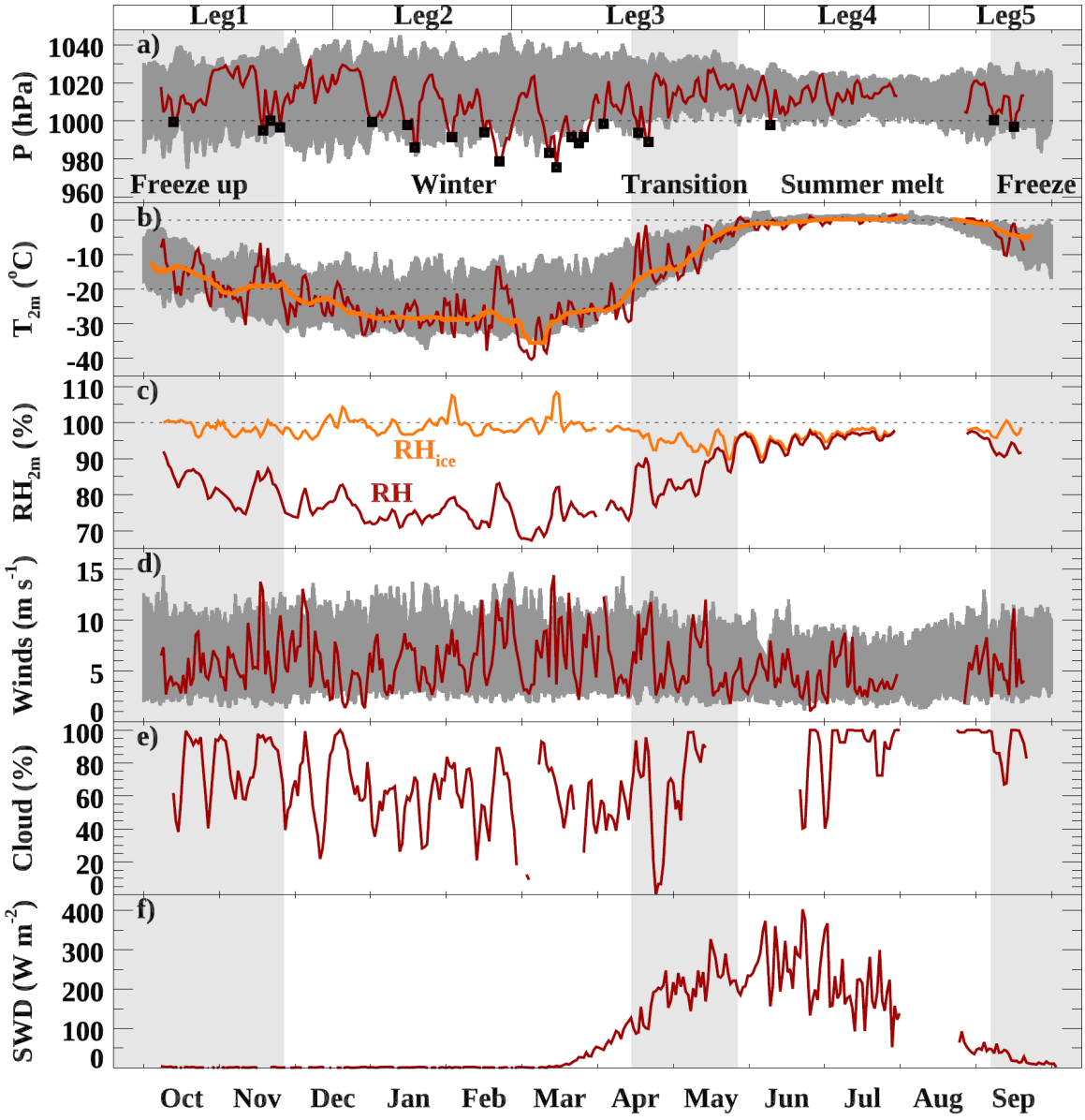

Figure 10. Surface-based atmospheric observations during the MOSAiC year. Daily-averaged (a) atmospheric sea-level pressure, with individual cyclone events identified (black squares); (b) 2-m temperature (red) and a 7-day running mean 2-m temperature (orange); (c) 2-m relative humidity with respect to liquid water (red) and ice water (orange) and (d) 10-m wind speed all measured from the met tower at Met City; (e) daily cloud occurrence fraction from a ceilometer onboard *Polarstern* (with gaps when *Polarstern* left the MOSAiC ice floes); and (f) downward shortwave radiation measured at Met City. While Met City was not operational during mid-May to mid-June, most measurements were provided by an Atmospheric Surface Flux Station that remained at the MOSAiC ice floe. The 5th–95th percentile range of ERA5 results at the moving MOSAiC position is given (gray shading) in (a), (b), and (d) based on Rinke et al. (2021). The MOSAiC Leg periods are shown along the top, and a general characterization of seasons, as described in the text, is provided with alternating gray and white background shading.

The lowest pressure center at the CO occurred on March 14, associated with the expedition minimum instantaneous sea-level pressure of 973.6 hPa and expedition maximum daily-averaged near-surface wind speed greater than 14 m s^{-1}, although relatively little change in temperature was observed at this time. A number of additional storms are of interest. A mid-November series of storms brought a period of warm air with strong wind, leading to the first significant sea ice deformation event that impacted the CO. A late February storm produced persistent strong wind and a mid-winter warming to –10˚C. In mid-April, a significant warm air intrusion event with strong wind initiated a seasonal transition towards the melt onset, moving the system from a period with temperature consistently below –25˚C to one with temperature consistently above –15˚C. This transition was coincident with a major transition in the large-scale circulation pattern impacting the region, and a diminished dominance of northerly winds. A mid-May storm was also quite significant, in spite of the surface sea-level pressure remained well above 1000 hPa, featuring the highest instantaneous near-surface wind measurement of > 17 m s^{-1} and resulting in substantial movement of the sea ice along a shear zone through the CO. A final influential storm occurred in mid-September as the surface had begun to freeze, bringing warm air, high winds, and rain on snow, which temporarily interrupted the freeze up.

Relatively quiescent atmospheric periods also played important roles during MOSAiC. A prolonged high-pressure period in late December, with nearly a week of atmospheric pressure near 1030 hPa, had weak wind and pushed the near-surface temperature down towards –30˚C for the first time. A similar cold, calm episode in early March directly followed the late February storm. In the week-long transition between these events, the sky generally cleared and the temperature plummeted by more than 25˚C, leading to the only period with the temperature consistently near –40˚C and an expedition minimum-observed instantaneous 2-m temperature of –42.3˚C on March 4. Moving towards summer, sea-level pressure was generally high. Persistent weak wind through most of July likely played a role in enabling the buildup of fresh melt water in the upper ocean (Rabe et al., 2022).

Air mass back-trajectory analysis provides important context for the meteorological and composition measurements. In this case the FLEXPART model was driven with hourly data from the European Centre for Medium-range Weather Forecasts fifth generation reanalysis (ERA5), and every 3 hours 100,000 atmospheric particles were initialized at the *Polarstern* location and traced backward for 30 days. The output of this back-trajectory mode represents the residence time of air masses over the geographic grid during their transport. Of special interest here is the residence time of particles below the lowest model layer at 100 m, which represents the interactions of the air masses with possible sources near the surface, where most gas and particle emissions occur. This quantity, divided by the thickness of the considered layer, is called footprint emission sensitivity (FES), because, if multiplied by emission fluxes of a specific constituent (e.g., from an inventory) and integrated over the domain, it would give the corresponding atmospheric concentration of that constituent at the ship location (Stohl et al., 2003). An FES time series for a passive air tracer (not subject to removal or decay) integrated over five distinct regional domains (Figure 11) clearly shows that interactions with the ocean and sea ice surfaces were dominant for the atmospheric composition observed at *Polarstern* year-round. Ice-covered surfaces were most influential in winter and early spring, when the sea ice extent was at its maximum. During late spring, while sea ice still covered a large part of the Arctic Ocean, a considerable fraction of the air mass back-trajectories were transported across

ice-free ocean regions. The relative contribution of ice-free ocean influences increased as the sea ice spatial extent decreased, with the largest ocean influence in late summer and autumn. Trajectories interacting with the near-surface over land masses during the prior 30 days were relatively rare, with the significant interactions occurring over northern Asia mostly during winter and early spring, with some influences in autumn. These findings are typical for the Arctic and explain the relatively lower concentrations of anthropogenic pollutants in summer than in winter (Stohl, 2006). The overall decline of FES in the spring-to-summer period indicates less interaction of air masses with the near-surface environment at this time of year, and is consistent with the higher observed atmospheric pressure (Figure 10a) and associated subsidence.

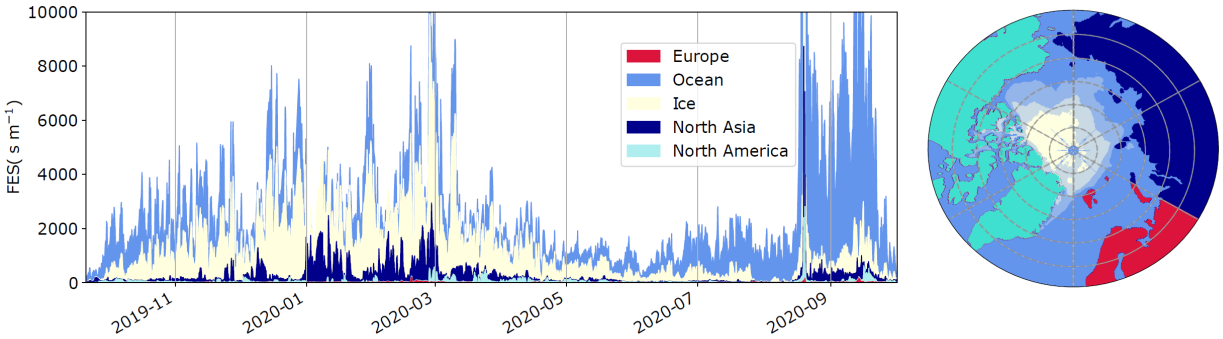

Figure 11. Trajectory analysis providing information on air mass origins. A time series of FLEXPART model footprint emission sensitivity for 30-day back-trajectories of a passive air tracer and integrated over the different regions shown in the map on the right. The different degrees of blue-to-white shading over the Arctic Ocean indicate the yearly evolution of sea ice cover (30, 50, and 99% sea ice concentration). The thickness of each colored layer in the time series represents the contribution of the corresponding region to the total FES. The quantity in the time series is expressed in units of s m^{-1} such that, when multiplied by the emission flux of a species over a region (given in units of kg m^{-2} s^{-1}), it gives an estimate of the relative contribution of each region to the total concentration (in kg m^{-3}) observed at *Polarstern*.

The most notable aspect of the large-scale circulation during the MOSAiC year was the particularly strong polar vortex that occurred from January to early April (e.g., Dethloff et al., 2021). During this period, the tropospheric circulation was generally locked into a quasi-static pattern with evidence for strong stratosphere-troposphere linkages and some of the strongest seasonally averaged stratospheric winds ever recorded (Lawrence et al., 2020). The Arctic Oscillation index during January to March was at record positive levels, with almost 60 days during this period with an index greater than 1 (Lawrence et al., 2020). These circulation patterns contributed to substantial warmth in the Siberian Arctic and increased precipitation in Northern Europe (Lawrence et al., 2020), the largest ozone hole ever observed in the Arctic (e.g., Wohltmann et al., 2020), and a particularly direct and rapid drift of the MOSAiC ice station across the central Arctic during these months (Krumpen et al., 2021). Additionally, as observed in the back-trajectory analysis, this circulation pattern likely contributed to an increased influence of the Siberian land surface on the atmospheric composition observed at the *Polarstern*.

MOSAiC is fundamentally limited by only observing one year. When placing the near-surface meteorological conditions during MOSAiC in the context of previous years based on the ERA5 reanalysis, Rinke et al. (2021) arrived at the following main conclusions. First, the entire MOSAiC year clearly fell primarily within the interquartile range of conditions from the preceding four decades (Figure 10). However, the MOSAiC winter and spring were characterized by relatively more frequent and stronger storm events than a typical year. Surface pressure was considerably lower than climatology in February and March, associated with the positive Arctic Oscillation index at the time. The temperature, moisture and radiation conditions associated with the storms and moisture intrusions in November, February and April also emerge as atypical by being outside of the interquartile range of the reanalysis data, and in some cases were record-breaking for their given times of the year. Winter minimum temperatures were also somewhat warmer than in the climatology. Additionally, the MOSAiC summer was anomalously warm and wet. These anomalous conditions started in May but really took hold in July and August, resulting in the highest ever monthly mean values of near-surface temperature and column-integrated water vapor. The surface temperature was near the melting point for approximately a month longer than the climatological median melt season length. To some degree these emergent behaviors are to be expected, as the location of the MOSAiC drift in summer was then much closer to the ice edge than it was during much of the climatological record.

3.2 Comprehensive atmospheric observations

To demonstrate the breadth of the MOSAiC atmospheric observational suite and its utility for studying numerous processes that are central to the MOSAiC science objectives, we examine two case studies in some detail. These include one case from winter, February 5–7, 2020, and another from summer, July 13–15, 2020. Both cases comprise a subset of characteristic measurements, although not all measurements are included due to their sheer number, nor do the cases represent particularly significant events. Rather, these cases were chosen to highlight a variety of conditions that occurred throughout the year and to demonstrate how the different observations complement each other towards telling a comprehensive and compelling story. More in-depth analyses targeting these case studies and others of high interest, such as the mid-November and mid-April storms highlighted in Section 3.1, will be the subject of forthcoming dedicated publications.

Winter case of February 5–7, 2020

In early February, a broad high sea-level pressure system sat over the coastline of eastern Siberia, reaching out over the Arctic Ocean (Figure 12). A band of low pressure stretched from Greenland, across Fram Strait towards Novaya Zemlya, with a low-pressure center over the western Siberian coastline. Accordingly, a low-level, relatively warm air mass impinged on *Polarstern* from central Siberia, and the MOSAiC measurements nicely characterize the changes brought by this air mass. Radiosoundings showed an initial pulse of relatively warm air aloft while the surface remained cold, leading to a 10˚C near-surface temperature inversion and otherwise typical, statically stable wintertime conditions (Figure 13). Lidar-based RH retrievals confirm this to be a relatively dry inversion, with near-water saturated air being trapped near the surface. Over the following days, as the near-surface wind speed remained modest or even decreased in time, wind speed aloft increased significantly. An air mass shift at about 14:00 (all

times are in UTC) on February 5 brought a deep layer of moisture and an erosion of the near-surface stratification. This transition included a short period of cooling at low levels, a warming and descent of the tropopause, and rapid shifts in upper-tropospheric winds (not shown), all consistent with the passage of a weak tropopause polar vortex (Cavallo and Hakim, 2010). Both RH profiles and the vertically integrated water vapor confirm this moist air mass to persist for approximately 2 days. Thereafter, altitudes above 1 km dried significantly and the near-surface stratification was again established. The change in the air masses reaching *Polarstern* during this period is also clearly visible in the isotopic composition of the near-surface water vapor. Both a first small increase in deuterium excess (d-excess) during February 5 and a second stronger increase early on February 6 (Figure 13g) indicate the arrival of water vapor that has been transported to *Polarstern* over a long distance without further mixing with different air masses.

Cloud sensors (Figure 14) revealed low-level fog for the first 8 hours of this case, embedded in the moist air below the strong temperature inversion, with LWPs of 5–25 g m^{-2}. With the air mass shift, the deep layer of atmospheric moisture and some mid-level destabilization supported multiple types of clouds, reaching at times from the surface up to nearly 9 km altitude. These deeper clouds were initially composed primarily of ice and snow, as confirmed by lidar depolarization ratios larger than 0.1, large fall velocities (not shown) and no discernible LWP (Figure 14d). However, over time there were embedded layers of supercooled liquid water at temperatures of –20 to –26˚C, from which ice crystals fell; these were classic Arctic mixed-phase clouds. The presence of these liquid layers is supported by high lidar backscatter, low lidar depolarization ratio, and positive LWP values derived from microwave radiometers. As ice crystals fell from these clouds, both snow particle counters (Figure 14e) and ice particle imagers (Figure 14f) deployed near the surface registered particles, with the strongest precipitation occurring on February 6.

Gas and aerosol measurements showed some variability similar to the atmospheric structure and clouds (Figure 15), likely driven by spatial heterogeneity of sources. The trace gases suggested a change of air mass on February 5, similar in timing to the other atmospheric measurements, when CO_2 and CH_4 concentrations rose while ozone decreased. SO_2 concentrations were initially high leading into February 5, likely related to rapid transport from specific pollution sources in Siberia. Over time as the surface pressure pattern shifted eastward along the Siberian coast and the low-pressure center weakened (not shown), SO_2 declined significantly. Later increases in CO_2, CH_4, and SO_2 during the middle of February 7 suggest a further shift in the air mass source region. Aerosol precursor gases (Figure 15c) did not show significant variability, except for sulfuric acid at the beginning of the period, suggesting that these precursor gases were not as strongly impacted by air mass origin and may have been limited by slow photochemistry during polar night and a lack of local biological emissions at this time.

Aerosol populations also underwent interesting transitions. During the early period of fog, both the particle size distributions and the total particle counts (Figure 15 d, e, g) showed a local minimum, coincident with the maximum in LWP, likely because many of the near-surface particles were activated into fog droplets. Initially, the CCN concentration comprised approximately 90% of the total particle concentration, consistent with size distributions showing predominantly larger particles (i.e., those most likely to be CCN). The predominance of accumulation mode particles around 200 nm is characteristic of the prevalent Arctic haze

situation (Freud et al., 2017). As the moist air mass entered the domain, total particle number increased. At the same time, the fractional amount of CCN became relatively lower as the number of particles smaller than 100 nm increased. Daily INP concentration during these early periods was about 0.005 L^{-1}, with the largest contribution from 1.21–2.96 μm particles (Figure 15g). Similar to the shift in gases, there was a marked transition during the middle of February 7 with substantial increases in aerosols at all size ranges and a commensurate increase in CCN. The total INP concentration increased by a factor of 7 with the majority of that increase occurring for the largest particles (2.96–12 μm). Total aerosol scattering tells a consistent story, with much smaller values early in the case but a transition to very large values with this final transition. Additionally, lidar observations in cloud-free regions (Figure 14b) reveal a general increase in backscatter below 2 km starting with the frontal passage on February 5.

With no sunlight in February, long-wave radiation was the primary driver of variability in the surface energy budget (Figure 16). Upward emission from the surface simply followed the variability of surface temperature, while the surface temperature was modulated by the balance of other terms. Downward radiation mostly from liquid-containing clouds provided the largest perturbations, with increases of 50 W m^{-2} that drastically decreased the surface radiative deficit during cloudy periods relative to those without clouds. This behavior represents the typical cloud-driven, bi-modal state of the Arctic system (e.g., Shupe and Intrieri, 2004). Infrared spectral brightness temperatures (Figure 16b) provide insight into these radiative effects, revealing numerous bands that are continuously opaque (i.e., CO_2 band at 667 cm^{-1}), while most of the variability occurs in the so-called atmospheric windows, which become transparent during clear skies but much warmer during cloudy skies. The surface cooled significantly during clear sky periods, leading to strong near-surface stratification and downward sensible heat flux (Figure 16c, d). However, in response to cloud radiative effects, the surface temperature warmed and near-surface temperature gradient diminished, leading to a smaller sensible heat flux that sometimes even acted to cool the surface. While behaving similarly, turbulent latent heat flux was very small. Because no ice is melting at this time, the atmospheric radiative and turbulent heat fluxes are balanced according to Equation 1 by the change in storage (i.e., temperature) in the finite, thin layer at the snow-air interface and the sub-surface conductive heat flux to the snow surface (black line in Figure 16d). Through most of this winter case, strong net atmospheric cooling was balanced by significant conductive warming of this top snow interface. However, during cloudy periods with decreased atmospheric cooling, and even short periods of surface warming, the upward conductive heat flux to the surface diminished and periodically changed sign. These periodic atmospheric warmings, in principle, serve to modulate the ice cooling and growth process.

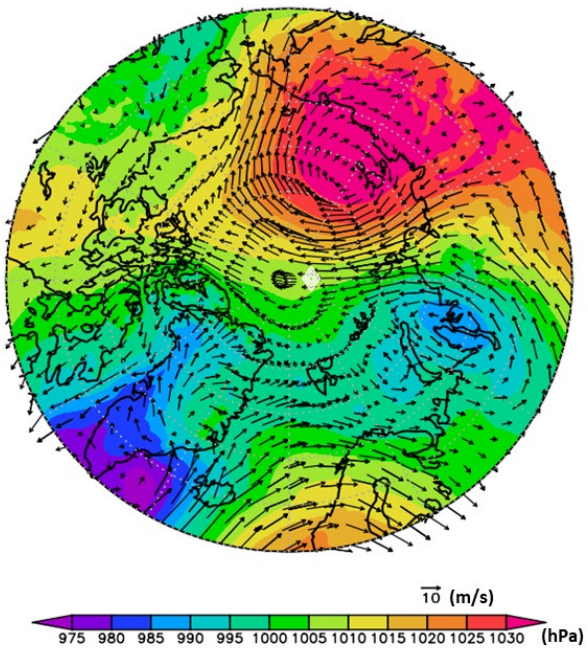

Figure 12. Sea-level pressure and 850 hPa wind vectors averaged over February 5–7. Data are derived from the ERA5 reanalysis. Sea-level pressure is given as colors in hPa. A 10 m s^{-1} wind vector is given in the legend, and plotted wind vectors scale linearly.

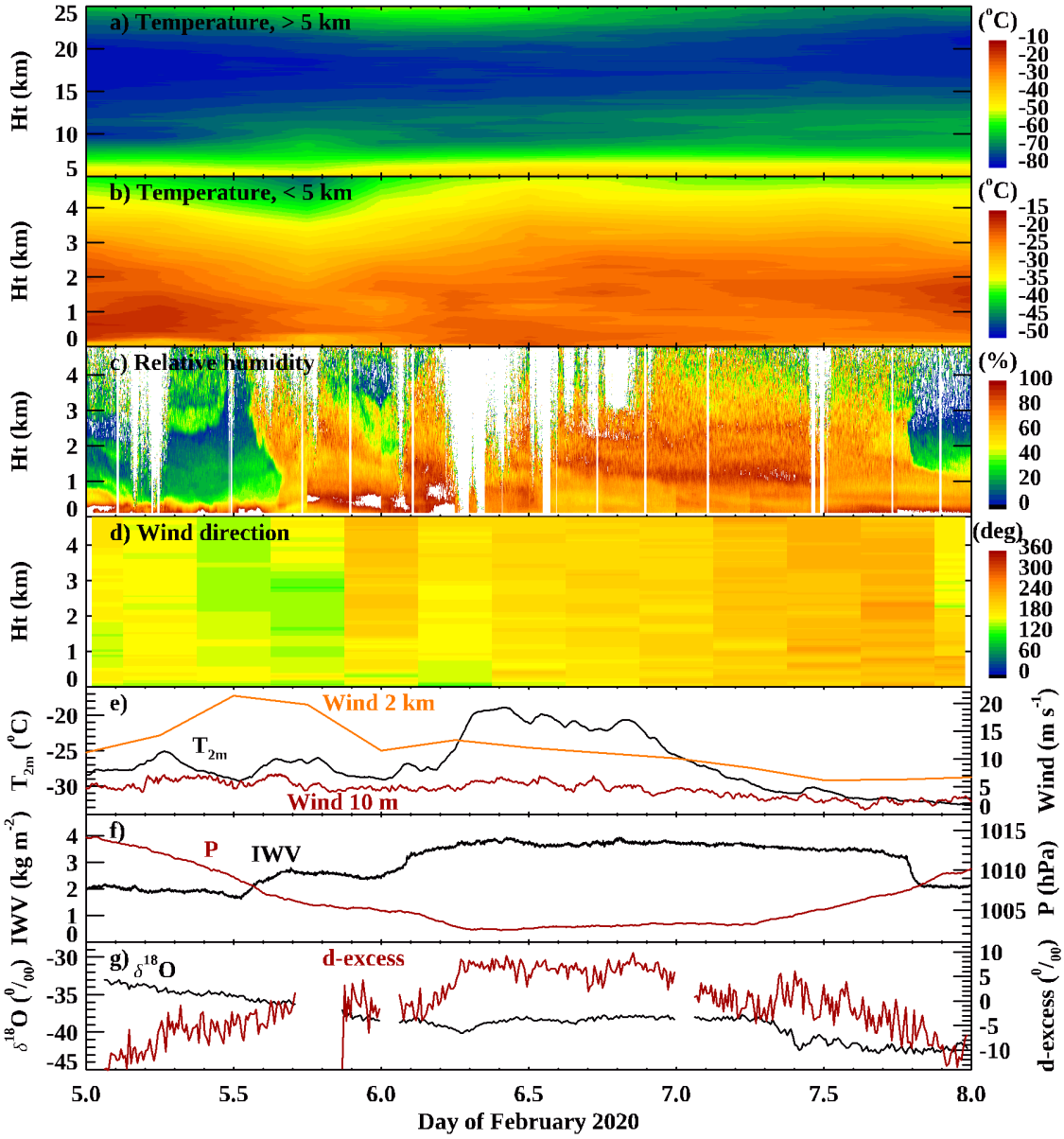

Figure 13. Atmospheric physical state measurements for the February 5–7 case. Temperature profiles from radiosondes for heights (a) above and (b) below 5 km; (c) relative humidity profiles derived from the PollyXT lidar; (d) wind direction profiles derived from radiosondes; (e) 2-m temperature (black) and 10-m wind speed (red) derived from the Met City tower, and 2-km wind speed from radiosondes (orange); (f) integrated water vapor (IWV, black) derived from the HATPRO and surface pressure (red) measured at the Met City tower; and (g) $\delta^{18}O$ (black) and d-excess (red) observed by a water vapor analyzer.

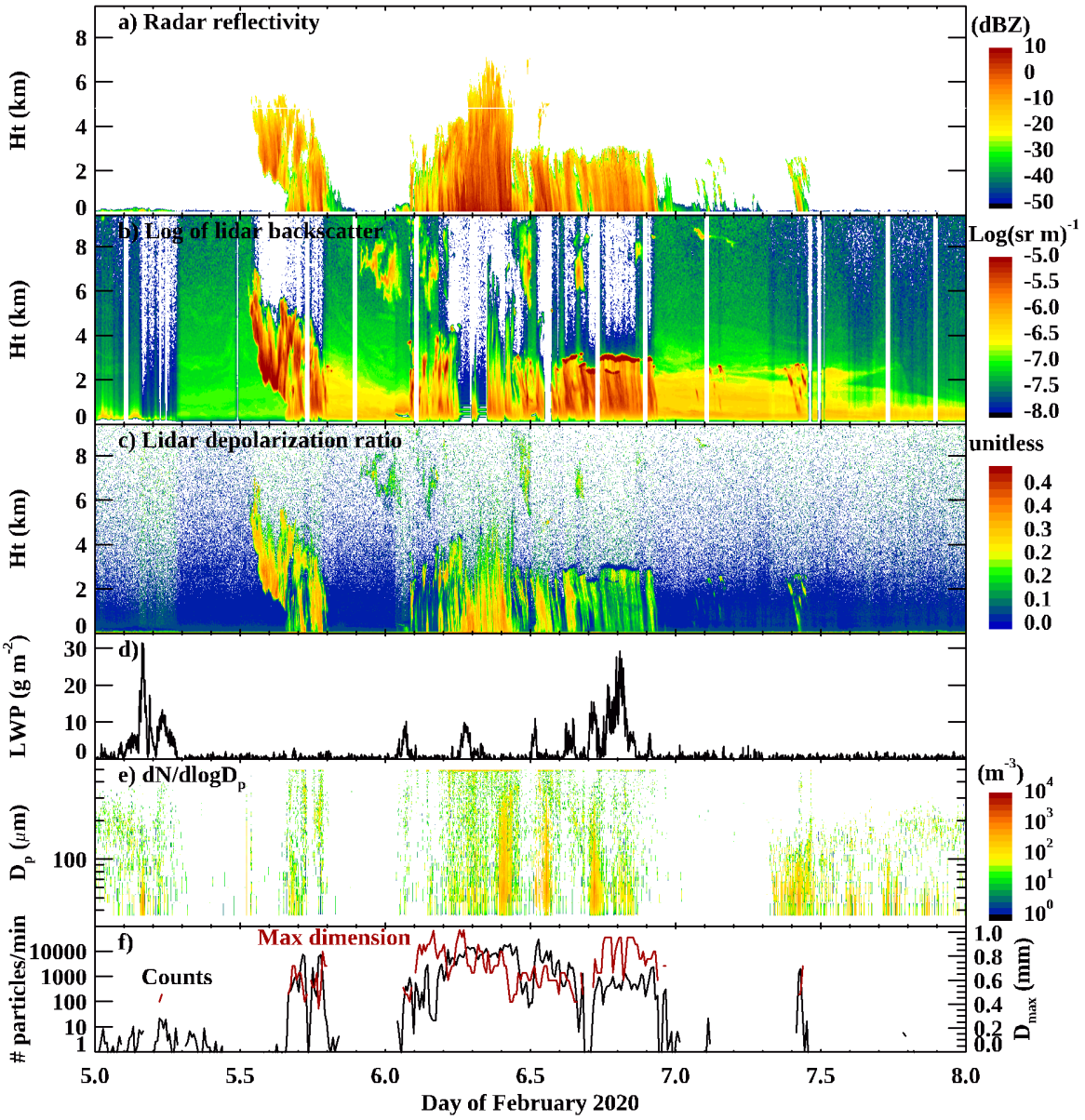

Figure 14. Cloud and precipitation measurements for the February 5–7 case. Time-height profiles of (a) radar reflectivity from the KAZR, (b) log of the lidar backscatter from PollyXT, (c) and lidar depolarization ratio from the Micropulse lidar; and time series of (d) liquid water path derived from HATPRO, (e) ice particle size distribution from a snow particle counter on the Met City tower, and (f) snow particle counts (black, left axis) and average particle maximum dimension (red, right axis) observed by the Video In Situ Snowfall Sensor at Met City.

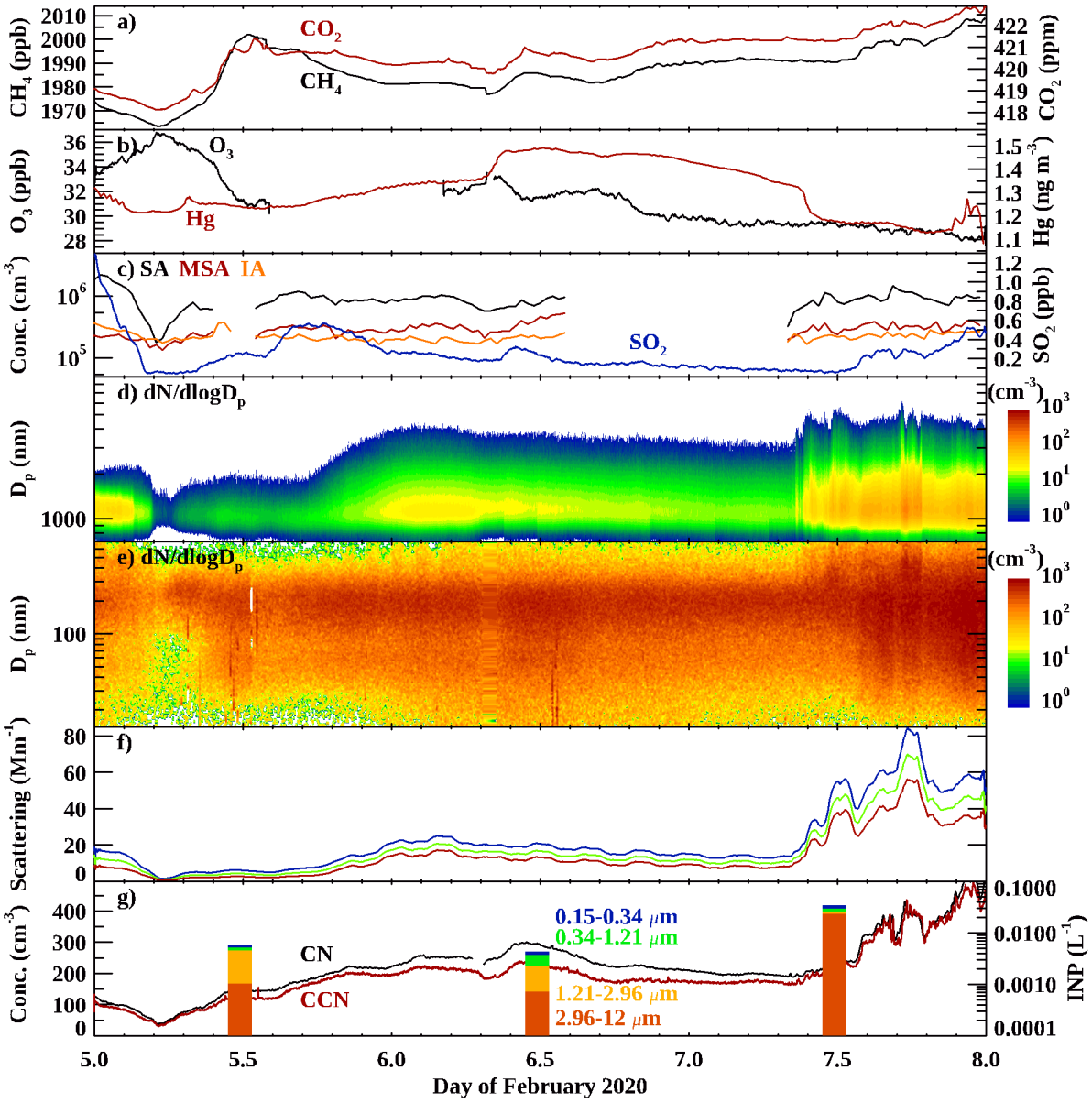

Figure 15. Gas and aerosol measurements for the February 5–7 case.
Gas concentrations of (a) CH_4 (black) and CO_2 (red), (b) O_3 (black) and Hg (red), and (c) sulfuric acid (SA, black), methanesulfonic acid (MSA, red), and iodic acid (IA, orange), all on the left axis, and SO_2 (blue) on the right axis. Aerosol number size distributions measured by (d) aerodynamic particle sizer and (e) scanning mobility particle sizer; (f) light scattering measured at 3 wavelengths (700 nm in red, 550 nm in green, and 450 nm in blue) from the nephelometer; and concentrations of (g) total particles (CN) from a condensation particle counter (black, left axis), total cloud condensation nuclei (CCN) at 0.4% supersaturation (red, left axis), and ice-nucleating particles (INP) in different size ranges (color bars, right axis).

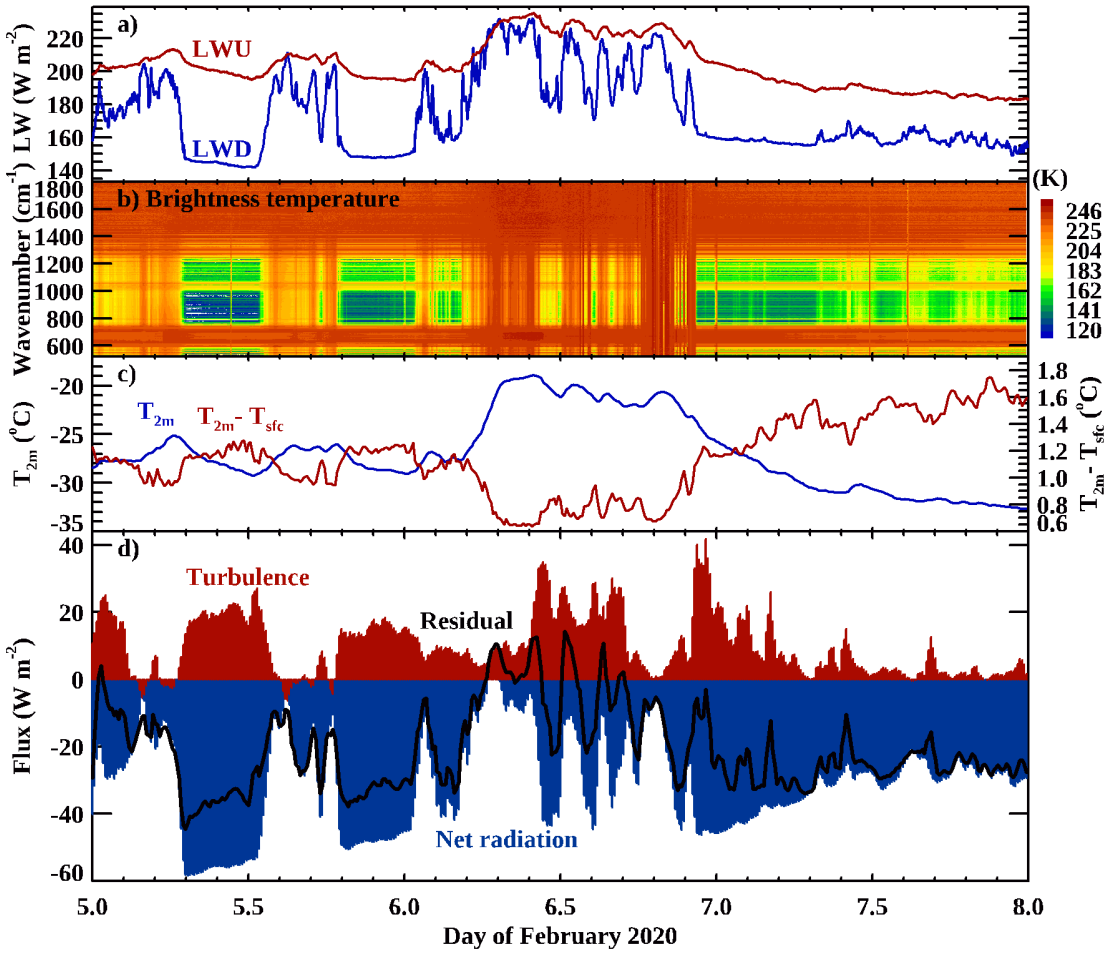

Figure 16. Energy balance measurements for the February 5–7 case. (a) Upward (red) and downward (blue) long-wave broadband radiation (LWU and LWD, respectively) measured at Met City; (b) infrared brightness temperature spectra observed by the Marine Atmospheric Emitted Radiance Interferometer; (c) 2-m temperature (blue) and the near-surface (T_{2m}–T_{sfc}) temperature gradient (red); and (d) turbulent sensible plus latent heat flux (red) and net radiative flux (blue) derived from Met City, along with the residual of these energy budget terms (black). According to Equation 1, because melting is zero at this time of year, this residual is comprised of the net change in temperature of the finite, thin surface layer and the sub-surface conductive heat flux.

Summer case of July 13-15, 2020

In the middle of July, as the drifting MOSAiC ice floe approached the ice edge in Fram Strait, the *Polarstern* was under a high sea-level pressure ridge spanning between a high-pressure center that filled much of the central Arctic and a second weaker high just south of *Polarstern* (Figure 17). A modest low-pressure cyclone was positioned over the northern tip of Novaya Zemlya. The *Polarstern* position relative to these systems meant generally weak wind, with a slow transition in time from low-level wind that was from the E-SE on July 13, shifting towards

W-SW on July 14 as the local pressure dropped, then transitioning towards NW by the end of July 15 (Figure 18).

At this time of year, the surface temperature is nominally constrained to approximately 0˚C by the melting surface (Figure 18f). Low-level temperature structure (Figure 18a) initially showed a weak near-surface temperature inversion with periodic low, thin liquid-containing clouds. During the second half of July 13 a second temperature inversion strengthened at 1–1.2 km associated with a liquid cloud that produced weak precipitation. Moving into July 14, the relatively warm southerly flow aloft was underridden by westerly low-level winds bringing cold flow from Greenland, leading to much stronger stratification at about 300 m. The cold flow over a warm surface also destabilized the near-surface stratification, supporting continued formation of low cloud and fog. Moving into July 15, the winds from 0.3–2 km altitude turned northerly bringing even warmer temperatures that slowly pushed downwards in time as the westerly flow at those levels subsided. Some higher-level clouds (mostly not seen in Figure 19a) formed in the moist air aloft (not shown).

Solar radiation (Figure 18d) followed expected daily cycles, modulated by the low-level, and liquid-containing, cloud coverage; at this time the melting ice surface had an albedo of about 0.59 leading to net surface shortwave radiation of 40–200 W m^{-2} depending on time of day. Upward emission from the surface was rather steady at 315 W m^{-2} due to the tightly constrained surface temperature (Figure 18e). When the liquid water clouds were present the downward long-wave radiation was similar to the surface emitted radiation; however, during brief cloud-free (or thin cloud) periods there was a significant deficit of long-wave radiation at the surface of up to 55 W m^{-2} (as was also observed in winter). This surface cooling led to periodic dips of the surface temperature below its expected melting value of 0˚C (Figure 18f). During July 13, the 2-m temperature was sometimes warmer than the surface, leading to minimal (sometimes downward) turbulent heat fluxes. However, with the transition towards cold, low-level, Greenlandic flow starting on July 14, the 2-m temperature became consistently colder than the surface, leading to strengthened upward surface turbulent heat fluxes, additionally contributing to surface cooling.

Aerosol processes reflect the complexity of this case (Figure 19). Initially the near-surface total particle concentration was quite low (20–80 cm^{-3}) with few CCN. During the second half of July 13, the number concentration increased significantly, with most of this increase occurring for particles smaller than 20 nm in size (Figure 19d) in an apparent new particle formation event possibly linked with local surface gas emissions. The low-atmosphere transition observed early on July 14 was also evident in the aerosol populations, wherein there was no longer suggestion of new particle formation but instead a large and increasing population of particles 20–50 nm in size. From this time forward there were few particles larger than 300 nm. However, throughout the full period starting on mid-day July 13 a Hoppel minimum between the accumulation and Aitken modes was visible, consistent with cloud processing of the aerosol population (Hoppel et al., 1994). During this case, daily INP concentration started out very low (< 0.001 L^{-1}) compared to the winter case, with the largest contributions from smaller-sized particles (0.15–1.21 μm). However, by July 15 the INP concentration increased by nearly an order of magnitude (> 0.004 L^{-1}), with the largest contribution from the size range of 1.2–2.96 μm. These results are in

contrast to the winter case when the largest particles (2.96–12 μm) were the largest contributor to the overall INP concentration.

Profiles on July 15 from tethered balloons, UAS, and radiosondes help to better constrain the vertical aspect of some parameters (Figure 20). The potential temperature and RH profiles mid-day on July 15 show a moist, well-mixed cloudy boundary layer up to about 220 m. As the day progressed, the Distributed Temperature Sensing system on Miss Piggy showed changes in potential temperature and a descending boundary layer height. Turbulent kinetic energy at mid-day was elevated in and below the observed cloud level, consistent with long-wave cloud-radiative cooling (Figure 20f) driving mixing of the boundary layer. Note that the heating rate profile was complicated at this time by upper level clouds. Wind speed (Figure 20c) was quite weak through the boundary layer, with a low-level jet observed by BELUGA about 100 m above the boundary layer top associated with the strong temperature inversion. The concentration of aerosol particles larger than 10 nm (Figure 20e) also appeared to be relatively constant across the well-mixed boundary layer (approximately 200 cm^{-3}), with a marked increase to > 1000 cm^{-3} above, suggesting a significant source of aerosols from aloft at this time. For particles larger than 150 nm, which typically can serve as CCN (e.g., Schmale et al., 2018), there was a nearly constant concentration of about 15 cm^{-3} from the surface up to 500 m, except for within and directly adjacent to the cloud layer itself. This vertical structure is consistent with cloud droplet formation on the aerosols, which are not sampled, and some entrainment at the top and bottom boundaries of the cloud. In most cases the measurements nearest the surface are consistent with equivalent, independent near-surface measurements.

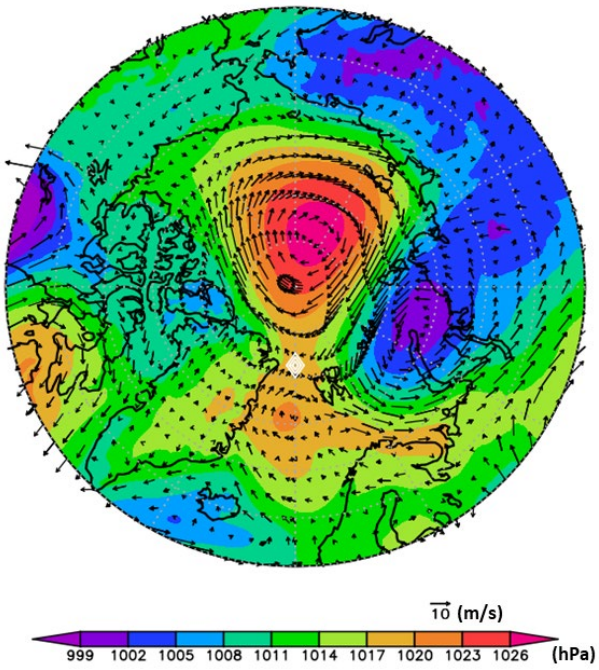

Figure 17. Sea-level pressure and 850 hPa wind vectors averaged over July 13–15. Data are derived from the ERA5 reanalysis. Sea-level pressure is given as colors in hPa. A 10 m s^{-1} wind vector is given in the legend and plotted wind vectors scale linearly.

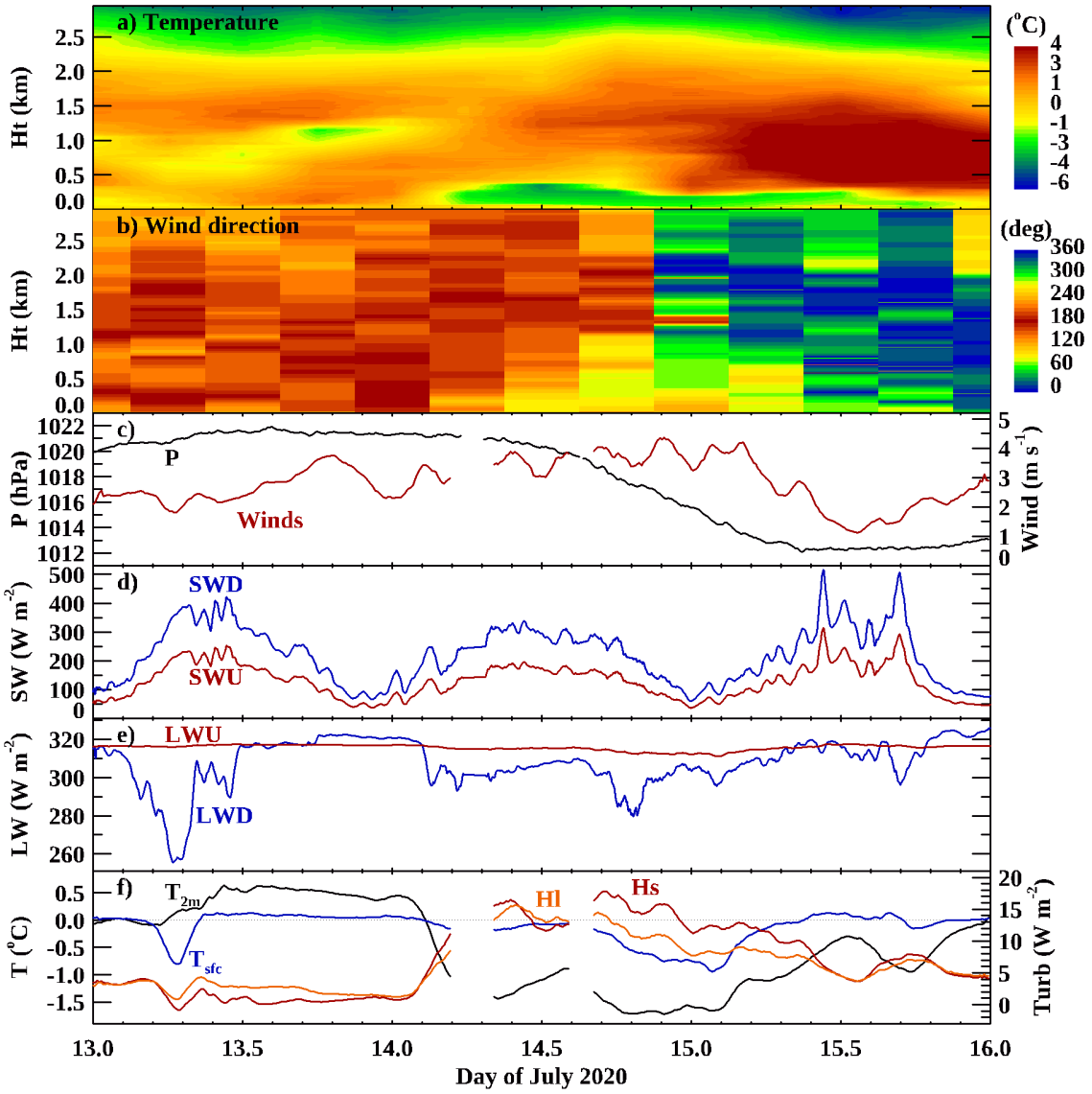

Figure 18. Meteorological and surface energy balance measurements for the July 13–15 case.

(a) Temperature and (b) wind direction profiles from radiosondes for heights below 3 km; (c) surface pressure (black) and 10-m wind speed (red) from the Met City tower; downward and upward (d) shortwave and (e) longwave radiation from Met City (SWD, SWU, LWD and LWU, respectively); (f) 2-m (black, left axis) and surface temperatures (blue, left axis), and turbulent sensible (red, right axis) and latent (orange, right axis) heat fluxes (Hs and Hl, respectively) all derived from the Met City tower.

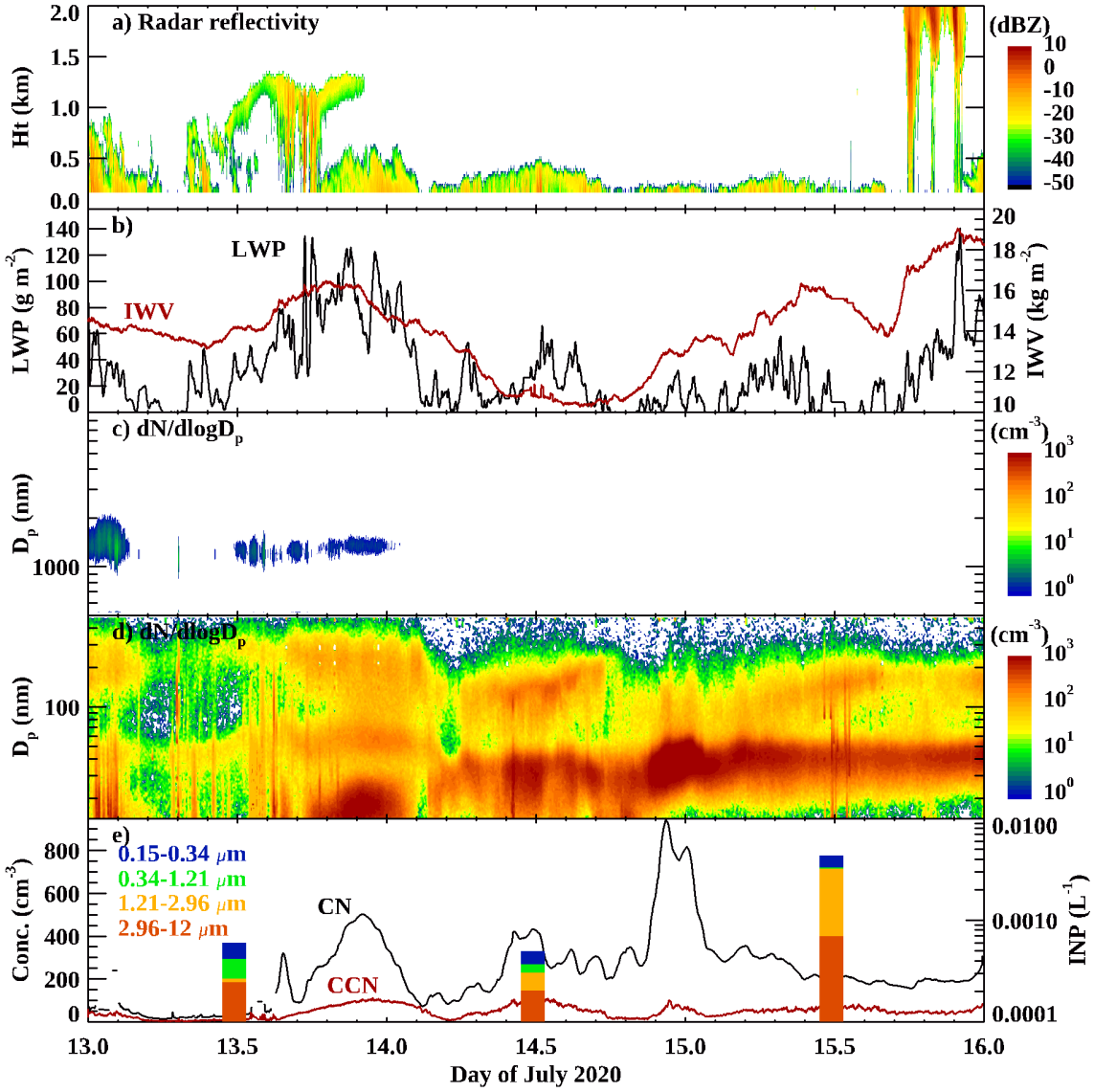

1424 **Figure 19. Cloud and aerosol measurements for the July 13–15 case.**
1425 (a) Radar reflectivity from the KAZR; (b) integrated water vapor (IWV, red) and liquid water
1426 path (LWP, black) derived from the HATPRO; aerosol size distributions (D_p) from the (c)
1427 aerodynamic particle sizer and (d) scanning mobility particle sizer; and time series
1428 concentrations of (e) total particles (CN, black, left axis) measured by condensation particle
1429 counter, total cloud condensation nuclei (CCN) at 0.4% supersaturation (red, left axis), and ice-
1430 nucleating particles (INP) in different size ranges (color bars, right axis). Note the occasional
1431 ship pollution visible from the spiky vertical lines in (d).
1432
1433

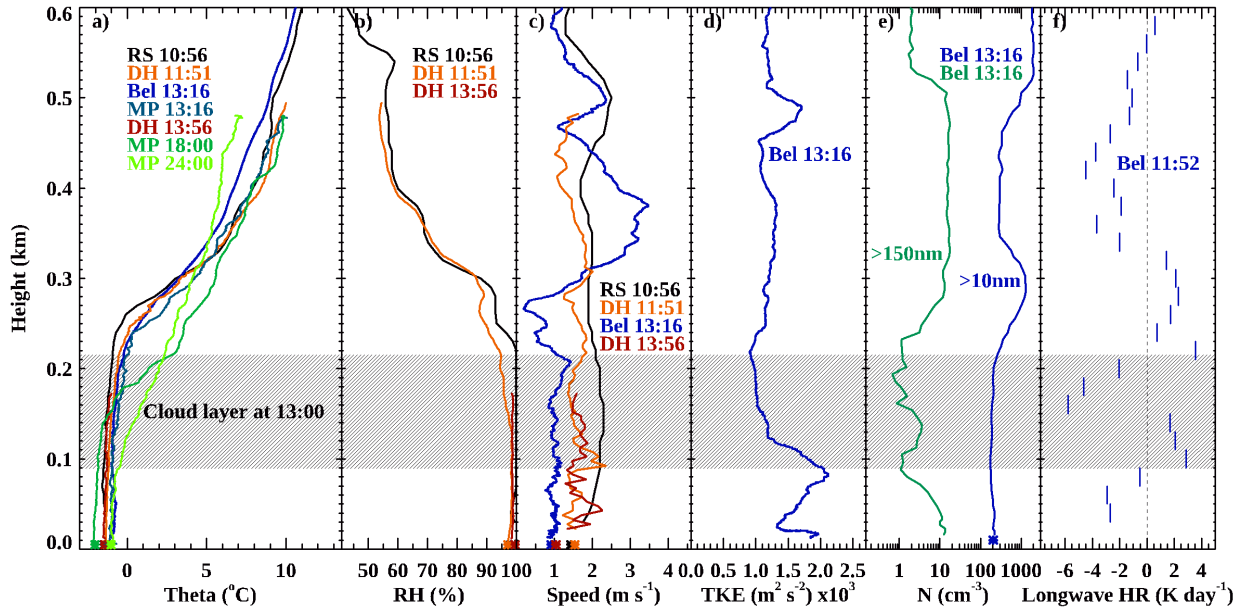

Figure 20. Profile measurements on July 15 of the summer case.
(a) Potential temperature from BELUGA (blue), two DataHawk2 profiles (red, orange), three selected Distributed Temperature Sensing profiles from Miss Piggy (shades of green) and the nearest-in-time radiosonde profile (black); (b) relative humidity (RH) measurements from two DataHawk2 profiles (red, orange) and the nearest-in-time radiosonde profile (black); (c) wind speed from BELUGA (blue), two DataHawk2 profiles (red, orange) and the nearest-in-time radiosonde profile (black); (d) turbulent kinetic energy (TKE) from BELUGA; e) aerosol particle number concentrations (N) from BELUGA for particles larger than 10 nm (blue) and larger than 150 nm (green); and f) long-wave radiative heating rate (HR) profiles from BELUGA. In all cases the equivalent near-surface measurement derived from either the Met City tower or the aerosol measurements onboard *Polarstern* is included as an appropriately colored asterisk. The approximate location of the cloud layer at 13:00 (all times in UTC) is shown in shading.

4. Perspectives and impacts

Collectively, the MOSAiC atmospheric program has provided a wealth of measurements and experiences that build on the past history of Arctic atmospheric observations and will feed a broad range of scientific and operational needs for many years to come. In this section we discuss the expected impacts of the atmospheric program on atmospheric and coupled system science, on modeling, and on the advancement of Arctic observing capabilities. While many of these research activities are currently underway, the topics can also serve as guidance to a wide user community on how these new observations can be further exploited.

4.1 Atmospheric and coupled system science across scales

A vast amount of new, and in many ways transformational, science will be enabled by the MOSAiC observations. Early assessment of the collected data suggests that we can anticipate the

following key results, products, and studies to advance our understanding of the Arctic atmosphere. Each has been annotated numerically to delineate a link to the specific numbered science questions listed in Section 1.

- Comprehensive characterization of aerosol physical and chemical properties over an annual cycle, including annual descriptions of CCN and INP, and a cross comparison of aerosol observations by multiple instruments (3)
- Assessment of local sources of atmospheric aerosols (3, 4)
- Quantification of seasonally varying surface gas fluxes over all surface types, including open ocean, melt ponds, first-year ice, and multi-year ice (1, 4)
- Characterization of atmospheric composition and chemistry of both long-lived climate forcing and reactive gases (4)
- Characterization of cloud phase, properties, and precipitation in all seasons, including derivation and intercomparison of comprehensive cloud products (3)
- Multivariate examination of the surface energy budget over sea ice and the drivers of its variability, including assessment of spatial heterogeneity and the closure between net energy budgets and sea-ice mass balance (1–3, 5)
- Ground observation assessment of satellite-derived surface radiative fluxes to improve satellite techniques and enable pan-Arctic studies of surface radiative balance (1, 3, 5)
- Detailed description of ABL structure, including its relationship with seasonal processes, advective forcing, leads, and other influences (1–3)
- Combined sensor characterization of ABL wind profiles and low-level jets, including a comprehensive comparison of different sensors and techniques (1–3)
- In-depth analysis of numerous storms, with links to large-scale circulation, troposphere-stratosphere interactions, precipitation, and surface impacts (1–3, 5)
- Characterization of the water isotopic fingerprints of pan-Arctic moisture processes and their relation to surface conditions, extreme events, and synoptic variability (3, 5)
- Cross-cutting, unified set of merged observatory data files that are designed for model assessment and process studies, comprised of detailed atmosphere and coupled system measurements on a unified time-height grid (1–3, 5)

At its core, MOSAiC was designed to be a multidisciplinary project, cutting across key interfaces in the Arctic system. Thus, there are abundant ways in which the atmospheric observations can also be combined with those from the other MOSAiC teams to address cross-disciplinary knowledge gaps and support coupled system science. Many of these interactions can be examined over periodic events such as storms, within the context of seasonal variability, and over a variety of other spatial and temporal scales. As above, each of these topics is annotated numerically to delineate a link to overarching science questions from Section 1.

- *Momentum exchange*. Atmospheric winds and ocean currents are the sources of momentum across the coupled system, with sea ice sitting at the interface. To understand sea ice dynamics, and to some degree the structure of the upper ocean and gas transfer across the system, requires an assessment of momentum transfer at both the top and bottom interfaces of the sea ice. While momentum transfer occurs in most conditions, atmospheric storms are a particularly interesting time to study this kinetic coupling. (2, 5)
- *Thermodynamics*. The energy budgets of the snow, sea ice, and ocean mixed layer are the result of highly coupled processes. Across much of the Arctic, the largest contributions to these energy budgets are atmospheric heat and latent heat fluxes, and importantly

summer solar insolation. Atmospheric fluxes are also largely responsible for removing accumulated heat in the ocean mixed layer prior to the onset of fall freeze up and through leads that open in the sea ice during winter. These coupled thermodynamic processes are closely linked with the snow and sea ice mass balance through their controls on growth and melt. (1–3, 5)

- *Light*. Sunlight is essential for photochemical processes as well as photosynthesis to support biological productivity in the Arctic Ocean and sea ice. While the maximum potential available sunlight is simply based on sun angle, atmospheric processes can exert significant influence on the incoming solar radiation that is available at the surface to enter the snow, ice, and ocean and affect light-sensitive processes. (1–5)
- *Gas transfer*. Many key cycles, such as the carbon cycle, link across the fully coupled system and are driven by the movement of gases across interfaces. Air-ocean and air-ice gas exchanges are dependent on winds and the seasonal evolution of the surface type distribution. These exchanges are closely linked with the ecosystem and biogeochemical processes in the ice and ocean. Moreover, gas transfer is central to global-scale processes such as the uptake of carbon dioxide by the ocean. (1, 4)
- *Aerosol sources*. Source attribution for aerosols in the central Arctic is not well understood, but local sources are hypothesized to be important. Biogenic particles that could serve important roles in cloud formation are found in ocean water and sea ice, and wind or bubbles might inject these particles into the atmosphere where they can then become available for growth and/or cloud particle nucleation. Similarly, aerosol precursors emitted from open water or melt ponds, might also contribute to local new aerosol particle formation. (3–5)
- *Snowfall and snow*. Snowfall is the primary sink of moisture from the atmosphere in winter and can limit the lifetime of clouds, and thus their radiative effects on the surface. Snowfall is also the source of snow on the surface, serving as one contribution to the surface mass budget. Surface snow also influences the surface albedo and functions as an insulating layer between the atmosphere and sea ice, both of which impact heat transfer. Atmospheric winds serve to erode and redistribute snow and its contents. Snow also acts as a vehicle for wet deposition of atmospheric particles and a substrate for chemical reactions. (3, 5)
- *Water cycle*. Water vapor is a critical cross-cutting parameter that couples the Arctic system spatially and temporally. Evaporation serves as a moisture source for the atmosphere and is highly dependent on local surface types, ranging from terrestrial land surfaces to open ocean, sea ice, and leads. Moisture transport and transformation within the atmosphere affects the spatial distribution and properties of clouds and precipitation. Importantly, large-scale moisture advection also links the central Arctic with lower latitudes. Precipitation completes the cycle, affecting local hydrological processes, freshwater budgets, and ecosystems. (1, 3, 5)

MOSAiC observed a single region of the Arctic for a single year, and therefore offers a very detailed but spatio-temporally limited perspective on the Arctic system. With this limitation in mind, MOSAiC has been designed in some ways to bridge across multiple scales to understand the variability of Arctic processes and to place them within a broader context. At local and meso-scales, the MOSAiC CO combined with the DN, at least over the winter season, offered four points with which to study spatial gradients related to advecting air masses, frontal passages, or

other mesoscale features. These observations can give insight into atmospheric divergence with potential influences on divergence in the sea ice. Moreover, these multiple points within approximately 20 km of each other, give some constraint on sub-grid variability in large-scale models and satellite remote sensing products. Stepping out to a regional scale, the aircraft observations made during the late summer, while not reaching *Polarstern* itself, can be linked with the MOSAiC surface observations via air mass trajectories both onto, and off of, the sea ice. At least two of the flights are well suited to this approach for examining processes related to air mass transformation. Lastly, there is much to learn about spatio-temporal variability by placing MOSAiC within the pan-Arctic setting through comparisons with the historical and ongoing measurements at land-based observatories. For example, assessing how the MOSAiC observations compare with longer-term analyses of atmospheric structure (e.g., Maturilli and Kayser, 2017), clouds (Dong et al., 2010; Shupe et al., 2011), water vapor and precipitation isotopes (Klein et al., 2016), aerosols (Schmeisser et al., 2018), and other parameters at these Arctic observatories will be essential. Additionally, during the MOSAiC year there was a second intensive atmospheric facility deployed by the DOE ARM program on the northern coast of Norway for the Cold-Air Outbreaks in the Marine Boundary Layer Experiment (COMBLE; Geerts et al., 2021). These contemporaneous deployments offer the unique ability to link the similar atmospheric observations made at the MOSAiC, Ny-Ålesund, and COMBLE locations to study the evolution of air masses as they transit into, or out of, the Arctic.

4.2 Enabling model studies

Observations from the MOSAiC ATMOS team have great potential to support a wide variety of modeling activities, including model evaluations and assessments, joint observation-model process studies, data assimilation studies, sub-grid-scale parameterization development, and much more. A few examples of these activities are outlined here, some of which are currently being implemented.

Large-eddy simulations and process models. The detailed observations made around the MOSAiC CO were explicitly designed to support high-resolution modeling. Numerous projects are taking shape to use large-eddy simulation (LES) or one-dimensional models to study the small-scale cloud, atmospheric composition, and ABL processes observed in the MOSAiC "grid cell." For example, observations of ABL temperature, moisture, and turbulence structure throughout a wide variety of conditions are enabling studies of ABL processes and transitions, including the strongly stratified turbulence that frequently occurs under clear skies with little sunlight. Similarly, the effect of periodic leads on the ABL structure can vary both as a function of season and proximity, often acting to erode otherwise stable stratification. Additionally, leads can serve as a significant source of moisture to the atmosphere, and observation-constrained LES is an essential tool to examine how leads impact the moisture profile and energy fluxes, including at cloud level. High resolution LES depictions of these lead impacts can also be upscaled to support their representation in larger-scale models. Finally, low-level stratiform clouds are very common, and LES can offer insight into the balance of processes at play during the early stages of cloud development in stable, non-turbulent conditions. These models are well positioned to then simulate the progression of these clouds in time and space, as associated air mass transformations affect moisture availability, atmospheric structure, the concentration of aerosols, and additional processes. Complementing these LES studies, one-dimensional climate-

chemistry models can examine atmospheric trace gases, their surface fluxes, and other interactions across the ABL to better understand the implications for physical and biogeochemical exchange processes. Research teams are currently using MOSAiC observations to constrain and evaluate model simulations targeting all of these important processes.

Process-based model evaluation. MOSAiC observations are being used to directly evaluate coupled processes unique to the Arctic (i.e., mixed-phase clouds, stable boundary layers, atmosphere-snow interactions, ocean-ice-atmosphere coupling) in an hierarchy of models. In a near real-time verification project, developed as part of YOPP, short-term forecasts are evaluated using observation-based process diagnostics. This evaluation is done to identify potential errors in the representation of "fast" processes, such as cloud feedbacks and surface fluxes, that cause systematic biases in climate model projections of Arctic change. Initially forecasts from nine experimental and operational forecast systems are included in the evaluation. One example process relationship used to assess the models is the observed relationship between the scaled sensible heat flux and the near-surface stratification (Figure 21), here compared to the NOAA Physical Sciences Laboratory Coupled Arctic Forecast System (CAFS). The slope of the relationship between these parameters is proportional to the transfer coefficient used in bulk parameterizations for the sensible heat flux. Observations from the three ASFS deployed in the DN show that the transfer coefficient is not a constant and that for near-surface temperature gradients greater than 2°C, the sensible heat flux decreases and then goes to zero for the largest values. A comparison of bin-averaged values (Figure 21d) shows that CAFS is able to simulate the observed relationship under weak stratification because the sea ice model (CICE5) used in this fully-coupled system includes similarity functions that take the observed non-linear relationship into account. However, this forecast system, and others in the study (not shown), still underestimate the occurrence of strongly stable conditions. While simulating the process interaction shown in Figure 21 is a significant accomplishment, the misrepresentation of strongly stable conditions motivates the need for multivariate diagnostics that can be used to further attribute the causes of these errors and then improve the simulation of strongly stable conditions. Process-based model assessments of this type are one important way to overcome the inherent temporal limitations of a field expedition like MOSAiC.

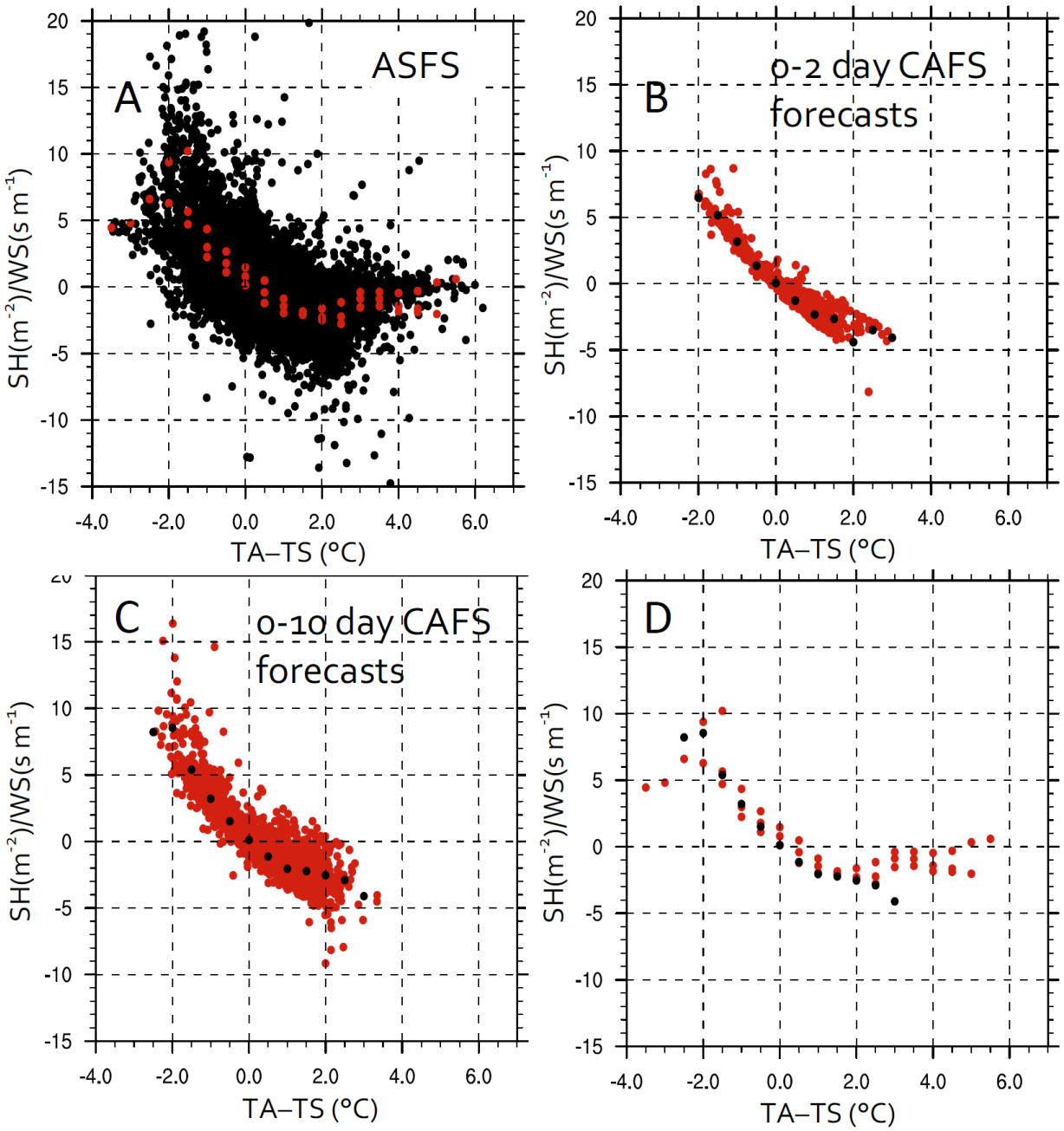

Figure 21. An example of process-based model evaluation.
(A) Ten-minute average observations of scaled sensible heat fluxes (2-m sensible heat flux divided by 2-m wind speed, in units of W s m^{-3}) relative to near-surface stratification (2-m air temperature minus skin temperature, in °C) from three ASFS flux stations (black) and values binned for each flux station individually in intervals of 0.5°C (red). (B) Same as (A) but from 6-hourly output from 0–2 day forecasts from CAFS. (C) Same as (B) but using the CAFS 0–10 day forecasts to show that the model is not drifting into a different state. (D) Binned values from (A) and (C) to compare the observations (red) and model (black) forecasts more closely.

Model simulations of air mass transformation. Warm air intrusions have been identified as important events as they have the ability to rapidly shift the surface energy budget, leading to

temperature increases and surface melt (Pithan et al., 2018). As a complementary MOSAiC activity targeting these warm air intrusions, the YOPP organized support from national Met Services to be on stand-by to release extra radiosondes at their regular stations. Using targeted forecast products from the European Center for Medium-range Weather Forecasts, the circulation patterns and northward moisture advection were followed closely from March 2020 onwards, and when the first spring intrusion was forecast the participating stations contributed to this targeted observing period. This effort resulted in more than 50 extra soundings during April 12–20, including extra soundings at *Polarstern*. The targeted period covered two warm air intrusions on April 16 and 19, when over this short period of time the temperature increased at *Polarstern* from –30˚C to very close to 0˚C on April 16 then cooled to below –15˚C for a day before the second intrusion pushed the temperature back to 0˚C. Back-trajectory analysis revealed that during the first event the warm, moist and cloudy air came to *Polarstern* from the southeast, while during the second event the air rapidly advected from the south, with some component passing over Greenland. This case is being used by the YOPP-MOSAiC modeling community for a model intercomparison study to examine the ability of models to capture Lagrangian air mass transformation along the trajectories. For this purpose and others, a specialized merged observatory data file product is being developed to be used by the wider community for model assessment and improvement.

Impact of radiosonde measurements on data assimilation. Due to the dearth of radiosondes launched over the Arctic Ocean, the initial atmospheric conditions for numerical weather forecast models and reanalyses are subject to large uncertainties that can contribute to errors in the evolution of large-scale atmospheric circulation. As a pilot study for MOSAiC, the Arctic Research Collaboration for Radiosonde Observing System Experiment (September 2013) involved launching many extra radiosondes across the Arctic to support assimilation studies using the Japanese Earth Simulator forecast model. The inclusion of the additional Arctic radiosondes improved initial atmospheric conditions and the overall skill of weather and sea ice forecasts in the Arctic (e.g., Inoue et al., 2015), with more realistic representation of ABL processes, radiation, and turbulent fluxes, their influence on cyclogenesis, and their interaction with the surface. Predictions of the polar vortex and mid-tropospheric wind were significantly improved. Similar studies have demonstrated that additional Arctic radiosonde observations can also have substantial impacts on the representation of extratropical cyclones, cold air outbreaks, the polar vortex structure, and other features that influence mid-latitude weather in both winter and summer (e.g., Sato et al., 2017; Sato et al., 2018). These results provided guidance for MOSAiC's four-times daily radiosonde program over the full annual cycle, in addition to periodic additional radiosondes at other Arctic stations during special observing periods as part of YOPP. All of these radiosonde profiles were fed into the WMO Global Telecommunication System (GTS), making them available in real-time for Numerical Weather Prediction data assimilation and verification systems (e.g., Hori et al., 2021). These additional observations provide an unprecedented opportunity to evaluate assimilation systems and to further study the implications of additional central Arctic observations for improved forecasts in all seasons.

4.3 Improving observing technologies

In addition to addressing science questions and advancing modeling capabilities, MOSAiC was also a tremendous opportunity to improve numerous observing technologies with the potential

for lasting impact on Arctic observing capabilities. For example, significant work was done to prepare, implement, and evaluate the robustness of robotic and autonomous measurement systems in this challenging environment. Autonomous measurements of surface energy fluxes, especially radiative and turbulent, have long been understood to be very challenging as a result of cold temperatures, instrument icing, and other considerations (e.g., Bourassa et al., 2013). The ASFS developed for MOSAiC successfully collected a robust set of measurements with little impact from icing, even in a semi-autonomous mode. While issues related to ice dynamics and polar bears are likely unavoidable, the experience gained through MOSAiC will enable these systems to become more autonomous through improvements to power generation and management.

MOSAiC also represents one of the first extended duration deployments of small UAS for scientific purposes in the Arctic. These platforms offered new insights into atmospheric and surface conditions, capturing details of the spatial variability of key quantities. Such sampling has long posed challenges for UAS due to a variety of reasons. Most directly, navigation systems for commercially available UAS are not generally ready to support operations at the highest latitudes. Due to proximity to the magnetic north pole, the magnetometers of such systems can provide uninformative readings, reducing the ability of the autopilot to guide the aircraft successfully and safely. To overcome this issue, a differential GPS solution was employed to provide DataHawk2 more complete attitude information while in flight, which proved to work very well. Systems were also hardened for cold-weather operations, allowing the DataHawk2 to operate in conditions down to nearly –35˚C. Additionally, multiple teams deployed newly developed multi-rotor platforms with gimbal-stabilized instrumentation to support robust measurements of broadband and spectral radiation.

Extending beyond the surface, MOSAiC is also impacting satellite-based observations of the Arctic. For example, over an intensive period from May 1 to September 15, 2020, the Clouds and Earth's Radiant Energy System (CERES) FM-2 instrument on the Terra satellite was operated in a special scanning mode that enabled it to look at the MOSAiC ship domain from multiple angles as it passed along its polar orbit. Using this unique data set, ground observations from the ATMOS team are contributing to a comprehensive evaluation of CERES-based retrievals of surface and top-of-atmosphere short-wave and long-wave radiative fluxes. A systematic assessment of derived fluxes will be performed as a function of viewing zenith angle, and a series of observation-constrained sensitivity studies will be used to evaluate many of the retrieval assumptions concerning the surface, atmosphere, and cloud properties. Similar evaluations can harness atmospheric observations to evaluate cloud, aerosol, water vapor, and temperature observations from a variety of other satellites (e.g., Crewell et al., 2021). Ultimately, these evaluations will help to improve satellite-based observations and reduce the overall uncertainty of pan-Arctic radiative budgets.

5. Conclusions

The breadth and depth of material summarized in this manuscript makes evident that the MOSAiC atmosphere program was broadly successful. This program has delivered, by far, the most comprehensive and sophisticated data set to characterize the annual cycle of central Arctic atmospheric properties to date. The observations cover all significant atmospheric variables in a

thorough manner and extend well beyond prior observational activities in the central Arctic. Moreover, when considered alongside the similarly comprehensive programs examining the sea ice/snow, ocean, ecosystem, and biogeochemistry conducted during MOSAiC, these activities collectively represent an entirely unprecedented observational accomplishment. Some key indicators of success include:

- As the majority of atmospheric observations were made onboard *Polarstern*, there was a remarkable degree of measurement continuity over the annual cycle, in spite of the incessant challenges posed by sea ice dynamics, and the necessity to move the ship for logistical purposes.
- A consistent, 4-times daily radiosonde data set was obtained that provides a continuous characterization of the basic atmospheric structure. These measurements provide a wealth of data for use by the operational weather forecasting community, will support the development of more reliable reanalysis products for the MOSAiC year, and will enable model assimilation impact studies.
- Continuous measurements in all seasons, and most importantly winter, filled critical gaps in atmospheric chemical composition, chemical reactivity, and aerosol observations in the central Arctic.
- The atmospheric program achieved many observational "firsts", for example: scanning cloud radar operations within the Arctic ice pack; annual cycle of central Arctic ice-nucleating particle concentrations; long-term, high-temporal resolution humidity profiling over sea ice; most extensive scientific operation to date of small UAS over the central Arctic; annual cycle of surface fluxes of climate-active trace gases in the central Arctic; routine operations of a calibrated temperature-sensing fiber-optic cable over the sea ice; and full year of high-resolution ABL wind profiles over sea ice.
- The measurements within the atmospheric program successfully documented the atmospheric properties and processes, and their interactions with the surface, during a year that included a persistent and influential large-scale circulation pattern, and many significant weather events.
- Redundant measurements in some areas provide a multi-seasonal data set for comparing measurement systems and methodologies, including for wind profiling, aerosol concentrations, determination of ABL properties, and surface energy budget terms.
- The collected data set will clearly enable coupled system research, cutting across multiple aspects of the Arctic system, in a manner that has not been accomplished in the past.
- The produced data sets have already set a new baseline to evaluate model processes, assess model biases, and develop model parameterizations.

Data are an important legacy for MOSAiC. Members of the ATMOS team are working diligently to quality-control all data sets and prepare them for public archival. In many cases, subsets of the data are already publicly available, while all will be made public by the start of 2023. Users are encouraged to engage the MOSAiC data for many purposes. Overall, the atmospheric program, and MOSAiC more broadly, are clearly making a generational contribution to Arctic research. This wealth of new information, at this important time of rapid Arctic and global change, will enable and support cross-cutting research for decades to come.

References

Akperov, M, Mokhov, I, Rinke, A, Dethloff, K, Matthew H. 2015. Cyclones and their possible changes in the Arctic by the end of the twenty first century from regional climate model simulations. *Theoretical Applications in Climatology* **122**: 85–95, https://doi.org/10.1007/s00704-014-1272-2.

Ancellet, G, Pelon, J, Blanchard, Y, Quennehen, B, Bazureau, A, Law, KS, Schwarzenboeck, A. 2014. Transport of aerosol to the Arctic: analysis of CALIOP and French aircraft data during the spring 2008 POLARCAT campaign. *Atmospheric Chemistry and Physics* **14**: 8235–8254, https://doi.org/10.5194/acp-14-8235-2014.

Andreas, EL, Persson, POG, Grachev, AA, Jordan, RE, Horst, TW, Guest, PS, Fairall, CW. 2010. Parameterizing turbulent exchange over sea ice in winter. *Journal of Hydrometeorology* **11**: 87–104, https://doi.org/10.1175/2009JHM1102.1.

Baccarini, A, Karlsson, L, Dommen, J, Duplessis, P, Vüllers, J, Brooks, IM, Saiz-Lopez, A, Salter, M, Tjernstrom, M, Baltensperger, U, Zieger, P, Schmale, J. 2020. Frequent new particle formation over the high Arctic pack ice by enhanced iodine emissions. *Nature Communications* **11**(1): 4924, https://doi.org/10.1038/s41467-020-18551-0.

Bailey, H, Klein, ES, Welker, JM. 2019. Synoptic and mesoscale mechanisms drive winter precipitation d18O/d2H in South-Central Alaska. *JGR Atmospheres* **124**: 4252–4266, https://doi.org/10.1029/2018JD030050.

Banta, B, Pichugina, YL, Brewer, WA. 2006. Turbulent velocity-variance profiles in the stable boundary layer generated by a nocturnal low-level jet. *Journal of Atmospheric Sciences* **63**: 2700–2719, https://doi.org/10.1175/JAS3776.1.

Bintanja, R, van der Wiel, K, van der Linden, EC, Reusen, J, Bogerd, L, Krikken, F, Selten, FM. 2020. Strong future increases in Arctic precipitation variability linked to poleward moisture transport. *Science Advances* **6**, https://doi.org/10.1126/sciadv.aax6869.

Boisvert, LN, Markus, T, Vihma, T. 2013. Moisture flux changes and trends for the entire Arctic in 2003-2011 derived from EOS Aqua data. *Journal of Geophysical Research* **118**: 5829–5843, https://doi.org/10.1002/jgrc.20414.

Bourassa, MA, Gille, ST, Bitz, C, Carlson, D, Cerovecki, I, Clayson CA, Cronin, MF, Drennan, WM, Fairall, CW, Hoffman, RN, Magnusdottier, G, Pinker, RT, Renfrew, IA, Serreze, M, Speer, K, Talley, LD, Wick, GA. 2013. High-latitude ocean and sea ice surface fluxes: Challenges for climate research. *Bulletin of the American Meteorological Society* **94**(3): 403–423, https://doi.org/10.1175/BAMS-D-11-00244.1.

Brock, CA, Cozic, J, Bahreini, R, Froyd, KD, Middlebrook, AM, McComiskey, A, Brioude, J, Cooper, OR, Stohl, A, Aikin, KC, de Gouw, JA, Fahey, DW, Ferrare, RA, Gao, R-S, Gore, W, Hollohway, JS, Hubler, G, Jefferson, A, Lack, DA, Lance, S, Moore, RH, Murphy, DM, Nenes,

A, Novelli, PC, Nowak, JB, Ogren, JA, Peischl, J, Pierce, RB, Pilewski, P, Quinn, PK, Ryerson, RB, Schmidt, KS, Schwarz, JP, Sodemann, H, Spackman, JR, Stark, H, Thomson, DS, Thornberry, T, Veres, P, Watts, LA, Warneke, C, Wollny, AG. 2011. Characteristics, sources, and transport of aerosols measured in spring 2008 during the aerosol, radiation, and cloud processes affective Arctic Climate (ARCPAC) Project. *Atmospheric Chemistry and Physics* **11**: 2423–2453, https://doi.org/10.5194/acp-11-2423-2011.

Brümmer, B, Müller, G, Affeld, B, Gerdes, R, Karcher, M, Kauker, F. 2006. Cyclones over Fram Strait: impact on sea ice and variability. *Polar Research* **20**: 147–152, https://doi.org/10.1111/j.1751-8369.2001.tb00050.x.

Bühl, J, Seifert, P, Myagkov, A, and Ansmann, A. 2016. Measuring ice- and liquid-water properties in mixed-phase cloud layers at the Leipzig Cloudnet station. *Atmospheric Chemistry and Physics* **16**: 10609–10620, https://doi.org/10.5194/acp-16-10609-2016.

Calhoun, R, Heap, R, Princevac, M, Newsom, R, Fernando, H, Ligon, D. 2006. Virtual towers using coherent Doppler lidar during the Joint Urban 2003 Dispersion Experiment. *Journal of Applied Meteorology and Climatology* **45**: 1116–1126, https://doi.org/10.1175/JAM2391.1.

Cavallo, SM, Hakim, GJ. 2010. Composite structure of tropopause polar cyclones. *Monthly Weather Review* **138**: 3840–3857, https://doi.org/10.1175/2010MWR3371.1.

Cohen, J, Zhang, X, Francis, J, Jung, T, Kwok, R, Overland, J, Ballinger, TJ, Bhatt, US, Chen, HW, Coumou, D, Feldstein, S, Gu, H, Handorf, D, Henderson, G, Ionita, M, Kretschmer, M, Laliberte, F, Lee, S, Linderholm, HW, Maslowski, W, Peings, Y, Pfeiffer, K, Rigor, I, Semmler, T, Stroeve, J., Taylor, PC, Vavrus, S, Vihma, T, Wang, S, Wendisch, M, Wu, Y, Yoon, J. 2020. Divergent consensuses on Arctic amplification influence on midlatitude severe winter weather. *Nature Climate Change* **10**: 20–29, https://doi.org/10.1038/s41558-019-0662-y.

Cohen, L, Hudson, SR, Walden, VP, Graham, RM, Granskog, MA. 2017. Meteorological conditions in a thinner Arctic sea ice regime from winter to summer during the Norwegian Young Sea ice expedition (N-ICE2015). *Journal of Geophysical Research* **122**: 7235–7259, https://doi.org/10.1002/2016JD026034.

Coumou, D, Di Capua, G, Vavrus, S, Wang, L, Wang, S. 2018. The influence of Arctic amplification on mid-latitude summer circulation. *Nature Communications* **9**: 2959, https://doi.org/10.1038/s41467-018-05256-8.

Cox C, Gallagher, M, Shupe, M, Persson, O, Solomon, A, Blomquist, B, Brooks, I, Costa, D, Gottas, D, Hutchings, J, Osborn, J, Morris, S, Preusser, A, Uttal, T. 2021a. 10-meter (m) meteorological flux tower measurements (Level 1 Raw), Multidisciplinary Drifting Observatory for the Study of Arctic Climate (MOSAiC), central Arctic, October 2019 - September 2020. Arctic Data Center. doi:10.18739/A2VM42Z5F.

Cox, C, Gallagher, M, Shupe, M, Persson, O, Solomon, A, Ayers, T, Costa, D, Hutchings, J, Leach, J, Morris, S, Osborn, J, Pezoa, S, Uttal, T. 2021b. Atmospheric Surface Flux Station #30

measurements (Level 1 Raw), Multidisciplinary Drifting Observatory for the Study of Arctic Climate (MOSAiC), central Arctic, October 2019 - September 2020. Arctic Data Center. doi:10.18739/A20C4SM1J.

Creamean, JM, Cross, JN, Pickart, R, McRaven, L, Lin, P, Pacini, A, Hanlon, R, Schmale, DG, Ceniceros, J, Aydell, T, Colombi, N, Bolger, E, DeMott, PJ. 2019. Ice nucleating particles carried from below a phytoplankton bloom to the Arctic atmosphere. *Geophysical Research Letters* **46**: 8572–8581, https://doi.org/10.1029/2019GL083039.

Creamean, J. 2020. Size-resolved ice nucleating particle (INP) concentrations from the MOSAiC campaign. Atmospheric Radiation Measurement (ARM) user facility. https://doi.org/10.5439/1798162.

Crewell, S, Ebell, K, Konjari, P, Mech, M, Nomokonova, T, Radovan, A, Strack, D, Triana-Gómez, AM, Noël, S, Scarlat, R, Spreen, G, Maturilli, M, Rinke, A, Gorodetskaya, I, Viceto, C, August, T, Schröder, M. 2021. A systematic assessment of water vapor products in the Arctic: from instantaneous measurements to monthly means. *Atmospheric Measurement Techniques* 14: 482904856. https://doi.org/10.5194/amt-14-4829-2021.

Curry, JA, Hobbs, PV, King, MD, Randall, DA, Minnis, P, Isaac, GA, Pinto, JO, Uttal, T, Bucholtz, A, Cripe, DG, Gerber, H, Fairall, CW, Garrett, TJ, Hudson, J, Intrieri, JM, Jakob, C, Jensen, T, Lawson, P, Marcotte, D, Nguyen, L, Pilewski, P, Rangno, A, Rogers, DC, Strawbridge, KB, Valero, FPJ, Williams, AG, Wylie, D. 2000. FIRE Arctic Clouds Experiment. *Bulletin of the American Meteorological Society* **81**: 5–30, https://doi.org/10.1175/1520-0477(2000)081<0005:FACE>2.3.CO;2.

Dethloff, K, Maslowski, W, Hendricks, S, Lee, Y, Goessling, HF, Krumpen, T, Haas, C, Handorf, D, Ricker, R, Bessonov, V, Cassano, JJ, Kinney, JC, Osinski, R, Rex, M, Rinke, A, Sokolova, J, Sommerfeld, A. 2021. Arctic sea ice anomalies during the MOSAiC winter 2019/20. *The Cryosphere Discussions*, under review. https://doi.org/10.5194/tc-2020-375.

Dlugokencky, EJ, Steele, LP, Lang, PM, Masarie, KA. 1995. Atmospheric methane at Mauna Loa and Barrow observatories: Presentation and analysis of in situ measurements. *Journal of Geophysical Research* **100**: 23103–23113. https://doi.org/10.1029/95JD02460.

Dong, X, Xi, B, Crosby, K, Long, CN, Stone, RS, Shupe, MD. 2010. A 10-year climatology of Arctic cloud fraction and radiative forcing at Barrow, Alaska. *Journal of Geophysical Research* **115**, D17212, https://doi.org/10.1029/2009JD013489.

Drüe, C, Heinemann, G. 2001. Airborne investigation of Arctic boundary layer fronts over the marginal ice zone of the Davis Strait. *Boundary Layer Meteorology* **101**: 261–292, https://doi.org/10.1023/A:1019223513815.

Edel, L, Claud, C, Genthon, C, Palerme, C, Wood, N, L'Ecuyer, R., Bromwich, D. 2020. Arctic snowfall from CloudSat observations and reanalyses. *Journal of Climate* **33**: 2093–2109, https://doi.org/10.1175/JCLI-D-19-0105.1.

Egerer, U, Gottschalk, M, Siebert, H, Ehrlich, A, Wendisch, M. 2019. The new BELUGA setup for collocated turbulence and radiation measurements using a tethered balloon: first applications in the cloudy Arctic boundary layer. *Atmospheric Measurement Techniques* **12**: 4019–4038, https://doi.org/10.5194/amt-12-4019-2019.

Ehrlich, A, Wendisch, M, Lüpkes, C, Buschmann, M, Bozem, H, Chechin, D, Clemen, HC, Dupuy, R, Eppers, O, Hartmann, J, Herber, A, Jäkel, E, Järvinen, E, Jourdan, O, Kästner, U, Kliesch, LL, Köllner, F, Mech, M, Mertes, S, Neuber, R, Ruiz-Donoso, E, Schnaiter, M, Schneider, J, Stapf, J, Zanatta, M. 2019. A comprehensive in situ and remote sensing data set from the Arctic CLoud Observations Using airborne measurements during polar Day (ACLOUD) campaign. *Earth System Science Data* **11**: 1853–1881, https://doi.org/10.5194/essd-11-1853-2019.

Freud, E, Krejci, R, Tunved, P, Leaitch, R, Nguyen, QT, Massling, A, Skov, H, Barrie, L. 2017. Pan-Arctic aerosol number size distributions: seasonality and transport patterns. *Atmospheric Chemistry and Physics* **17**: 8101–8128, https://doi.org/10.5194/acp-17-8101-2017.

Frolov, IE, Gudkovich, ZM, Radionov, VF, Shirochkov, AV, Timokhov, LA. 2005. The Arctic Basin – Results from the Russian Drifting Stations. Berlin: Springer. https://doi.org/10.1007/3-540-37665-8.

Galewsky, J, Steen-Larsen, HC, Field, RD, Worden, J, Risi, C, Schneider, M. 2016. Stable isotopes in atmospheric water vapor and applications to the hydrologic cycle. *Reviews in Geophyiscs*, **54**: 809–865, doi:10.1002/2015RG000512.

Gascard, J-C, Festy, J, le Goff, H, Weber, M, Bruemmer, B, Offermann, M, Doble, M, Wadhams, P, Forsberg, R, Hanson, S, Skourup, H, Gerland, S, Nicolaus, M, Metaxian, J-P, Grangeon, J, Haapala, J, Rinne, E, Haas, C, Wegener, A, Heygster, G, Jakobson, E, Palo, T, Wilkinson, J, Kaleschke, L, Claffey, K, Elder, B, Bottenheim, J. 2008. Exploring Arctic transpolar drift during dramatic sea ice retreat. *Eos Transactions* **89**: 21–28, https://doi.org/10.1029/2008EO030001.

Geerts, B., McFarquhar, G, Xue, L, Jensen, M, Kollias, P., Ovchinnikov, M., Shupe, M, DeMott, P, Wang, Y, Tjernstrom, M, Field, P, Abel, S, Spengler, T, Neggers, R, Crewell, S, Wendisch, M, Luepkes, C. 2021. Cold-Air Outbreaks in the Marine Boundary Layer Experiment (COMBLE) Field Campaign Report. U. S. Department of Energy technical report, DOE/SC-ARM-21-001. Available: https://www.arm.gov/publications/programdocs/doe-sc-arm-21-001.pdf.

Gero, J, Garcia, R, Hackel, D, Ermold, B, Gaustad, K. 2019. Atmospheric Emitted Radiance Interferometer (AERICH1). Atmospheric Radiation Measurement (ARM) user facility. https://doi.org/10.5439/1025143.

Groves, DG, Francis, JA. 2002. Moisture budget of the Arctic atmosphere from TOVS satellite data. *Journal of Geophysical Research* **107**: 11.1–11.21, https://doi.org/10.1029/2001JD001191.

Heinemann, G, Willmes, S, Schefczyk, L, Makshtas, A, Kustov, V, Makhotina, I. 2021. Observations and simulations of meteorological conditions over Arctic thick sea ice in late winter during the Transarktika 2019 expedition. *Atmosphere* **12**: 174, https://doi.org/10.3390/atmos12020174.

Herber, AB, Haas, C, Stone, RS, Bottenheim, JW, Liu, P, Li, S-M, Staebler, RM, Strapp, JW, Dethloff, K. 2012. Regular airborne surveys of Arctic sea ice and atmosphere. *Eos Transactions*. **93**: 41–42, https://doi.org/10.1029/2012EO040001.

Herman, GF, Curry, JA. 1984. Observational and theoretical studies of solar radiation in Arctic stratus clouds. *Journal of Applied Meteorology and Climatology* **23**: 5–24, https://doi.org/10.1175/1520-0450(1984)023<0005:OATSOS>2.0.CO;2

Hoppel, WA, Frick, GM, Fitzgerald, JW, Larson, RE. 1994. Marine boundary layer measurements of new particle formation and the effects nonprecipitating clouds have on aerosol size distribution. *Journal of Geophysical Research* **99**: 14443–14459, https://doi.org/10.1029/94JD00797.

Hori, ME, Inoue, J, Dethloff, K, Kustov, V. 2021. Near-tropopause bias in the Russian radiosonde-observed air temperature during the YOPP special observing periods in 2018. *Polar Science* **27**: 100601, https://doi.org/10.1016/j.polar.2020.100601.

Illingworth, AJ, Hogan, RJ, O'Connor, EJ, Bouniol D, Brooks, ME, Delanoe, J., Donovan, DP, Eastment, JD, Gaussiat, N, Goddard, JWF, Haeffelin, M, Klein Baltink, H, Krasnov, OA, Pelon, J., Piriou, J-M, Protat, A, Russchenberg, HWJ, Seifert, A, Tompkins, AM, van Zadelhoff, G-J, Vinit, F, Willen, U, Wilson,DR, Wrench, CL. 2007. CloudNet: Continuous evaluation of cloud profiles in seven operational models using ground-based observations. *Bulletin of the American Meteorological Society* **88**: 883–898, https://doi.org/10.1175/BAMS-88-6-883.

Inoue, J, Yamazaki, A, Ono, J, Dethloff, K, Maturilli, M, Neuber, R, Edwards, P, Yamaguchi, H. 2015. Additional Arctic observations improve weather and sea ice forecasts for the Northern Sea Route. *Nature Scientific Reports* **5**: 16868, https://doi.org/10.1038/srep16868.

Jacob, DJ, Crawford, JH, Maring, H, Clarke, AD, Dibb, JE, Emmons, LK, Ferrare, RA, Hostetler, CA, Russel, PB, Singh, HB, Thompson, AM, Shaw, GE, McCauley, E, Pederson, JR, Fisher, JA. 2010. The Arctic Research of the Composition of the Troposphere from Aircraft and Satellites (ARCTAS) mission: design, execution, and first results. *Atmospheric Chemistry and Physics* **10**: 5191–5212, https://doi.org/10.5194/acp-10-5191-2010.

Jaiser, R, Dethloff, K, Handorf, D. 2013. Stratospheric response to Arctic sea ice retreat and associated planetary wave propagation changes. *Tellus* **65**: 1, https://doi.org/10.3402/tellusa.v65i0.19375.

Johnson, K, Scott, T. 2019. Arctic Remote Sensing of Clouds (ARSCL) product using Ka-band ARM Zenith Radars (ARSCLKAZR1KOLLIAS). Atmospheric Radiation Measurement (ARM) user facility. https://doi.org/10.5439/1393437.

Jokinen, T, Sipilä, M, Junninen, H, Ehn, M, Lönn, G, Hakala, J, Petäjä, T, Mauldin III, RL, Kulmala, M, Worsnop, DR. 2012. Atmospheric sulfuric acid and neutral cluster measurements using CI-APi-TOF. *Atmospheric Chemistry and Physics* **12**: 4117–4125, https://doi.org/10.5194/acp-12-4117-2012.

Jozef, G, de Boer, G, Cassano, J, Calmer, R, Hamilton, J, Lawrence, D, Borenstein, S, Doddi, A, Schmale, J, Preusser, A, Argrow, B. 2021. DataHawk2 Uncrewed Aircraft System data from the Multidisciplinary drifting Observatory for the Study of Arctic Climate (MOSAiC) campaign, B1 level. Arctic Data Center. https://doi.org/10.18739/A2VQ2SB8S.

Jung, T, Gordon, ND, Bauer, P, Bromwich, DH, Chevallier, M, Day, JJ, Dawson, J, Doblas-Reyes, F, Fairall, C, Goessling, HF, Holland, M, Inoue, J, Iversen, T, Klebe, S, Lemke, P, Losch, M, Makshtas, A, Mills, B, Nurmi, P, Perovich, D, Reid, P, Renfrew, IA, Smith, G, Svensson, G, Tolstykh, M, Yang, Q. 2016. Advancing polar prediction capabilities on daily to seasonal time scales. *Bulletin of the American Meteorological Society* **97**: 1631–1647, https://doi.org/10.1175/BAMS-D-14-00246.1.

Karlsson, J, Svensson, G. 2013. Consequences of poor representation of Arctic sea ice albedo and cloud-radiation interactions in the CMIP5 model ensemble. *Geophysical Research Letters* **40**: 4374–4379, https://doi.org/10.1002/grl.50768.

Keen, A, Blockley, E, Bailey, DA, Boldingh Debernard, J, Bushuk, M, Delhaye S, Docquier, D, Feltham, D, Massonnet, F, O'Farrell, S, Ponsoni, L, Rodriguez, JM, Schroeder, D, Sward, N, Toyoda, T, Tsujino, H, Vancoppenolle, M, Wyser, K. 2021. An intercomparison of the mass budget of the Arctic sea ice in CMIP6 models. *The Cryosphere* **15**: 951–982, https://doi.org/10.5194/tc-15-951-2021.

Klein, E, Nolan, M, Cable, J, Cherry, J, Welker, JM. 2016. Northern Alaska precipitation and water vapor isotopic measurements applied to McCall Glacier ice core climate reconstructions. *Quaternary Science Research* **131**: 274–284.

Koontz, A, Senum, G. 2019. Cloud Condensation Nuclei Particle Counter (AOSCCN200). Atmospheric Radiation Measurement (ARM) user facility. https://doi.org/10.5439/1223287.

Koontz, A, Flynn, C, Uin, J, Jefferson, A. 2019. Nephelometer (AOSNEPHDRY). Atmospheric Radiation Measurement (ARM) user facility. https://doi.org/10.5439/1228051.

Kretzschmar, J, Stapf, J, Klocke, D, Wendisch, M, Quaas, J. 2020. Employing airborne radiation and cloud microphysics observations to improve cloud representation in ICON at kilometer-scale resolution in the Arctic. *Atmospheric Chemistry and Physics* **20**: 13145–13165, https://doi.org/10.5194/acp-20-13145-2020

Krumpen, T, Birrien, F, Kauker, F, Rachow, T, von Albedyll, L, Angelopoulos, M, Belter, HJ, Bessonov, V, Damm, E, Dethloff, K, Haapala, J, Haas, C, Harris, C, Hendricks, S, Hoelemann, J, Hoppmann, M, Kaleschke, L, Karcher, M, Kolabutin, N, Lei, R, Lenz, J, Morgenstern, A, Nicolaus, M, Nixdorf, U, Petrovsky, T, Rabe, B, Rabenstein, L, Rex, M, Ricker, R, Rohde, J, Shimanchuk, E, Singha, S, Smolyanitsky, V, Sokolov, V, Stanton, T, Timofeeva, A, Tsamados, M, Watkins, D. 2020. The MOSAiC ice floe: Sediment-laden survivor from the Siberian shelf. *Cryosphere* **14**: 2173–2187, https://doi.org/10.5194/tc-14-2173-2020.

Krumpen, T, von Albedyll, L, Goessling, HF, Hendricks, S, Juhls, B, Spreen, G, Willmes, S, Jakob, Belter, H, Dethloff, K, Haas, C, Kaleschke, L, Katlein, C, Tian-Kunze, X, Ricker, T, Rostovsky, P, Rueckert, J, Singha, S, Sokolova, J. 2021. MOSAiC drift expedition from October 2019 to July 2020: sea ice conditions from space and comparison with previous years. *The Cryosphere* **15**: 3897–3920. https://doi.org/10.5194/tc-2021-80.

Kwok, R. 2018. Arctic sea ice thickness, volume, and multiyear ice coverage: Losses and coupled variability (1958–2018). *Environmental Research Letters* **13**: 105005, https://doi.org/10.1088/1748-9326/aae3ec.

Lawrence, ZD, Perlwitz, J, Butler, AH, Manney, GL, Newman, PA, Lee, SH, Nash, ER. 2020. The remarkably strong Arctic stratospheric polar vortex of winter 2020: Links to record-breaking Arctic Oscillation and ozone loss. *Journal of Geophysical Research* **125**: e2020JD033271. https://doi.org/10.1029/2020JD033271.

Matejka, T, Srivastava, RC. 1991. An improved version of the extended velocity-azimuth display analysis of single-Doppler radar data. *Journal of Atmospheric and Oceanic Technology* **8**: 453–466.

Matrosov, SY. 2007. Modeling backscatter properties of snowfall at millimeter wavelengths. *Journal of Atmospheric Science* **64**: 1727–1736, https://doi.org/10.1175/jas3904.1.

Maturilli, M, Kayser, M. 2017. Arctic warming, moisture increase and circulation changes observed in the Ny-Ålesund homogenized radiosonde record. *Theoretical and Applied Climatology* **130**: 1–17, https://doi.org/ 10.1007/s00704-016-1864-0.

Maturilli, M, Holdridge, DJ, Dahlke, S, Graeser, J, Sommerfeld, A, Jaiser, R, Deckelmann, H, Schulz, A. 2021. Initial radiosonde data from 2019-10 to 2020-09 during project MOSAiC. Alfred Wegener Institute, Helmholtz Centre for Polar and Marine Research, Bremerhaven, PANGAEA, https://doi.org/10.1594/PANGAEA.928656.

Mellat Ardakani, M, Bailey, H, Mustonen, KR, Marttila, H., Klein, ES, Gribanov, K, Bret-Harte, MS, Chupakov, AV, Divine DV, Else, B, and Filippov, I. 2021. Hydroclimatic controls on the isotopic ($\delta^{18}O$, $\delta^{2}H$, d-excess) traits of pan-Arctic summer rainfall events. *Frontiers in Earth Sciences* **9**: 367, https://doi.org/10.3389/feart.2021.651731.

Middlemas, EA, Kay, JA, Medeiros, BM, Maroon, EA. 2020. Quantifying the influences of cloud radiative feedbacks on Arctic surface warming using cloud locking in an Earth system model. *Geophysical Research Letters* **47**, https://doi.org/10.1029/2020GL089207.

Morris, V, Ermold, B. 2019. Ceilometer (CEIL). Atmospheric Radiation Measurement (ARM) user facility. https://doi.org/10.5439/1181954.

Morrison, AL, Kay, JE, Chepfer, H, Guzman, R, Yettella, V. 2018. Isolating the liquid cloud response to recent Arctic sea ice variability using spaceborne lidar observations. *Journal of Geophysical Research* **123**: 473–490, https://doi.org/10.1002/2017JD027248.

MOSAiC. 2016. MOSAiC – Multidisciplinary drifting Observatory for the Study of Arctic Climate Science Plan. Available online: https://mosaic-expedition.org/wp-content/uploads/2020/12/mosaic_scienceplan.pdf

Nansen, F. 1897. Farthest North, Volumes I and II. New York: Harper & Brothers Publishers.

Nicolaus, M, Perovich, DK, Spreen, G, Granskog, MA, v. Albedyll, L, Anhaus, P, Angelopoulos, M, Arndt, A, Belter, HJ, Bessonov, V, Birnbaum, G, Brauchle, JB, Calmer, R, Cardellach, E, Cheng, B, Clemens-Sewall, D, Dadic, R, Damm, E, de Boer, G, Demir, O, Divine, D, Fong, A, Fons, S, Fuchs, N, Gabarró, C, Gerland, S, Gradinger, R, Goessling, HF, Haapala, J, Haas, C, Hamilton, J, Hannula, H-R, Hendricks, S, Herber, A, Heuzé, C, Hoppmann, M, Høyland, KV, Huntemann, M, Hutchings, JK, Hwang, B, Itkin, P, Jaggi, M, Jutila, A, Kaleschke, L, Katlein, C, Kolabutin, N, Krampe, D, Kristensen, SS, Krumpen, T, Kurtz, N, Lampert, A, Lange, BA, Lei, R, Light, B, Linhardt, F, Liston, G, Loose, B, Macfarlane, AR, Mahmud, M, Matero, IO, Maus, S, Morgenstern, A, Naderpour, R, Nandan, V, Niubom, A, Oggier, M, Oppelt, N, Pätzold, F, Petrovsky, T, Pirazzini, R, Polashenski, C, Rabe, B, Raphael, IA, Regnery, J, Rex, M, Ricker, R, Riemann-Campe, K, Rinke, A, Rohde, J, Salganik, E, Scharien, RK, Schiller, M, Schneebeli, M, Semmling, M, Sheikin, I, Shimanchuk, E, Shupe, MD, Smith, MM, Smolyanitsky, V, Sokolov, V, Sokolova, J, Stanton, TP, Stroeve, J, Tavri, A, Thielke, L, Timofeeva, A, Tonboe, RT, Tsamados, M, Wagner, DN, Watkins, D, Webster, M, Wendisch, M. 2022. Overview of the MOSAiC Expedition – Snow and Sea Ice. *Elementa: Science of the Anthropocene* (in press).

Nixdorf, U, Dethloff, K, Rex, M, Shupe, M, Sommerfeld, A, Perovich, DK, Nicolaus, M, Heuze, C, Rabe, B, Loose, B, Damm, E, Gradinger, R, Fong, A, Maslowski, W, Rinke, A, Kwok, R, Spreen, G, Wendisch, m, Herber, A, Hirsekorn, M, Mohaupt, V, Frickenhaus, S, Immerz, A, Weiss-Tuider, K, Koenig, B, Mengedoht, D, Regnery, J, Gerchow, P, Ransby, D, Krumpen, T, Morgenstern, A, Haas, C, Kanzow, T, Rack, F, Saitzev, V, Sokolov, V, Makarov, A, Schwarze, S, Wunderlick, T, Wurr, K, Boetius, A. 2021. MOSAiC extended acknowledgement. *Zenodo*. https://doi.org/10.5281/zenodo.5541624.

O'Connor, EJ, Hogan, RJ, Illingworth, AJ. 2005. Retrieving stratocumulus drizzle parameters using Doppler radar and lidar. *Journal of Applied Meteorology* **44**: 14–27, https://doi.org/10.1175/JAM-2181.1.

O'Connor, EJ, Illingworth, AJ, Brooks, IM, Westbrook, CD, Hogan, RJ, Davis, F, Brooks, BJ. 2010. A method for estimating the turbulent kinetic energy dissipation rate from a vertically pointing Doppler lidar, and independent evaluation from balloon-borne in situ measurements. *Journal of Atmospheric and Oceanic Technology* **27**: 1652–1664. https://doi.org/10.1175/2010JTECHA1455.1

Overland, J, Dunlea, E, Box, JE, Corell, R, Forsius, M, Kattsov, V, Olsen, MS, Pawlak, J, Reiersen, LO, Wang, M. 2019. The urgency of Arctic change. *Polar Science* **21**: 6–13, https://doi.org/10.1016/j.polar.2018.11.008.

Perovich, DK, Andreas, EL, Curry, JA, Eiken, H, Fairall, CW, Grenfell, TC, Guest, PS, Intrieri, J, Kadko, D, Lindsay, RW, McPhee, MG, Morison, J, Moritz, RE, Paulson, CA, Pegau, WS, Persson, POG, Pinkel, R, Richter-Menge, JA, Stanton, T, Stern, H, Sturm, M, Tucker III, WB, Uttal, T. 1999. Year on ice gives climate insights. *Eos Transactions* **80**: 485–486, https://doi.org/10.1029/EO080i041p00481-01.

Philipp, D, Stengel, M, Ahrens, B. 2020. Analyzing the Arctic feedback mechanism between sea ice and low-level clouds using 34 years of satellite observations. *Journal of Climate* **33**: 7479–7501, https://doi.org/10.1175/JCLI-D-19-0895.1.

Pisso, I, Sollum, E, Grythe, H, Kristiansen, NI, Cassiani, M, Eckhardt, S, Arnold, D, Morton, D, Thompson, RL, Groot Zwaaftink, CD, Evangeliou, N, Sodemann, H, Haimberger, L, Henne, S, Brunner, D, Burkhart, JF, Fouilloux, A, Brioude, J, Philipp, A, Seibert, P, Stohl, A. 2019. The Lagrangian particle dispersion model FLEXPART version 10.4. *Geoscientific Model Development* **12**: 4955–4997, https://doi.org/10.5194/gmd-12-4955-2019.

Pithan, F, Svensson, G, Caballero, R, Chechin, D, Cronic, TW, Ekman, A, Neggers, R, Shupe, MD, Solomon, A, Tjernstrom, M, Wendisch, M. 2018. Role of air-mass transformations in exchange between the Arctic and mid-latitudes. *Nature Geosciences* **11**: 805–812, https://doi.org/ 10.1038/s41561-018-0234-1.

Polarstern: Alfred-Wegener-Institut Helmholz-Zentrum für Polar- und Meeresforschung. 2017. Polar Research and Supply Vessel POLARSTERN Operated by the Alfred-Wegener-Institute. *Journal of Large-scale Research Facilities* **3**: A119. https://doi.org/10.17815/jlsrf-3-163.

Rabe, B, Heuzé, C, Regnery, J, Aksenov, Y, Allerholt, J, Athanase, M, Bai, Y, Basque, C, Bauch, D, Baumann, TM, Chen, D, Cole, ST, Craw, L, Davies, A, Damm, E, Dethloff, K, Divine, DV, Doglioni, F, Ebert, F, Fang, Y-C, Fer, I, Fong, AA, Gradinger, R, Granskog, MA, Groupner, R, Haas, C, He, H, He, Y, Hoppmann, M, Janout, M, Kadko, D, Kanzow, T, Karam, S, Kawaguchi, Y, Koenig, Z, Kong, B, Krishfield, RA, Kuhlmey, D, Kuznetsov, I, Lan, M, Lei, R, Li, T, Torres-Valdes, S, Lin, L, Lin, L, Liu, H, Liu, N, Loose, B, Ma, X, MacKay, R, Mallet, M, Mallett, RDC, Maslowski, W, Mertens, C, Mohrholz, V, Muilwijk, M, Nicolaus, M, O'Brien, JK, Perovich, D, Ren, J, Rex, M, Ribeiro, N, Rinke, A, Schaffer, J, Schuffenhauer, I, Schulz, K, Shupe, MD, Shaw, W, Sommerfeld, A, Spreen, G, Stanton, T, Stephens, M, Su, J, Sukhikh, N, Sundfjord, A, Tippenhauer, S, Toole, JM, Vredenborg, M, Walter, M, Wang, H, Wang, L, Wang,

Y, Wendisch, M, Zhao, J, Zhou, M, Zhu, J. 2022. Overview of the MOSAiC Expedition – Physical Oceanography. *Elementa: Science of the Anthropocene* (accepted with minor revision).

Rinke, A, Cassano, JJ, Cassano, EN, Jaiser, R, Handorf, D. 2021. Meteorological conditions during the MOSAiC expedition: Normal or anomalous? *Elementa: Science of the Anthropocene* **9**(1): 00023, https://doi.org/10.1525/elementa.2021.00023.

Riihimaki, L. 2021. Radiation instruments on Ice (ICERADRIIHIMAKI). Atmospheric Radiation Measurement (ARM) user facility. https://doi.org/10.5439/1608608.

Roiger, A, Thomas, J-L, Schlager, H, Law, KS, Kim, J, Schafler, A, Weinzierl, B, Dahlkotter, F, Krisch, I, Marelle, L, Minikin, A, Raut, J-C, Reiter, A, Rose, M, Scheibe, M., Stock, P, Baumann, R, Bouarar, I, Clerbaux, C, George, M, Onishi, T, Flemming, J. 2015. Quantifying emergin local anthropogenic emissions in the Arctic Region: The ACCESS Aircraft Campaign Experiment. *Bulletin of the American Meteorological* Society **96**: 441–460, https://doi.org/10.1175/BAMS-D-13-00169.1.

Romanowsky, E, Handorf, D, Jaiser, R, Wohltmann, I, Dorn, W, Ukita, J, Cohen, J, Dethloff, K, Rex, M. 2019. The role of stratospheric ozone for Arctic-midlatitude linkages. *Scientific Reports* **9**: 7962, http://doi.org/10.1038/s41598-019-43823-1.

Sandu, I, Beljaars, A, Bechtold, P, Mauritsen, T, Balsamo, G. 2013. Why is it so difficult to represent stably stratified conditions in numerical weather prediction (NWP) models? *Journal of Advanced Modeling of the Earth System* **5**: 117–133, https://doi.org/10.1002/jame.20013.

Sato, K, Inoue, J, Yamazaki, A, Kim, JH, Maturilli, M, Dethloff, K, Hudson, SR, Granskog, M. 2017. Improved forecasts of winter weather extremes over midlatitudes with extra Arctic observations. *Journal of Geophysical Research - Oceans* **122**: 775–787, https://doi.org/10.1002/2016JC012197.

Sato, K, Inoue, J, Yamazaki, A, Kim, JH, Makshtas, A, Kustov, V, Maturilli, M, Dethloff, K. 2018. Impact on predictability of tropical and mid-latitude cyclones by extra Arctic observations. *Nature Scientific Reports* **8**: 12104, https://doi.org/10.1038/s41598-018-30594-4.

Schmale, J, and Coauthors. 2018. Long-term cloud condensation nuclei number concentration, particle number size distribution and chemical composition measurements at regionally representative observatories. *Atmospheric Chemistry and Physics* **18**: 2853–2881, https://doi.org/10.5194/acp-18-2853-2018.

Schmale, J, Zieger, P, Ekman, AML. 2021. Aerosols in current and future Arctic climate. *Nature Climate Change* **11**: 95–105, https://doi.org/10.1038/s41558-020-00969-5.

Schmeisser, L, Backmann, J, Ogren, JA, Andrews, E, Asmi, E, Starkweather, S, Uttal, T, Fiebig, M, Sharma, S, Eleftheriadis, K, Vratolis S, Bergin, M, Tunved, P, Jefferson, A. 2018. Seasonality of aerosol optical properties in the Arctic. *Atmospheric Chemistry and Physics* **18**: 11599–11622, https://doi.org/10.5194/acp-18-11599-2018.

Screen, JA, Bracegirdle, TJ, Simmonds, I. 2018. Polar climate change as manifest in atmospheric circulation. *Current Climate Change Reports* **4**: 383–395, https://doi.org/ 10.1007/s40641-018-0111-4.

Sedlar, J, Tjernstrom, M, Rinke, A, Orr, A, Cassano, J, Fettweis, X, Heinemann, G, Seefeldt, M, Solomon, A, Matthes, H, Phillips, T, Webster, S. 2020. Confronting Arctic troposphere, clouds, and surface energy budget representations in Regional Climate Models with observations. *Journal of Geophysical Research* **125**: e2019JD031783, https://doi.org/10.1029/2019JD031783.

Serreze, MC, Barry, RG. 2011. Processes and impacts of Arctic amplification: A research synthesis. *Global and Planetary Change* **77**: 85–96, https://doi.org/ 10.1016/j.gloplacha.2011.03.004.

Shupe, MD, Intrieri, JM. 2004. Cloud radiative forcing of the Arctic surface: The influence of cloud properties, surface albedo, and solar zenith angle. *Journal of Climate* **17**: 616–628, https://doi.org/10.1175/1520-0442(2004)017<0616:CRFOTA>2.0.CO;2.

Shupe, MD, Kollias, P, Persson, POG, McFarquhar, GM. 2008. Vertical motions in Arctic mixed-phase stratiform clouds. *Journal of Atmospheric Science* **65**: 1304–1322, https://doi.org/10.1175/2007JAS2479.1.

Shupe, MD, Walden, VP, Eloranta, E, Uttal, T, Campbell, JR, Starkweather, SM, Shiobara, M. 2011. Clouds at Arctic Atmospheric Observatories, Part I: Occurrence and macrophysical properties. *Journal of Applied Meteorology and Climatology* **50**: 626–644, https://doi.org/ 10.1175/2010JAMC2467.1.

Shupe, MD, Turner, DD, Zwink, A, Thieman, MM, Mlawer, EJ, Shippert, T. 2015. Deriving Arctic cloud microphysics at Barrow, Alaska: Algorithms, results, and radiative closure. *Journal of Applied Meteorology and Climatology* **54**: 1675–1689, https://doi.org/10.1175/JAMC-D-15-0054.1.

Sivaraman, C, Flynn, D, Riihimaki, L, Comstock, J. 2019. Cloud mask from Micropulse Lidar (30SMPLCMASK1ZWANG). Atmospheric Radiation Measurement (ARM) user facility. https://doi.org/10.5439/1508389.

Stapf, J, Ehrlich, A, Jäkel, E, Lüpkes, C, Wendisch, M. 2020. Reassessment of shortwave surface cloud radiative forcing in the Arctic: consideration of surface-albedo–cloud interactions. *Atmospheric Chemistry and Physics* **20**: 9895–9914, https://doi.org/10.5194/acp-20-9895-2020.

Stevens, RG, Loewe, K, Dearden, C, Dimitrelos, A, Possner, A, Eirund, GK, Raatikainen, T, Hill, AA, Shipway, BJ, Wilkinson, J, Romakkaniemi, S, Tonttila, J, Laaksonen, A, Korhonen, H, Connolly, P, Lohmann, U, Hoose, C, Ekman, AML, Carslaw, KS, Field, PR. 2018. A model intercomparison of CCN-limited tenuous clouds in the high Arctic. *Atmospheric Chemistry and Physics* **18**: 11041–11071, https://doi.org/10.5194/acp-18-11041-2018.

Stohl, A. 2006. Characteristics of atmospheric transport into the Arctic troposphere. *Journal of Geophysical Research* **111**: D11306, https://doi.org/10.1029/2005JD006888.

Stohl, A, Forster, C, Eckhardt, S, Spichtinger, N, Huntrieser, H, Heland, J, Schlager, H, Wilhelm, S, Arnold, F, Cooper, O. 2003. A backward modeling study of intercontinental pollution transport using aircraft measurements. *Journal of Geophysical Research* **108**: 4370, https://doi.org/10.1029/2002JD002862.

Tetzlaff, A, Lüpkes, C, Hartmann, J. 2015. Aircraft-based observations of atmospheric boundary-layer modification over Arctic leads. *Quarterly Journal of the Royal Meteorological Society* **141**: 2839–2856, https://doi.org/10.1002/qj.2568.

Thomas, CK, Kennedy, AM, Selker, JS, Moretti, A, Schroth, MH, Smoot, AR, Tufillaro, NB, Zeeman, MJ. 2012. High-resolution fibre-optic temperature sensing: A new tool to study the two-dimensional structure of atmospheric surface layer flow. *Boundary-Layer Meteorology* **142**: 177–192. https://doi.org/10.1007/s10546-011-9672-7.

Tjernström, M, Leck, C, Birch, CE, Bottenheim, JW, Brooks, BJ, Brooks, IM, Bäcklin, L, Chang, RY-W, de Leeuw, G, Di Liberto, L, de la Rosa, S, Granath, E, Graus, M, Hansel, A, Heintzenberg, J, Held, A, Hind, A, Johnston, P, Knulst, J, Martin, M, Matrai, PA, Mauritsen, T, Müller, M, Norris, SJ, Orellana, MV, Orsini, DA, Paatero, J, Persson, POG, Gau, Q, Rauschenberg, C, Ristovski, Z, Sedlar, J, Shupe, MD, Sierau, B, Sirevaag, A, Sjogren, S, Stetzer, O, Swietlicki, E, Szczodrak, M, Vaattovaara, P, Wahlberg, N, Westberg, M, Wheeler, CR,. 2014. The Arctic Summer Cloud Ocean Study (ASCOS): Overview and experimental design. *Atmospheric Chemistry and Physics* **14**: 2823–2869, https://doi.org/10.5194/acp-14-2823-2014.

Tjernström, M, Svensson, G, Magnusson, L, Brooks, IM, Prytherch, J., Vüllers, J, Young, G. 2021. Central Arctic weather forecasting: Confronting the ECMWF IFS with observations from the Arctic Ocean 2018 expedition. *Quarterly Journal of the Royal Meteorological Society* **147**: 1278–1299, https://doi.org/10.1002/qj.3971.

Urrego-Blango, JR, Hunke, EC, Urban, N. 2019. Emergent relationships among sea ice, longwave radiation, and the Beaufort High circulation exposed through parameter uncertainty analysis. *Journal of Geophysical Research* **124**: 9572–9589, https://doi.org/10.1029/2019JC014979.

Uttal, T, Starkweather, S, Drummond, JR, Vihma, T, Makshtas, AP, Darby, LS, Burkhart, JF, Cox, CJ, Schmeisser, LN, Haiden, T, Maturilli, M, Shupe, MD, de Boer, G, Saha, A, Grachev, AA, Crepinsek, SM, Bruhwiler, L, Goodison, B, McArther, B, Walden, VP, Dlugokencky, EJ, Persson POG, Lesins, G, Laurila, T, Ogren, JA, Stone, R, Long, CN, Sharma, S, Massling, A, Turner, DD< Stanitski, DM, Asmi, E, Aurela, M, Skov, H, Eleftheriadis, K, Virkkula, A, Platt, A, Forland, EJ, Iijima, Y, Nielsen, IE, Bergin, MH, Candlish, L, Zimov, NS, Zimov, SA, O'Neill, NT, Fogal, PF, Kivi, R, Konopleva-Akish, EA, Verlinde, J, Kustov, VY, Vasel, B, Ivakhov, VM, Viisanen, Y, Intrieri, JM. 2016. International Arctic Systems for Observing the Atmosphere (IASOA): An International Polar Year legacy consortium. *Bulletin of the American Meteorological Society* **97**: 1033–1056, https://doi.org/10.1175/BAMS-D-14-00145.1.

Verlinde, J, Harrington, JY, McFarquhar, GM, Yannuzzi, VT, Avramov, A, Greenberg, S, Johnson, N, Zhang, G, Poellot, MR, Mather, JH, Turner, DD, Eloranta, EW, Zak, BD, Prenni, AJ, Daniel, JS, Kok, GL, Tobin, DC, Holz, R, Sassen, K, Spangenberg, D, Minnis, P, Tooman, TP, Ivey, MD, Richardson, SJ, Bahrmann, CP, Shupe, M, DeMott, PJ, Heymsfield, AJ, Schofield, R. 2007. The Mixed-Phase Arctic Cloud Experiment (M-PACE). *Bulletin of the American Meteorological Society* **88**: 205–220, https://doi.org/10.1175/BAMS-88-2-205.

Verlinde, J, Zak, BD, Shupe, MD, Ivey MD, Stamnes, K. 2016. The North Slope of Alaska (NSA) sites. The Atmospheric Radiation Measurement Program: The First 20 Years. *Meteorological Monograph*, American Meteorological Society **57**: 8.1–8.13. https://doi.org/10.1175/AMSMONOGRAPHS-D-15-0023.1.

Vüllers, J, Achtert, P, Brooks, IM, Tjernström, M, Prytherch, J, Burzik, A, Neely III, R. 2020. Meteorological and cloud conditions during the Arctic Ocean 2018 expedition. *Atmospheric Chemistry and Physics* **21**: 2890314, https://doi.org/10.5194/acp-21-289-2021.

Wagner, D, Shupe, MD, Persson, OG, Uttal, T, Frey, MM, Kirchgaessner, A, Schneebeli, M, Jaggi, M, Macfarlane, AR, Itkin, P, Arndt, S, Hendricks, S, Krampe, D, Ricker, R, Regnery, J, Kolabutin, N, Shimanshuck, E, Oggier, M, Raphael, I, Lehning, M. 2021. Snowfall and snow accumulation processes during the MOSAiC winter and spring season. *Cryosphere Discussions*, under review. https://doi.org/10.5194/tc-2021-126.

Walter, B, Overland, J. 1991. Aircraft observations of the mean and turbulent structure of the atmospheric boundary layer during spring the central Arctic. *Journal of Geophysical Research* **96**: 4663–4673, https://doi.org/10.1029/90JC02263.

Wendisch, M, Macke, A, Ehrlich, A, Lupkes, C, Mech, M, Chechin, D, Barientos, C, Bozem, H, Brueckner, M, Clemen, HC, Crewell, S, Donth, T, Dupuy, R, Ebell, K, Egerer, U, Engelmann, R, Engler, C, Eppers, O, Gehrmeann, M, Gong, X, Gottschalk, M, Bourbeyre, C, Griesche, H, Hartmann, J, Hartmann, M, Herber, A, Herrmann, H, Heygster, G, Hoor, P, Jafariserajehlou, S, Jakel, E, Jarvinen, E, Jourdan, O, Kastner, U, Kecorius, S, Knudsen, EM, Kollner, F, Kretzschmar, J, Lelli, L, Leroy, D, Maturilli, M, Mei, L, Mertes, S, Mioche, G, Neuber, R, Nicolaus, M, Nomokonova, T, Notholt, J, Palm, M, Van Pinxteren, M, Quass, J, Richter, P, Ruiz-Donoso, E, Schafer, M, Schmieder, K, Schnaiter, M, Schneider, J, Schwarzenbock, A, Siefert, P, Shupe, MD, Siebert, H, Spreen, G, Stapf, J, Stratmann, F, Vogl, T, Welti, A, Wex, H, Wiedensohler, A, Zanatta, M, Zeppenfeld, S. 2019. The Arctic Cloud Puzzle: Using ACLOUD/PASCAL multi-platform observations to unravel the role of clouds and aerosol particles in Arctic Amplification. *Bulletin of the American Meteorological Society* **100**: 841–871, https://doi.org/10.1175/BAMS-D-18-0072.1.

Wesche, C, Steinhage, D, Nixdorf, U. 2016. Polar aircraft Polar5 and Polar6 operated by the Alfred-Wegener-Institute. *Journal of Large-scale Research Facilities* **2**: A87, https://doi.org/10.17815/jlsrf-2-153.

Wohltmann, I, von der Gathen, P, Lehmann, R, Maturilli, M, Deckelmann, H, Manney, GL, Davies, J, Tarasick, D, Jepsen, N, Kivi, R, Lyall, N, Rex, M. 2020. Near-complete local reduction of Arctic stratospheric ozone by severe chemical loss in spring 2020. *Geophysical Research Letters* **47**: e2020GL089547. https://doi.org/10.1029/2020GL089547.

Woods, C, Caballero, R. 2016. The role of moist intrusions in winter Arctic warming and sea ice decline. *Journal of Climate* **29**: 4473–4485, https://doi.org/10.1175/JCLI-D-15-0773.1.

Woods, C, Caballero, R, Svensson, G. 2017. Representation of Arctic moist intrusions in CMPI5 models and implications for winter climate biases. *Journal of Climate* **30**: 4083–4102, https://doi.org/10.1175/JCLI-D-16-0710.1.

Contributions

Contributed to conception and design: SA, BB, CB, GdB, IMB, DCh, JC, SC, ED, KD, AAF, MMF, RG, GH, DHe, AH, CH, BL, AM, WM, MMat, MN, DP, POGP, HP, BR, MRe, JS, MDS, GS, ASom, PvdG, MWen

Contributed to acquisition/production of data: DA, HA, SA, LB, IB, JB, BB, MB, ZB, IMB, RC, JC, VC, DCh, DCo, CC, JC, SD, HD, AE, JE, RE, MMF, MG, JG, VG, HG, SG, JHa, AH, JHo, TH, DHo, JHue, JHut, RJ, TJ, OJ, GJ, WK, AK, MKl, MKr, TK, AL, BL, TL, DL, ML, CL, MMaa, CM, MMat, MMe, MMo, PO, JO, FP, POGP, CP, RP, KPo, HP, KPr, AP, LQ, MRa, MRe, TSa, JS, ASc, MDS, HS, TSi, ASol, ASom, ASt, JU, TU, JV, CV, PvdG, BW, JMW, MWen, MWer, ZQX, FY

Contributed to analysis and interpretation of data: HA, SA, BB, SB, GdB, MB, ZB, IMB, RC, CC, JC, SD, KD, MD, KE, RE, MMF, LG, GH, JI, H-WJ, GJ, MKl, ML, MMaa, POGP, AR, JS, ASc, MDS, HS, ASol, GS, MWen, MWer

Drafted and/or revised the manuscript: All authors

Approved and submitted manuscript: All authors

Acknowledgements

This work was carried out, and data used in this manuscript were produced, as part of the international Multidisciplinary drifting Observatory for the Study of Arctic Climate (MOSAiC) with the tag MOSAiC20192020. We thank all persons involved in the expedition of the Research Vessel *Polarstern* during MOSAiC in 2019–2020 (AWI_PS122_00) as listed in Nixdorf et al. (2021). A subset of data was obtained from the Atmospheric Radiation Measurement (ARM) User Facility, a U.S. Department of Energy (DOE) Office of Science User Facility Managed by the Biological and Environmental Research Program. Instrumentation from the University of Leeds was provided by the Atmospheric Measurement Observations Facility (AMOF) or the UK National Centre for Atmospheric Science (NCAS). J.S. holds the Ingvar Kamprad chair for extreme environments research. We thank the anonymous reviewers; their constructive comments have helped to improve the manuscript.

Funding information

This work was funded by

- German Federal Ministry for Education and Research (BMBF) through financing the Alfred-Wegener-Institut Helmholtz Zentrum für Polar- und Meeresforschung (AWI) and the Polarstern expedition PS122 under grant N-2014-H-060_Dethloff
- AWI through its projects: AWI_ATMO, AWI_ICE, AWI_SNOW
- US National Science Foundation Office of Polar Programs (OPP-1724551, OPP-1805569, OPP-1807496, OPP-1914781, OPP-1852614, OPP-1753423, OPP-1753418, OPP-1753408)

- US Department of Energy – Office of Science Atmospheric Radiation Measurement and Atmospheric System Research Programs (DE-SC0019251, DE-SC0021341, DE-SC0019745, DE-SC0019172, DE-AC05-76RL01830)
- US National Oceanic and Atmospheric Administration Physical Sciences Laboratory, Global Monitoring Laboratory, and Global Ocean Monitoring and Observing Program
- Deutsche Forschungsgemeinschaft, (268020496 – TRR 172), within the Transregional Collaborative Research Center "Arctic Amplification: Climate Relevant Atmospheric and Surface Processes, and Feedback Mechanisms (AC)[3]
- Deutsche Forschungsgemeinschaft (LA 2907/11-1, SA 1884/6-1)
- European Regional Development Fund (ZW 6-85014470)
- European Union's Horizon 2020 research and innovation program projects ARICE (grant 730965), INTAROS (grant 727890), INTERACT Program-Pan Arctic Precipitation Isotope Network
- European Commission (689443)
- Swiss National Science Foundation (grant 200021_188478) and the Swiss Polar Institute
- UK Natural Environment Research Council (grant NE/S002472/1, NE/S00257X/1)
- French National Centre for Scientific Research (CNRS)
- Chinese Arctic and Antarctic Administration and National Natural Science Foundation of China (41941014)
- Japan Society for the Promotion of Science (JP18H03745, JP18KK0292)
- Academy of Finland (grant 318930, 333397, 337549, 329274, 307537), and University of Helsinki (752 84 128)
- University of the Arctic Research Chairship (U.Arctic and the University of Oulu)

Competing interests

All authors declare that they have no competing interests. ED, RG, CH, WM, MN, MRe, AR, MDS and GS are all guest editors for the *Elementa* Special Feature on MOSAiC but were not involved in the editorial or review process for this manuscript. DHe is editor-in-chief of the *Elementa* Atmospheric Science Domain, but was not involved in the editorial or review process of this manuscript.

Data accessibility statement

All data plotted in this paper are extracted from much larger data sets that must be made publicly available prior to January 1, 2023, on the MOSAiC archives, including PANGAEA (https://www.pangaea.de/), the Department of Energy Atmospheric Radiation Measurement (ARM) Program data archive (https://adc.arm.gov/discovery/), the National Science Foundation's Arctic Data Center (http://arcticdata.io), and elsewhere. Prior to public release, direct access to data included in this paper can be granted by contacting the relevant contact(s) given for each measurement in Appendix B. The following data used in this manuscript are currently publicly available:

- Near-surface meteorology and surface energy flux measurements from the University of Colorado/NOAA surface flux team are available through the Arctic Data Center (Cox et al., 2021a; Cox et al., 2021b).

- All data used in this paper from the ARM Program are available at the ARM Archive (https://adc.arm.gov/discovery), including:
    - Cloud occurrence data (Morris and Ermold, 2019).
    - Radiation data (Riihimaki, 2021).
    - Cloud radar (Johnson and Scott, 2019).
    - Micropulse lidar data (Sivaraman et al., 2019).
    - Nephelometer data (Koontz et al., 2019).
    - Cloud condensation nucleus data (Koontz and Senum, 2019).
    - Atmospheric emitted radiance interferometer data (Gero et al., 2019).
    - Ice-nucleating particle data (Creamean, 2020).
- Radiosonde data from the Alfred Wegener Institute, in collaboration with the ARM Program, are available from the PANGAEA archive (Maturilli et al. 2021).
- UAS data from the University of Colorado and NOAA Physical Sciences Laboratory are available from the Arctic Data Center (Jozef et al., 2021).
- Trajectory analysis was derived from FLEXPART model simulations performed by the FLEXPART group at the University of Vienna, available via https://img.univie.ac.at/webdata/mosaic.
- The ERA5 Reanalysis data are available from the European Centre for Medium-Range Weather Forecasts at: https://www.ecmwf.int/en/forecasts/datasets/reanalysis-datasets/era5

Figure titles and legends

Figure 1. Atmospheric processes over the Central Arctic.
Depicted are the primary zones and processes examined by the atmosphere team during the year-long MOSAiC expedition that began in September 2019.

Figure 2. Expedition track distinguished by leg.
Periods of passive drift by *Polarstern* (solid) and periods of transit when the vessel was underway (dotted) are distinguished. The inclusive dates for each of the five, color-coded expedition legs are given in the legend, with the second set of dates in parentheses being the dates spent in passive drift with an ice floe. The approximate sea ice edge at the annual maximum (Mar 5, 2020) and minimum (Sep 15, 2020) is also provided.

Figure 3. *Polarstern* during July 2020, with key observing locations for the ATMOS team highlighted.
Bow containers included instruments provided by institutions TROPOS, BAS, Swiss and ARM (abbreviations defined in Appendix A). Photo credit: Lianna Nixon.

Figure 4. Main installations in the MOSAiC Central Observatory on November 15, 2019.
This configuration of the Central Observatory is provided as a conceptual example; while it accurately represents the initial installation during Leg 1, ice dynamics and logistics dictated many changes over the course of the expedition. BGC refers to Biogeochemistry; ROV, to remotely operated vehicle.

Figure 5. Temporal coverage of atmospheric state measurements in different categories.
The different colors represent the following: red, onboard *Polarstern* while at MOSAiC ice floe; orange, onboard *Polarstern* while underway; blue, on sea ice in the Central Observatory; green, on sea ice in the Distributed Network. Solid bars are continuous measurements with minimal gaps. Hatched bars are intermittent or periodic measurements. The time spans from late September 2019 through early October 2020.

Figure 6. Temporal coverage of cloud and precipitation measurements in different categories.
The different colors represent the following: red, onboard *Polarstern* while at MOSAiC ice floe; orange, onboard *Polarstern* while underway; blue, on sea ice in the Central Observatory. Solid bars are continuous measurements with minimal gaps. Hatched bars are intermittent or periodic measurements. The time spans from late September 2019 through early October 2020.

Figure 7. Temporal coverage of gas and aerosol measurements in different categories.
The different colors represent the following: red, onboard *Polarstern* while at MOSAiC ice floe; orange, onboard *Polarstern* while underway; blue, on sea ice in the Central Observatory. Solid bars are continuous measurements with minimal gaps. Hatched bars are intermittent or periodic measurements. The time spans from late September 2019 through early October 2020.

Figure 8. Temporal coverage of energy budget measurements in different categories.

The different colors represent the following: red, onboard *Polarstern* while at MOSAiC ice floe; orange, onboard *Polarstern* while underway; blue, on sea ice in the Central Observatory; green, on sea ice in the Distributed Network. Solid bars are continuous measurements with minimal gaps. Hatched bars are intermittent or periodic measurements. The time spans from late September 2019 through early October 2020.

Figure 9. *Polar 5* flight paths for flights conducted during the ACA program out of Longyearbyen (LYR).
Flight dates are given as year-month-day. The sea ice concentration is shaded according to the colorbar.

Figure 10. Surface-based atmospheric observations during the MOSAiC year.
Daily-averaged (a) atmospheric sea-level pressure, with individual cyclone events identified (black squares); (b) 2-m temperature (red) and a 7-day running mean 2-m temperature (orange); (c) 2-m relative humidity with respect to liquid water (red) and ice water (orange) and (d) 10-m wind speed all measured from the met tower at Met City; (e) daily cloud occurrence fraction from a ceilometer onboard *Polarstern* (with gaps when *Polarstern* left the MOSAiC ice floes); and (f) downward shortwave radiation measured at Met City. While Met City was not operational during mid-May to mid-June, most measurements were provided by an Atmospheric Surface Flux Station that remained at the MOSAiC ice floe. The 5^{th}–95^{th} percentile range of ERA5 results at the moving MOSAiC position is given (gray shading) in (a), (b), and (d) based on Rinke et al. (2021). The MOSAiC Leg periods are shown along the top, and a general characterization of seasons, as described in the text, is provided with alternating gray and white background shading.

Figure 11. Trajectory analysis providing information on air mass origins.
A time series of FLEXPART model footprint emission sensitivity for 30-day back-trajectories of a passive air tracer and integrated over the different regions shown in the map on the right. The different degrees of blue-to-white shading over the Arctic Ocean indicate the yearly evolution of sea ice cover (30, 50, and 99% sea ice concentration). The thickness of each colored layer in the time series represents the contribution of the corresponding region to the total FES. The quantity in the time series is expressed in units of s m^{-1} such that, when multiplied by the emission flux of a species over a region (given in units of kg m^{-2} s^{-1}), it gives an estimate of the relative contribution of each region to the total concentration (in kg m^{-3}) observed at *Polarstern*.

Figure 12. Sea-level pressure and 850 hPa wind vectors averaged over February 5–7.
Data are derived from the ERA5 reanalysis. Sea-level pressure is given as colors in hPa. A 10 m s^{-1} wind vector is given in the legend, and plotted wind vectors scale linearly.

Figure 13. Atmospheric physical state measurements for the February 5–7 case.
Temperature profiles from radiosondes for heights (a) above and (b) below 5 km; (c) relative humidity profiles derived from the PollyXT lidar; (d) wind direction profiles derived from radiosondes; (e) 2-m temperature (black) and 10-m wind speed (red) derived from the Met City tower, and 2-km wind speed from radiosondes (orange); (f) integrated water vapor (IWV, black) derived from the HATPRO and surface pressure (red) measured at the Met City tower; and (g) $\delta^{18}O$ (black) and d-excess (red) observed by a water vapor analyzer.

Figure 14. Cloud and precipitation measurements for the February 5–7 case.
Time-height profiles of (a) radar reflectivity from the KAZR, (b) log of the lidar backscatter from PollyXT, (c) and lidar depolarization ratio from the Micropulse lidar; and time series of (d) liquid water path derived from HATPRO, (e) ice particle size distribution from a snow particle counter on the Met City tower, and (f) snow particle counts (black, left axis) and average particle maximum dimension (red, right axis) observed by the Video In Situ Snowfall Sensor at Met City.

Figure 15. Gas and aerosol measurements for the February 5–7 case.
Gas concentrations of (a) CH_4 (black) and CO_2 (red), (b) O_3 (black) and Hg (red), and (c) sulfuric acid (SA, black), methanesulfonic acid (MSA, red), and iodic acid (IA, orange), all on the left axis, and SO_2 (blue) on the right axis. Aerosol number size distributions measured by (d) aerodynamic particle sizer and (e) scanning mobility particle sizer; (f) light scattering measured at 3 wavelengths (700 nm in red, 550 nm in green, and 450 nm in blue) from the nephelometer; and concentrations of (g) total particles (CN) from a condensation particle counter (black, left axis), total cloud condensation nuclei (CCN) at 0.4% supersaturation (red, left axis), and ice-nucleating particles (INP) in different size ranges (color bars, right axis).

Figure 16. Energy balance measurements for the February 5–7 case.
(a) Upward (red) and downward (blue) long-wave broadband radiation (LWU and LWD, respectively) measured at Met City; (b) infrared brightness temperature spectra observed by the Marine Atmospheric Emitted Radiance Interferometer; (c) 2-m temperature (blue) and the near-surface (T_{2m}–T_{sfc}) temperature gradient (red); and (d) turbulent sensible plus latent heat flux (red) and net radiative flux (blue) derived from Met City, along with the residual of these energy budget terms (black). According to Equation 1, because melting is zero at this time of year, this residual is comprised of the net change in temperature of the finite, thin surface layer and the sub-surface conductive heat flux.

Figure 17. Sea-level pressure and 850 hPa wind vectors averaged over July 13–15.
Data are derived from the ERA5 reanalysis. Sea-level pressure is given as colors in hPa. A 10 m s^{-1} wind vector is given in the legend and plotted wind vectors scale linearly.

Figure 18. Meteorological and surface energy balance measurements for the July 13–15 case.
(a) Temperature and (b) wind direction profiles from radiosondes for heights below 3 km; (c) surface pressure (black) and 10-m wind speed (red) from the Met City tower; downward and upward (d) shortwave and (e) longwave radiation from Met City (SWD, SWU, LWD and LWU, respectively); (f) 2-m (black, left axis) and surface temperatures (blue, left axis), and turbulent sensible (red, right axis) and latent (orange, right axis) heat fluxes (Hs and Hl, respectively) all derived from the Met City tower.

Figure 19. Cloud and aerosol measurements for the July 13–15 case.
(a) Radar reflectivity from the KAZR; (b) integrated water vapor (IWV, red) and liquid water path (LWP, black) derived from the HATPRO; aerosol size distributions (D_p) from the (c) aerodynamic particle sizer and (d) scanning mobility particle sizer; and time series concentrations of (e) total particles (CN, black, left axis) measured by condensation particle

counter, total cloud condensation nuclei (CCN) at 0.4% supersaturation (red, left axis), and ice-nucleating particles (INP) in different size ranges (color bars, right axis). Note the occasional ship pollution visible from the spiky vertical lines in (d).

Figure 20. Profile measurements on July 15 of the summer case.
(a) Potential temperature from BELUGA (blue), two DataHawk2 profiles (red, orange), three selected Distributed Temperature Sensing profiles from Miss Piggy (shades of green) and the nearest-in-time radiosonde profile (black); (b) relative humidity (RH) measurements from two DataHawk2 profiles (red, orange) and the nearest-in-time radiosonde profile (black); (c) wind speed from BELUGA (blue), two DataHawk2 profiles (red, orange) and the nearest-in-time radiosonde profile (black); (d) turbulent kinetic energy (TKE) from BELUGA; e) aerosol particle number concentrations (N) from BELUGA for particles larger than 10 nm (blue) and larger than 150 nm (green); and f) long-wave radiative heating rate (HR) profiles from BELUGA. In all cases the equivalent near-surface measurement derived from either the Met City tower or the aerosol measurements onboard *Polarstern* is included as an appropriately colored asterisk. The approximate location of the cloud layer at 13:00 (all times in UTC) is shown in shading.

Figure 21. An example of process-based model evaluation.
(A) Ten-minute average observations of scaled sensible heat fluxes (2-m sensible heat flux divided by 2-m wind speed, in units of W s m^{-3}) relative to near-surface stratification (2-m air temperature minus skin temperature, in °C) from three ASFS flux stations (black) and values binned for each flux station individually in intervals of 0.5°C (red). (B) Same as (A) but from 6-hourly output from 0–2 day forecasts from CAFS. (C) Same as (B) but using the CAFS 0–10 day forecasts to show that the model is not drifting into a different state. (D) Binned values from (A) and (C) to compare the observations (red) and model (black) forecasts more closely.

Tables Titles

Table 1. Primary ATMOS team observing locations, with approximate locations and headings relative to *Polarstern*

Table 2. Flight activities wherein *Polar 5* was equipped for the ACA program

Appendix A. Institutional participation in the ATMOS team

Abbreviation	Institution; Location	Summary of contribution
AWI	Alfred-Wegener-Institut Helmholtz-Zentrum für Polar- und Meeresforschung; Germany	radiosonde program, Miss Piggy tethered balloon, mobile eddy covariance, temperature profiling at fiber tower, water vapor isotopes, permanent ship installations, aircraft probes and dropsondes
BAS	British Antarctic Survey; UK	Aerosol and snow particle counters, snow and aerosol sample collection, ice-nucleating particle counter
Bigelow	Bigelow Laboratory for Ocean Sciences; USA	Gas flux chamber measurements
CSU	Colorado State University; USA	Aerosol and ice-nucleating particle samplers
CU-INSTAAR	Institute for Arctic and Alpine Research, University of Colorado; USA	Gas concentrations and fluxes
CU-NOAA	Cooperative Institute for Research in Environmental Science (CIRES), University of Colorado and National Oceanic and Atmospheric Administration; USA	10-m met tower, gas concentration and fluxes, surface energy budget stations, uncrewed aircraft observations, video in-situ snowfall sensor
CU-Aerospace	Integrated Remote and In Situ Sensing (IRISS), Smead Aerospace Engineering Sciences, University of Colorado; USA	Uncrewed aircraft observations
DLR	Institute for Physics of the Atmosphere; Germany	Aircraft particle probes
DOE-ARM	US Department of Energy Atmospheric Radiation Measurement Program; USA	radiosonde program, suite of 60 instruments to measure cloud, precipitation, aerosol, atmosphere structure, and radiation properties
EPFL	Swiss Federal Institute of Technology, Lausanne; Switzerland	Aerosol and trace gas measurement suite
FMI	Finnish Meteorological Institute; Finland	Radiation suite and uncrewed aircraft observations of surface albedo
FSU	Florida State University	Aerosol sampler
GFZ	German Research Centre for Geosciences; Germany	HELiPOD heat flux and gases
IGM	Institute for Geophysics and Meteorology, Cologne; Germany	Aircraft radar and radiometer

LaMP	Laboratoire de Meteorologie Physique; France	Aircraft particle probes
LIM	Leipzig Institute for Meteorology, University of Leipzig; Germany	Aircraft and ground-based spectral radiation, radiation measurements from BELUGA tethered balloon
PSI	Paul Scherrer Institute; Switzerland	Aerosol and gas measurements suite
TROPOS	Leibniz Institute for Tropospheric Research; Germany	OceanNet suite of cloud, atmospheric structure, and precipitation measurements, BELUGA tethered balloon, sensors for Miss Piggy balloon
TU Braunschweig	Institute of Flight Guidance, TU Braunschweig; Germany	HELiPOD
U. Alaska	University of Alaska – Anchorage; USA and University of Oulu; Finland	Water vapor isotope network
U. Cologne	University of Cologne; Germany	Microwave radiometer
U. Georgia	University of Georgia; USA	Aerosol sampler
U. Helsinki	University of Helsinki; Finland	Aerosol measurement suite
U. Leeds	University of Leeds; UK	Wind lidar, sodar, sonic anemometer
U. Michigan	University of Michigan; USA	Aerosol sampler
USTC	University of Science and Technology of China	Mercury measurements
U. Trier	University of Trier; Germany	Wind lidar
U. Vienna	University of Vienna; Austria	FLEXPART back trajectories

2682
2683

Appendix B. Measurement tables.

Table B1. Atmospheric physical state measurements.

Instrument	Measurements or products	Location[a]; timing	Institution[b]; contact
Primarily permanent installations			
Radiosonde	Profiles of pressure, temperature, humidity, winds, typically surface to 20 km	PS Helideck; 6-hourly continuous	AWI, DOE-ARM; Marion Maturilli
Cryogenic frostpoint hygrometer sondes	Profiles of stratospheric water vapor mixing ratio	PS Helideck; monthly	AWI; Marion Maturilli
Polarstern Met System	Pressure, temperature, relative humidity, winds, and visibility at 29–39 m	PS Crow's Nest; continuous	AWI; Holger Schmithüsen
Met Tower	Pressure (2 m), temperature, relative humidity, sonic anemometer winds (2, 6, 10 m)	MC; mostly continuous	CU-NOAA; Matthew Shupe
Met mast	Pressure, temperature, relative humidity, winds (23 or 30 m)	MC/CO; mostly continuous Legs 1–3	U. Leeds, CU-NOAA; Ian Brooks, Matthew Shupe
Ultrasonic anemometer	Winds at 16 m	PS Bow Tower; mostly continuous	CU-NOAA; Byron Blomquist
Distributed Temperature Sensing (DTS)	Temperature profile 0–10 m, along with profile down to 60-m depth in the ocean	CO; mostly continuous Legs 2–5	AWI; Alexander Schulz
Atmospheric Surface Flux Stations (ASFS)	Pressure, temperature, relative humidity (2 m), sonic anemometer winds (3 m), surface skin temperature	DN and CO; 3 systems with variable deployments	CU-NOAA; Matthew Shupe
Microwave radiometer, 2-channel (MWR-2C)	Sky brightness temperatures, column-integrated water vapor and liquid water path	PS P-deck; continuous	DOE-ARM; Maria Cadeddu
Microwave radiometer, 3-channel (MWR-3C)	Sky brightness temperatures, column-integrated water vapor and liquid water path	PS P-deck; continuous Legs 2–3	DOE-ARM; Maria Cadeddu
Humidity and Temperature Profiler (HATPRO)	Sky brightness temperatures, column-integrated water vapor, liquid water path, temperature and humidity profiles	PS Bow; continuous	TROPOS; Ronny Engelmann
Microwave Radiometer for Arctic Clouds (MiRAC-P)	Sky brightness temperatures, column-integrated water vapor, liquid water path, and humidity profiles	PS Bow; continuous	U. Cologne; Kerstin Ebell

Multiwavelength Raman Lidar (Polly XT)	3 backscatter, 2 extinction, 2 depolarization wavelengths, profiles water vapor mixing ratio	PS Bow; continuous	TROPOS; Ronny Engelmann
Cavity ring down spectroscopy analyzer	Near-surface water vapor mixing ratio and isotopic composition	PS P-deck; continuous	AWI; Martin Werner
Cavity ring down spectroscopy analyzer	Near-surface water vapor mixing ratio and isotopic composition, many stations in a network	PA; continuous	U. Alaska; Jeffrey Welker
Beam-Steerable Radar Wind Profiler (BSRWP)	Wind profiles, typically below 4 km	PS Bow; continuous	DOE-ARM; Paytsar Muradyan
Doppler lidar (DL)	Wind profiles, vertical velocity, turbulent dissipation rate, typically below 1 km	PS Bow; continuous	DOE-ARM; Rob Newsom
Doppler lidar	Turbulent kinetic energy profiles (all), wind profiles (Legs 3–5), typically below 1 km	PS P-deck; mostly continuous	U. Trier; Günther Heinemann
Doppler lidar	Wind profiles, typically below 1 km	PS P-deck; continuous	U. Leeds; Ian Brooks
Doppler lidar	Turbulent kinetic energy profiles, typically below 1 km	MC/CO; mostly continuous Legs 1–3; P-deck, mostly continuous Legs 3–5	U. Leeds; Ian Brooks
Sodar	Wind profiles, acoustic backscatter intensity, typically below 1 km	MC; mostly continuous	U. Leeds; Ian Brooks
Intermittently operated platforms			
DataHawk2	Flight-level pressure, temperature, humidity, winds, turbulence, in profiles and other patterns, various heights below 1 km	CO; Legs 3–4	CU-NOAA; Gijs de Boer
HELiX	Flight-level pressure, temperature, humidity, in profiles and other patterns, various heights below 0.4 km	CO; Leg 4	CU-NOAA; Gijs de Boer
HELiPOD	Flight-level temperature, humidity, winds, and surface temperature	Regional flights; Legs 3–4	TU Braunschweig, GFZ; Astrid Lampert, Torsten Sachs
Meteorology, on Miss Piggy	Flight-level temperature, humidity, winds, various heights below 1 km	BT; Legs 1–5	AWI; Jürgen Graeser
Hotwire anemometer, on Miss Piggy	Flight-level winds, various heights below 1 km	BT; Legs 1–3	TROPOS; Holger Siebert

Distributed Temperature Sensing (DTS), on Miss Piggy	Temperature profile, below 1 km	BT; Legs 2, 4, 5	AWI; Alexander Schulz
Meteorology, on BELUGA	Flight-level temperature, humidity, winds, various heights below 1 km	BT; Leg 4	TROPOS; Holger Siebert
Ultrasonic anemometer, on BELUGA	Flight-level 3-D winds, various heights below 1 km	BT; Leg 4	TROPOS; Holger Siebert

[a]PS = *Polarstern*, MC = Met City, BT = Balloon Town, CO = various locations in Central Observatory, DN = Distributed Network, and PA = pan-Arctic (see Figure 4 for locations).

[b]Abbreviations for institutions provided in Appendix A.

Table B2. Cloud and precipitation measurements.

Instrument	Measurements or products	Location[a]; timing	Institution[b]; contact
Primarily permanent installations			
Ceilometer	Backscatter, cloud base height	PS P-deck; continuous	AWI; Holger Schmithüsen
Ceilometer	Backscatter, cloud base height	PS P-deck; continuous	DOE-ARM; Vic Morris
Multiwavelength Raman lidar (Polly XT)	3 backscatter, 2 extinction, 2 depolarization wavelengths, profiles of cloud, and aerosol properties	PS Bow; continuous	TROPOS; Ronny Engelmann
High Spectral Resolution Lidar (HSRL)	Backscatter and depolarization ratio, profiles of cloud and aerosol properties	PS Bow; continuous	DOE-ARM; Ed Eloranta
Micropulse lidar (MPL)	Backscatter and depolarization ratio, profiles of cloud and aerosol properties	PS Bow; mostly continuous	DOE-ARM; Paytsar Muradyan
Ka-band ARM Zenith Radar (KAZR)	Doppler radar moments and spectra, profiles of cloud properties	PS Bow; continuous	DOE-ARM; Andrei Lindenmaier
Marine W-band ARM Cloud Radar (MWACR)	Doppler radar moments and spectra, profiles of cloud properties	PS Bow; continuous	DOE-ARM; Andrei Lindenmaier
Ka-band Scanning ARM Radar (Ka-SACR)	Doppler radar moments, spatial cloud distribution and properties	PS P-deck; mostly continuous	DOE-ARM; Andrei Lindenmaier
Total sky imager (TSI)	Visible hemispheric sky images, cloud coverage	PS P-deck; during sunlit periods	DOE-ARM; Vic Morris
Total sky imager	Visible hemispheric sky images, cloud coverage	PS Bow; during sunlit periods	TROPOS; Ronny Engelmann
Microwave radiometer, 2-channel (MWR-2C)	Sky brightness temperature, liquid water path	PS P-deck; continuous	DOE-ARM; Maria Cadeddu
Microwave radiometer, 3-channel (MWR-3C)	Sky brightness temperature, liquid water path	PS P-deck; continuous Legs 2-3	DOE-ARM; Maria Cadeddu
Humidity and Temperature Profiler (HATPRO)	Sky brightness temperature, liquid water path	PS Bow; continuous	TROPOS; Ronny Engelmann

Microwave Radiometer for Arctic Clouds (MiRAC-P)	Sky brightness temperature, liquid water path	PS Bow; continuous	U. Cologne; Kerstin Ebell
Present Weather Detector (PWD)	Precipitation occurrence and intensity	PS P-deck; continuous MC, mostly continuous	DOE-ARM; Jenny Kyrouac
Laser disdrometer (LDIS)	Precipitation and particle size distribution	PS P-deck; continuous MC, mostly continuous	DOE-ARM; Die Wang
Laser disdrometer	Precipitation and particle size distribution	PS Bow; continuous	TROPOS; Ronny Engelmann
2-D video disdrometer (2DVD)	Precipitation and particle size distribution	PS Bow; continuous	TROPOS; Ronny Engelmann
Weighing bucket rain gauge (WBRG)	Precipitation occurrence and mass	MC; mostly continuous	DOE-ARM; Die Wang
Siphon rain gauge (SRG)	Precipitation occurrence and mass	PS P-deck; continuous	DOE-ARM; Die Wang
Video In-Situ Snowfall Sensor (VISSS)	Precipitation particle size, type, shape	MC; Leg 1–3; PS P-deck; Leg 3–5	CU-NOAA; Maximilian Maahn
Snow particle counter (SPC)	Snow particle concentration, 40–500 µm, at 0.3 and 10 m	MC Met Tower; mostly continuous	BAS; Markus Frey
Rocket trap	Blowing snow collection for off-line ice-nucleating particle and ion analysis	MC; episodic Legs 1–3	BAS; Markus Frey
Intermittently operated platforms			
Video Ice Particle Sampler (VIPS), on BELUGA	In-situ videos of ice particles, particle shape and size distribution, various heights below 1 km	BT; Leg 4	LIM, TROPOS; Michael Lonardi

[a]PS = *Polarstern*, MC = Met City, and BT = Balloon Town (see Figure 4 for locations).
[b]Abbreviations for institutions provided in Appendix A.

Table B3. Aerosol measurements.

Instrument	Measurements or products	Location; timing	Institution; contact
Primarily permanent installations			
Condensation particle sounter (CPC)	Total particle number concentration > 10 nm	PS Bow; continuous	DOE-ARM; Chongai Kuang
Condensation particle counter	Total particle number concentration > 10 nm	PS Bow; continuous	EPFL/PSI; Julia Schmale
Condensation particle counter – ultrafine (CPCUF)	Total particle number concentration > 3 nm	PS Bow; continuous	DOE-ARM; Chongai Kuang
Condensation particle counter – ultrafine	Total particle number concentration > 3 nm, interstitial	PS Bow; continuous	EPFL/PSI; Julia Schmale
Condensation particle counter – ultrafine	Total particle number concentration > 2.5 nm	PS Bow; continuous	EPFL/PSI; Julia Schmale
Nano condensation nucleus counter (nCNC)	Particle size distribution, 1–3 nm	PS Bow; two systems continuous	U. Helsinki; Tuija Jokinen
Neutral Cluster and Air Ion Spectrometer (NAIS)	Air ion size distribution, 0.8–42 nm, neutral cluster size distribution, 2–42 nm	PS Bow; continuous Legs 1–5, PS Aft; Legs 4–5	U. Helsinki; Tuija Jokinen
Scanning Mobility Particle Sizer (SMPS)	Particle size distribution, 10–500 nm	PS Bow; continuous	DOE-ARM; Chongai Kuang
Scanning Mobility Particle Sizer (SMPS)	Particle size distribution, 17 -600 nm	PS Bow; continuous	EPFL/PSI; Julia Schmale
Ultra-High Sensitivity Aerosol Spectrometer (UHSAS)	Particle size distribution, 50–1000 nm	PS Bow; continuous	DOE-ARM; Janek Uin
Aerodynamic particle sizer (APS)	Particle size distribution, 0.5–20 µm	PS Bow; continuous	EPFL/PSI; Julia Schmale
Wideband Integrating Bioaerosol Spectrometer (WIBS)	Particle optical size, fluorescent particles 0.5–20 µm	PS Bow; continuous	EPFL/PSI; Julia Schmale
Aerosol spectrometer (OPC, GRIMM)	Particle size distribution, 0.3–40 µm	PS Bow; continuous	BAS; Markus Frey

Compact Lightweight, Aerosol Spectrometer Probe (CLASP)	Particle size distribution, 0.5–20 µm, particle flux	MC Met Tower; mostly continuous	BAS; Markus Frey
Cloud and Aerosol Spectrometer (CAS)	Particle size distribution, 0.51–50 µm	PS Crow's Nest; mostly continuous Legs 3–5	BAS;Markus Frey
Humidified Tandem Differential Mobility Analyzer (HTDMA)	Mass, size, and particle size distribution as a function of relative humidity, hygroscopicity	PS Bow; continuous	DOE-ARM; Janek Uin
Cloud condensation nucleus counter, 2 column (CCN200)	CCN concentration at supersaturation of 0.4% and scanning from 0 to 0.8%	PS Bow; continuous	DOE-ARM; Janek Uin
Cloud condensation cucleus counter (CCNC)	CCN concentration with supersaturation scanning from 0.15 to 1%	PS Bow; continuous for Legs 1–3	EPFL/TROPOS; Julia Schmale
Total aerosol filter sampler	Aerosol loadings for offline ice nucleating particle analysis and DNA sequencing, 3-day resolution	PS Bow; continuous	CSU; Jessie Creamean
Total aerosol filter sampler	Aerosol loadings for offline ice nucleating particle analysis and major ion/Br^- analysis, 2-day resolution	PS Bow; continuous	BAS; Markus Frey
PM2.5 aerosol filter sampler	Aerosol loadings for offline ice nucleating particle analysis, major ion/Br- analysis, and sulfur isotope analysis, 1-week resolution	PS Bow; continuous	BAS; Markus Frey
Davis Rotating-drum Unit for Monitoring (DRUM)	Size-resolved aerosol loadings for offline ice nucleating particle analysis, 4 bins 0.15–12 µm	PS Bow; continuous	CSU; Jessie Creamean
Spectrometer for Ice Nuclei (SPIN)	Ice nucleating particle concentration and size, 0.8–20 µm	PS Bow; episodic Leg 3	BAS; Markus Frey
Aerosol Chemical Speciation Monitor (ACSM)	Mass spectrum	PS Bow; continuous	DOE-ARM; Maria Anna Zawadowicz
Single Particle Soot Photometer (SP2)	Black carbon mass concentration	PS Bow; continuous	DOE-ARM; Art Sedlacek
Aethalometer	Equivalent black carbon	PS Bow; continuous	EPFL/PSI; Julia Schmale

Aerosol mass spectrometer (AMS)	Mass spectrum (sulfate, nitrate, ammonium, chloride, organics), 70–1000 nm	PS Bow; mostly continuous Legs 1, 3, 4	EPFL/PSI; Julia Schmale
Total aerosol filter sampler	Aerosol loadings for offline trace element chemistry analysis	PS P-deck; weekly Legs 2–3	U. Georgia, FSU; Clifton Buck, William Landing
Davis Rotating-drum Unit for Monitoring (DRUM)	Size-resolved aerosol loadings for offline single-particle morphology and elemental composition using computer-controlled scanning electron microscopy with energy-dispersive X-ray spectroscopy, 3 stages 0.1–12 µm	PS Bow; continuous	U. Michigan; Kerri Pratt
Nephelometer	Light scattering at dry relative humidity at 3 wavelengths	PS Bow; continuous	DOE-ARM; Janek Uin
Particle Soot Absorption Photometer (PSAP)	Light absorption at 3 wavelengths	PS Bow; continuous	DOE-ARM; Stephen Springston
Compact Optical Backscatter Aerosol Detector (COBALD) sondes	Aerosol backscatter profiles up to stratosphere	PS Bow; monthly during dark season	AWI; Marion Maturilli
Intermittently operated platforms			
Portable aerosol package (C3PO)	Particle size distribution, 0.38–17 µm, time-resolved aerosol loadings for offline ice-nucleating particle analysis	CO, various locations and times	CSU; Jessie Creamean
Condensation particle counter (CPC), on BELUGA	Total particle number concentration > 8 nm and > 12 nm, various heights below 1 km	BT; Leg 4	TROPOS; Christian Pilz
Portable Optical Particle Sizer (POPS), on BELUGA	Optical particle size distribution 150–3500 nm, various heights below 1 km	BT; Leg 4	TROPOS; Christian Pilz
Absorption photometer (STAP), on BELUGA	Light absorption at 3 wavelengths; equivalent black carbon, various heights below 1 km	BT; Leg 4	TROPOS; Christian Pilz
Optical particle counter (OPC), on Miss Piggy	Particle size distribution 0.3–40 µm, various heights below 1 km	BT; Legs 1–3	BAS; Markus Frey

Total aerosol filter sampler, on Miss Piggy	Aerosol loadings for offline ice-nucleating particle analysis, major ion/Br^- analysis, various heights below 1 km	BT; Legs 1–3	BAS; Markus Frey
HELiPOD	CPC, CPCU, OPC information on number concentration and size distribution, absorption at 3 wavelengths	Regional flights; Legs 3–4	TU Braunschweig; Astrid Lampert

[a]PS = *Polarstern*, MC = Met City, BT = Balloon Town, and CO = various locations in the Central Observatory (see Figure 4 for locations).

[b]Abbreviations for institutions provided in Appendix A.

Table B4. Gas measurements.

Instrument	Measurements or products	Location; timing	Institution; contact
Primarily permanent installations			
Ozonesondes	Profile of O_3 concentration up into stratosphere	PS Helideck; weekly	AWI; Peter von der Gathen
Ozone monitor	O_3 concentration	PS Bow; continuous	DOE-ARM; Stephen Springston
Ozone monitor	O_3 concentration	PS Bow; continuous	EPFL/PSI; Julia Schmale
Ozone monitor	O_3 concentration	PS Bow Tower; continuous	CU-NOAA, CU-INSTAAR; Byron Blomquist, Detlev Helmig
Atmospheric mercury analyzer	Gaseous elemental mercury concentration	PS Bow Tower; continuous	CU-NOAA, CU-INSTAAR; Byron Blomquist, Detlev Helmig
Atmospheric mercury analyzer	Gaseous elemental mercury concentration	PS P-deck; continuous	USTC; Zhouqing Xie
Chemiluminescent nitrogen oxides analyzer	NO, NO_2, and NO_y concentrations	PS Bow Tower; continuous	CU-NOAA, CU-INSTAAR; Byron Blomquist, Detlev Helmig
SO_2 monitor	SO_2 concentration	PS Bow; continuous	EPFL/PSI; Julia Schmale
Cavity ring-down spectrometer	CO, N_2O, and H_2O concentrations	PS Bow; continuous	DOE-ARM; Stephen Springston
Cavity ring-down spectrometer	CO, CO_2, CH_4, and H_2O concentrations	PS Bow; continuous	EPFL/PSI; Julia Schmale
Gas Chromatograph Mass Spectrometer, in-situ air sampling	Volatile organic trace gases, including halogenated gases	PS Bow Tower; continuous	CU-NOAA, CU-INSTAAR; Byron Blomquist, Detlev Helmig

Whole air samples into stainless steel canisters	Halogenated trace gases	PS; bi-weekly	CU-INSTAAR, UEA; Detlev Helmig, Bill Sturges
Whole air samples into glass flasks	Greenhouse gases, monitoring program from NOAA GML	PS; weekly	CU-NOAA, CU-INSTAAR; Byron Blomquist, Detlev Helmig
Chemical Ionization – Atmospheric Pressure interface Time-Of-Flight mass spectrometer (CI-APi-TOF)	Composition of condensing gases	PS Bow; continuous	U. Helsinki; Tuija Jokinen
Atmospheric Pressure interface Time-Of-Flight mass spectrometer (APi-TOF)	Composition of air ions	PS Bow; continuous	EPFL/PSI; Julia Schmale
Adsorbant trap air samples and analysis by gas chromatography	Atmospheric dimethyl sulfide	PS Bow Tower; episodic Legs 4-5	Bigelow; Steve Archer
Atmospheric pressure ionization mass spectrometer	Dimethyl sulfide concentration and flux	PS Bow Tower; continuous Legs 4–5	CU-NOAA; Byron Blomquist
Cavity ring-down spectrometer	CO_2 and CH_4 fluxes	PS Bow Tower; continuous MC Met Tower; mostly continuous	CU-NOAA; Byron Blomquist
Chemiluminescent ozone analyzer	O_3 flux	PS Bow Tower; continuous	CU-NOAA, CU-INSTAAR; Byron Blomquist, Detlev Helmig
CO_2 & CH_4 Dynamic Chamber Flux System	CO_2 and CH_4 gas exchange on snow, ice, or water surfaces	CO; various locations 2–3 times weekly	Bigelow Steve Archer
Dimethyl Sulfide Dynamic Chamber Flux System	DMS gas exchange on snow, ice, or water surfaces	CO; various locations 2–3 times weekly Legs 4–5	Bigelow; Steve Archer
Mobile or intermittently operated platforms			

Tethered balloon ozonesonde	Boundary layer ozone profile, various heights below 1 km	Selected balloon flights, Legs 2–4	CU-NOAA, CU-INSTAAR; Byron Blomquist, Detlev Helmig
Gas analyzers, on HELiPOD	CH_4, CO_2, and O_3 concentrations, CH_4, CO_2, and H_2O fluxes	Regional flights; Legs 3–4	TU Braunschweig, GFZ; Astrid Lampert, Torsten Sachs

[a]PS = *Polarstern*, MC = Met City, BT = Balloon Town, and CO = various locations in the Central Observatory (see Figure 4 for locations).

[b]Abbreviations for institutions provided in Appendix A.

Table B5. Physical samples to serve offline analyses.

Parameter	Type of sample[a]; method	Institution[b]; contact
Water isotopes ($\delta^{18}O$, $\delta^{2}H$)	Snow, precipitation; isotope ratio mass spectrometry	AWI; Martin Werner
INP	Snow, sea ice, melt ponds, leads, bulk seawater; off-line INP immersion freezing assays	CSU; Jessie Creamean
Marine polysaccharides, INP	Snow, sea ice, melt ponds, leads, ocean surface microlayer; off-line INP immersion freezing assays	TROPOS; Manuela van Pinxteren
INP, major ions, methanesulfonic acid, bromide, salinity, sulphate isotopes ($\delta^{34}S$)	Snow, blowing snow, bulk seawater; off-line INP immersion freezing assays, ion chromatography, isotope ratio mass spectrometry	BAS; Markus Frey
Black carbon	Snow; single-particle soot photometer	AWI; Andreas Herber
Iodide	Snow, sea ice; ion chromatography, voltammetry	University of York/IGE; Lucy Carpenter/Hans-Werner Jacobi

[a]All samples taken from the surface in the Central Observatory, intermittently over all legs of MOSAiC
[b]Abbreviations for institutions provided in Appendix A.

2709 **Table B6.** Energy budget measurements.

Instrument	Measurements or products	Location; timing	Institution and contact
Primarily permanent installations			
Sky-viewing broadband radiometer suite (SKYRAD)	Downward broadband solar and terrestrial radiation, direct and diffuse solar partitioning, sky infrared temperature	MC; nearly continuous	DOE-ARM; Laura Riihimaki
Sky-viewing broadband radiometer suite (SHIPRAD)	Downward broadband solar and terrestrial radiation	PS P-deck; 2 systems, continuous	DOE-ARM; Manajit Sengupta
Scalable automatic weather station (SCAWS)	Downward broadband solar and terrestrial radiation	PS Bow; continuous	TROPOS; Ronny Engelmann
Surface-viewing broadband radiometer suite (GNDRAD)	Upward broadband solar and terrestrial radiation, infrared surface temperature	MC; nearly continuous	DOE-ARM; Manajit Sengupta
Radiation suite	Upward and downward, broadband solar and terrestrial radiation, downward direct and diffuse solar partitioning	MC; nearly continuous Legs 1–3 CO; nearly continuous Legs 4–5	FMI; Roberta Pirazzini
Radiation suite	Upward and downward, broadband solar and terrestrial radiation	CO; variable deployments Legs 3 and 5	AWI; Alexander Schulz
Atmospheric Surface Flux Stations (ASFS)	Upward and downward, broadband solar and terrestrial radiation, infrared surface temperature, high-rate 3D winds and water vapor, temperature, surface flux plates, eddy correlation and bulk estimates of sensible and latent heat flux, surface conductive heat flux	DN and CO; 3 systems with variable deployments	CU-NOAA; Matthew Shupe
Multifilter Rotating Shadowband Radiometer (MFRSR)	Upward irradiance at 415, 500, 615, 673, 870, and 940 nm	MC; mostly continuous Legs 3-5	DOE-ARM; Gary Hodges
Marine Atmospheric Emitted Radiance	Spectral infrared radiation from the sky and surface, trace gas and cloud properties	PS P-deck; continuous	DOE-ARM; Jonathon Gero

Interferometer (MAERI)			
Compact Radiation Measurements System (CORAS)	Visible and near-infrared spectrometers	PS Bow; continuous Legs 3-5	LIM; Michael Lonardi
Sun photometer (CSPHOT)	Solar irradiance and sky radiance at 340, 437, 498, 669, 871, and 1021 nm, fixed pointing zenith	PS P-deck; continuous Legs 4–5	DOE-ARM; Lynne Ma
Met Tower	High-rate 3D winds and water vapor, temperature surface flux plates, eddy correlation and bulk estimates of sensible and latent heat flux, surface conductive heat flux	MC; mostly continuous	CU-NOAA; Matthew Shupe
Met mast	High-rate 3D winds and water vapor, temperature, eddy correlation and bulk estimates of sensible and latent heat flux	MC/CO; mostly continuous Legs 1–3	U. Leeds, CU-NOAA; Ian Brooks, Matthew Shupe
Polarstern bow tower	High-rate 3D winds and water vapor, temperature, eddy correlation and bulk estimates of sensible and latent heat flux	PS Bow Tower; mostly continuous	CU-NOAA; Byron Blomquist
Mobile eddy covariance sledges (MEC)	High-rate 3D winds and water vapor, temperature, eddy correlation and bulk estimates of sensible and latent heat flux	CO; variable deployments Legs 2–5	AWI; Alexander Schulz
Intermittently operated platforms			
HELiX	Upward and downward broadband solar radiation, multispectral camera, surface albedo, various heights below 0.4 km	CO; Leg 4	CU-NOAA; Gijs de Boer
Spectra	Upward and downward solar broadband and spectral irradiance, broadband and spectral surface albedo	CO; Leg 5	FMI; Roberta Pirazzini
Broadband radiation package, on BELUGA	Upward and downward broadband solar and terrestrial radiation, various heights below 1km	BT; Leg 4	LIM/TROPOS; Michael Lonardi
HELiPOD	Upward and downward broadband solar and terrestrial radiation, high-rate 3D winds and	Regional flights; Leg 3–4	TU Braunschweig, GFZ; Astrid Lampert, Torsten Sachs

	water vapor, temperature, eddy correlation estimates of sensible and latent heat flux		

[a]PS = *Polarstern*, MC = Met City, BT = Balloon Town, CO = various locations in the Central Observatory, and DN = Distributed Network (see Figure 4 for locations).
[b]Abbreviations for institutions provided in Appendix A.

Table B7. Aircraft measurements.

Instrument	Measurements or products	Institution[a]; contact
In-situ instrumentation		
Nose boom with turbulence probe	3-D winds, temperature, humidity, turbulent heat fluxes	AWI; Christof Lüpkes
Advanced Vertical Atmospheric Profiling System (AVAPS)	Downward profiles of pressure, humidity, temperature, winds	AWI; Christof Lüpkes
Polar nephelometer	Cloud particle scattering phase function	LaMP; Olivier Jourdan
2-D stereo probe (2D-S)	Cloud particle size and shape, 10 µm to 1.28 mm	LaMP; Olivier Jourdan
Cloud Combination Probe (CCP)	Cloud particle size and shape, 2–960 µm	DLR/JGU; Manuel Moser
Precipitation Imaging Probe (PIP)	Precipitation size and shape, 100 µm to 6.4 mm	DLR/JGU; Manuel Moser
Nevzerov probe	Liquid and total water content	AWI; Christof Lüpkes
Remote sensing instrumentation		
Spectral Modular Airborne Radiation measurement system (SMART) albedometer	Spectral radiance (nadir), irradiance (up, down) at 300–2200 nm, cloud albedo, optical depth, particle effective radius, ice indices	LIM; André Ehrlich
Airborne Imaging Spectrometer for Applications (AISA) Eagle	Spectral radiance in 512 pixels (36˚ swath), 300–1000 nm, cloud optical thickness	LIM; Marcus Klingebiel
AISA Hawk	Spectral radiance in 256 pixels (36˚ swath), 1000–2500 nm, cloud phase, particle effective radius	LIM; Marcus Klingebiel

Humidity And Temperature PROfiler (HATPRO)	Passive microwave radiometer, multi-channels near 22.24 and 60 GHz, integrated water vapor, liquid water path, temperature profiles	IGM; Mario Mech
Microwave Radar/radiometer for Arctic Clouds (MiRAC)	Cloud radar, 95 GHz for cloud geometry, precipitation, 89 GHz for LWP	IGM; Mario Mech
Airborne Mobile Aerosol Lidar (AMALi)	Particle extinction coefficient, cloud top height	AWI; Christof Lüpkes
Sun photometer	Aerosol optical depth	AWI; Andreas Herber
180˚ fish-eye camera	Bidirectional reflectance distribution function, cloud phase function, photo documentation	AWI/LIM; André Ehrlich
Basis instrumentation		
Broadband radiometers	Solar and terrestrial broadband irradiance, upward and downward	AWI; Christof Lüpkes
Infrared thermometer	Cloud top or surface temperature	AWI; Christof Lüpkes
Laser altimeter	Ground altitude	AWI; Christof Lüpkes

[a]Abbreviations for institutions provided in Appendix A.